Encoding of non-MR Signals in Magnetic Resonance Imaging

Pedersen, Jan Ole

Publication date:
2018

Document Version
Publisher's PDF, also known as Version of record

Encoding of non-MR Signals in Magnetic Resonance Imaging

Jan Ole Pedersen
PhD thesis
February 2018

DTU Electrical Engineering
Department of Electrical Engineering

DTU Electrical Engineering
Department of Electrical Engineering
Center for Magnetic Resonance
Technical University of Denmark
Ørsteds Plads
Building 348
DK-2800 Kgs. Lyngby
Denmark
Tel: (+45) 45 25 38 00
www.elektro.dtu.dk

Sino-Danish Center for Education and Research
Niels Jensens Vej 2
Building 1190
DK-8000 Aarhus C
Denmark
Tel: (+45) 87 15 25 97
www.sdc.university

Summary

Magnetic resonance imaging (MRI) is widely used for both clinical and research purposes, and offers non-invasive imaging of tissues within the head and body of patients. Generation of the magnetic resonance (MR) signal relies on the presence of a large, static, main magnetic field, and temporally varying gradient and radio-frequency fields, that typically alternate at kilohertz and megahertz frequencies. During scanning, other signals than the MR signal are often of interest, e.g., biomedical signals from the imaged patient for multi-modal studies, and precise characterization of the scanner's electromagnetic fields for improving image quality. The static magnetic field, however, prevents having typical measuring equipment in the vicinity of the scanner, and the oscillating fields induce unwanted currents in cabling and transducers, causing artefacts in acquired non-MR signals. Using the scanner to acquire both the MR and the non-MR signals partially alleviates these challenges, as the scanner's fields are typically not alternating during MR acquisition periods. In addition, this yields a high degree of synchronization between the scanner and the acquisition of the non-MR signals, which for most applications is highly beneficial. Such acquisition is, however, challenged by filters of the scanner attenuating signals with frequencies far from those of the MR signal.

This thesis evolves around solving the engineering challenges arising from using an MR scanner for acquisition of non-MR signals. Custom circuitry is presented, which facilitates this through real-time signal processing, and digital synthesis of scanner-recorded signals. The applicability of the circuitry is exemplified by emulation of a point-shaped MR source from real-time measurements of the scanner's electromagnetic fields.

For demanding sequences, reconstruction based on nominal gradient fields, and thereby nominal k-space trajectories, leads to degradation and artefacts in MR images, which can be avoided if the actual k-space trajectory is determined. In a second study, an inductively generated k-space trajectory measure is generated and acquired by an MR scanner concurrently with MRI. Initial results from a solely inductive measure are improved by regularization using a measure of the current driving the gradient field. Minimal artefacts are observed when reconstruction is based on the measured k-space trajectory, and improved image quality compared to reconstructions based on the nominal trajectory is obtained.

Lorentz forces induced in generation of the gradient field lead to loud acoustic noises that challenge speech recording in the MR environment. In a third study, an induction-based transducer and amplitude modulation are used to facilitate concurrent MRI and audio sampling. The resulting synchronization between gradient field shifting and speech signal sampling facilitates simple removal of the scanner-induced noise, and audible speech recordings are obtained.

Resumé

Billeddannende magnetisk resonans er en non-invasiv billeddannelsesmetode, der anvendes til både kliniske og forskningsrelaterede formål. Magnetisk resonans (MR) er afhængig af et kraftigt, statisk, magnetfelt og temporalt vekslende gradient- og radiofrekvensfelter, som typisk veksler ved kilohertz- og megahertzfrekvenser.

Under skanning kan andre signaler end MR signalet være af interesse, for eksempel biomedicinske signaler fra patienten i multimodale undersøgelser, og præcis karakterisering af skannerens elektromagnetiske felter, for at forbedre kvaliteten af genererede billeder. Det statiske magnetfelt forhindrer imidlertid at have typisk måleudstyr i nærheden af skanneren, og de oscillerende felter inducerer uønskede strømme i kabler og transducere, hvilket fører til artefakter i udlæste ikke-MR signaler. Disse udfordringer kan til dels undgås, hvis skanneren bruges til at optage både MR- og ikke-MR signalet, da skannerens felter typisk ikke veksler mens MR signalet udlæses. Desuden opnås en høj grad af synkronisering mellem skanneren og udlæsningen af ikke-MR signalet, hvilket typisk er yderst fordelagtigt. Denne fremgangsmåde er dog udfordret af filtre i skanneren, som dæmper signaler med frekvenser langt fra MR signalets frekvenser.

Denne afhandling omhandler bestemmelse af løsninger på de tekniske udfordringer, som opstår ved at bruge en MR skanner til at optage ikke-MR signaler. Afhandlingen introducerer specialudviklet elektronik, som muliggør dette gennem realtidsignalbehandling og digital syntesering af signaler der kan optages af en MR skanner. Som et eksempel på en anvendelse, er den præsenterede elektronik brugt til emulering af en punktformet MR-kilde fra realtids-målinger af skannerens elektromagnetiske felter.

For krævende sekvenser fører billedrekonstruktion baseret på nominelle gradientfelter, og derved nominelle k-rumstrajektorier, til forringelse og artefakter i genererede billeder. Dette kan dog undgås, hvis det faktiske k-rumstrajektorie bestemmes. Igennem en forsøgsrække blev et induktivt mål for k-rumstrajektorier genereret og udlæst af en MR skanner samtidig med MR signalet. Indledende resultater fra et udelukkende induktivt mål blev forbedret ved at udføre regulering baseret på målinger af strømmen som genererer gradientfeltet. Rekonstruktioner baseret på de målte k-rumstrajektorier indeholdte kun begrænsede artefakter, og k-rumsbestemmelsen gav derved anledning til en forbedret billedkvalitet sammenlignet med rekonstruktioner baseret på nominelle k-rumstrajektorier.

Lorentz-kræfter, induceret ved generering af gradientfeltet, fører til kraftig akustisk støj der besværliggør optagelse af tale i skannerrummet. I et tredje eksperiment blev en induktionsbaseret mikrofon og amplitude-modulation anvendt til at facilitere samtidig MR- og lydoptagelse. Dette resulterede i en høj grad af synkronisering mellem veksling af gradientfeltet og udlæsning af lydsignalet, hvilket gjorde det muligt at bruge simpel signalbehandling til at fjerne den skannerinducerede støj fra lydoptagelser af blandet støj og tale.

Preface

This thesis has been submitted to the Department of Electrical Engineering at the Technical University of Denmark (DTU) in partial fulfilment of the PhD degree requirements. The thesis documents research conducted from December 1st 2014 until February 5th 2018. The project was funded by the Sino-Danish Center for Education and Research (SDC), DTU, Institute of Electrical Engineering with additional contributions from the Danish Research Center for Magnetic Resonance, Copenhagen University Hospital, Hvidovre (DRCMR). The research was conducted at DRCMR, DTU, and for two periods of combined 9 months at State Key Laboratory of Brain and Cognitive Sciences, Institute of Biophysics, Chinese Academy of Sciences, Beijing (CAS) under supervision of Associate Professor Lars G. Hanson and Professor Rong Xue.

During the stays at CAS lectures were given for part of the course *Fundamental Biomedical Signal Processing (FBSP)* offered by SDC in Beijing (fall 2015 and fall 2016). For the course *Medical Magnetic Resonance Imaging (31547)* offered by DTU, teaching assistant responsibilities were met by assisting during problem solving, and providing feed-back on hand-in assignments (spring 2016 and spring 2017).

Acknowledgements

I would like to express my gratitude to my main supervisor Lars Hanson, for his continuous guidance and support throughout the PhD. Your continuous enthusiasm for discussing and explaining theoretical and experimental concepts have been invaluable, and your willingness to join late-night scanning marathons is immensely appreciated. I owe you many thanks for your always favourable advice and good mood. Likewise, I would like to thank Christian Hanson for his contributions to the presented work. I greatly appreciate you using your knowledge and spare time to answer questions and designing hardware necessary for me to finish my PhD. I am very grateful to Rong Xue for her support and guidance. Thank you for supervising me, and letting me visit your lab, where I gained valuable knowledge, and was very well received by fellow students and researchers. I would also like to thank Vitaliy Zhurbenko for discussions and inputs through the past three years.

Next, I would like to thank my colleagues at DTU, DRCMR and SDC for making both work hours and after-work hours pleasant. I enjoyed coming to work every day, which you all can be accredited for. A special thanks goes to those who have helped me throughout the project by discussing experimental procedures and sharing your knowledge of MR theory and hardware. It has truly been a privilege to work with all of you. In addition, I would like to thank the leadership at the institutions for funding the project.

Finally, I would like to thank friends and family for your support and for your patience when deadlines and late-hour scanning have prevented my presence. Above all, I would like to express my appreciation of Giske for her imperishable support and encouragement. You have been a great discussion partner, and have made conferences and external stays highly enjoyable. I owe you all my love for your help throughout my PhD, but especially in the final stages, where clean clothes, lunch boxes and a continuous flow of Forest Fruit tea have magically materialized around me.

Contents

1 | Introduction

Magnetic resonance imaging (MRI) is a widely used medical imaging modality in both research and clinical contexts[1],[2]. The precessing magnetization of an isochromate experiencing a strong magnetic field is perturbed by short bursts of radio-frequency (RF) radiation, which brings the magnetization away from thermal equilibrium. While again approaching equilibrium, a radio-frequency signal (the MR signal) is induced with sample-specific relaxation rates and frequency equal to the precession frequency of the magnetization. As this frequency is depending on the magnetic field experienced by each isochromate, spatial frequencies of the magnetization density can be encoded by applying linear magnetic field gradients across an object constituted by a large number of isochromates. An image of the object with a relaxation-dependent contrast can be reconstructed by Fourier transformation of the MR signal acquired at different spatial frequencies, with the obtainable image resolution depending on the range of spatial frequencies at which the MR signal is sampled. In order to obtain useful images in reasonable time, the MR signal is typically discretely sampled in fast succession while the spatial frequencies are varied dynamically, facilitating sampling at multiple spatial frequencies after a single burst of RF radiation.

MR signal acquisition, generation of the RF field, and generation of the magnetic field gradients are handled by different scanner subsystems, namely the receive chain, the transmit chain and, in combination, the gradient amplifier and gradient coils. Typical precession frequencies of the isochromate magnetization require sub-µs timing and synchronization between these subsystems. Also, since their behaviour is usually advantageously constant over considerable time periods, a high degree of temporal stability is sought for the individual subsystems.

The MR signal is easily unwantedly perturbed by uncontrolled factors, e.g., subject motion and imperfect performance of the scanner's subsystems. This causes a mismatch between the nominal and actual state of the isochromate magnetizations, which can limit the feasible spatial acquisition schemes[3],[4] and/or cause artefacts in the reconstructed images[5],[6]. The effects of the perturbations can often be countered if the cause of these is monitored during scanning. This yields the need for acquiring non-MR signals concurrent with MR acquisition. In addition, other modalities, e.g., electroencephalography (EEG)[7] or subject speech recording[8], can be of interest during MRI, adding to the list of signals of interest (SOIs) during MRI.

The acquisition of such SOIs is challenged by the strong static magnetic field necessary for generation of the MR signal ($\mathbf{B}_0$), which prevents having most typical measuring equipment in proximity of the scanner. Besides this, the changing field gradients and RF transmission can induce severe artefacts in electromagnetic signals when transducers or cabling are placed near the scanner, and the equipment may in turn perturb the MR signal. Depending on the SOI, different approaches have been developed to overcome these challenges.

One strategy is to encode the SOI in an electromagnetic bandwidth far from the frequencies of the induced artefacts, or use a non-electromagnetic signal carrier. Both allow for transmitting the SOI to a transducer positioned away from the scanner, where its electromagnetic fields are less restrictive regarding the choice of equipment. Examples include respiratory state monitoring, which is typically encoded as pressure in a tube[9], and fibre-optic transmission, which is viable, since the frequency range of the optic signal lies far from the operating frequencies of the scanner subsystems[8],[10],[11],[12].

Another strategy is to allow scanner-induced artefacts in SOI recordings, and rely on filtering to remove these after sampling by using prior knowledge of the SOI and the artefacts. This approach is often used for, e.g., EEG, but is challenged by the SOI potentially being orders of magnitude smaller than the artefacts induced by the scanner, which compromises the robustness, e.g., when subjects move[7]. For speech recordings, scanner-induced acoustic noise can be removed from the SOI-recording by subtraction of a noise-only signal based on recordings acquired far from the subject[8],[13]. This is feasible for speech recordings in particular, due to the noise-only signal being easily obtainable.

During considerable periods of typical MRI scans, gradients are not altered and no RF bursts are applied. This is exploited in a third strategy, where the SOIs are only sampled in periods where the scanner-generated artefacts are limited or not present[14]. If sampling of the SOI in addition is phase-locked to the subsystems generating the artefacts, any residual artefacts are easily filtered out. This approach requires a high degree of synchronization to the scanner which is non-trivial to obtain.

Using the scanner itself for sampling of the SOI facilitates the necessary synchronization directly, since the above-mentioned periods typically coincide with MR sampling, and the scanner's subsystems by design are highly synchronized. Doing so is restricted to signals with frequencies close to the frequency of the MR signal, due to bandpass filters in the receive chain of MR scanners[15]. The SOI can alternatively be encoded into the MR signal, which is possible for some cases of scanner subsystem monitoring. Examples of this are the pre-scans that are typically run before an actual MR scan to address scanner subsystem imperfections, such as inhomogeneities in $\mathbf{B}_0$[16] and adjustments to the RF transmission gain[17],[18]. For other SOIs with frequencies outside the passband of the receive chain filters, this is not necessarily possible. Sampling by the MR scanner is, however, still feasible by modulation of a carrier signal with a frequency within the passband of the receive chain filters. This facilitates unattenuated passage of the filters, and is in addition partially undone by the demodulation also done in the receive chain, simplifying the extraction of the SOI from the scanner-acquired data[15]. Some SOIs are not directly receivable using this method, due to, e.g., the available bandwidth being insufficient, gaps between scanner sampling being confounding, and/or the SOI not being directly available and having multiple dependencies. A common solution to these challenges is to perform signal processing before transmission to the scanner, though necessary signal processing is highly specific for the SOI in question.

In the work presented in this thesis, different non-MR SOIs were sampled by an MR scanner. Acquisition of these is heavily challenged by concurrent MR scanning, and requires specialized equipment and/or complex experimental procedures when done by other means. Sampling of the SOIs is facilitated by custom circuitry, that provides real-time flexible signal processing of multiple inputs, and transmission of a modulated signal receivable by MR scanners. The presented experimental procedures lay the groundwork for a general framework for sampling of non-MR signals in an MR environment.

1.1 Outline

Chapter 2 introduces the underlying theory of MR imaging and reconstruction. A general introduction to MR hardware and its role for generation of MR images is also given.
Chapter 3 describes methods for acquiring non-MR SOIs by an MR scanner through modulation of a carrier signal. The chapter introduces the manuscript provided in Appendix A, where a circuitry facilitating flexible pre-processing and MR scanner acquisition of SOIs is presented. The chapter further discusses procedures for detection of RF pulses applied by MR scanners.
Chapter 4 initially describes putative causes for deviation from nominal k-space trajectories, and reviews approaches for correcting these presented in literature. The chapter serves as introduction to the manuscript presented in Appendix B, where an MR scanner was used to sample regularized inductive measures of k-space trajectories.
Chapter 5 reviews efforts in acquisition of speech recordings concurrently with MRI. Following this, experimental procedures for the abstract presented in Appendix C is presented, and the feasibility of acquiring audio recordings by an MR scanner is discussed.
Chapter 6 and **Chapter 7** contains general discussions, conclusions and future perspectives.

2 | Magnetic Resonance Imaging Theory and Hardware

The following sections describe general MRI theory and hardware relevant for image acquisition and reconstruction. The notation of Nishimura[19] is followed exclusively, unless other sources are referenced.

2.1 The Bloch Equations

Ignoring the RF field, from here on referred to as $\mathbf{B}_1(t)$ and assumed homogeneous, the total magnetic field in an MR scanner at position $\mathbf{r}$ at time t, $\mathbf{B}(\mathbf{r},t)$, consists of a near-homogeneous time-independent field, $\mathbf{B}_0$, and a temporally and spatially dependent gradient field $\mathbf{B}_G(\mathbf{r},t)$. Even though $\mathbf{B}_G(\mathbf{r},t)$ has both $\hat{\mathbf{x}}$-, $\hat{\mathbf{y}}$- and $\hat{\mathbf{z}}$-components, a typical approximation is to only consider the component pointing in the same direction as $\mathbf{B}_0$, denoted by $\hat{\mathbf{z}}$:

$$\mathbf{B}(\mathbf{r},t) = \hat{\mathbf{z}}[B_0 + B_G(\mathbf{r},t)]. \tag{2.1}$$

$B_G(\mathbf{r},t)$ is typically generated by a set of linear gradients, one in each Cartesian direction, thus

$$B_G(\mathbf{r},t) = G_x(t)x + G_y(t)y + G_z(t)z = \mathbf{G}(t)\cdot\mathbf{r}. \tag{2.2}$$

The behavior of a nuclear magnetization, $\mathbf{M}$, positioned in $\mathbf{B}(\mathbf{r},t)$, can be described by the Bloch equations as

$$\frac{d\mathbf{M}}{dt} = \mathbf{M}\times\gamma\mathbf{B}(\mathbf{r},t) - \frac{M_x\hat{\mathbf{x}} + M_y\hat{\mathbf{y}}}{T_2} - \frac{(M_z - M_0)\hat{\mathbf{z}}}{T_1}, \tag{2.3}$$

where T_1 and T_2 denotes longitudinal and transversal relaxation times, and $\hat{\mathbf{z}}\cdot M_0$ denotes the magnetization at equilibrium. All three have have spatial dependencies that for simplicity are omitted. Following this, the magnetization will be precessing around $\mathbf{B}(\mathbf{r},t)$ with a frequency dependent on the gyromagnetic ratio, γ. The absolute precession frequency $\omega_L(\mathbf{r},t)$, or Larmor frequency, is a function of the total magnetic field strength, $B(\mathbf{r},t)$:

$$\omega_L(\mathbf{r},t) = \gamma B(\mathbf{r},t) = \gamma\left(B_0 + B_G(\mathbf{r},t)\right) = \omega_0 + \omega_G(\mathbf{r},t). \tag{2.4}$$

In matrix-vector notation the Bloch equations become

$$\begin{pmatrix} \frac{dM_x}{dt} \\ \frac{dM_y}{dt} \\ \frac{dM_z}{dt} \end{pmatrix} = \begin{pmatrix} -1/T_2 & \gamma B(\mathbf{r},t) & 0 \\ -\gamma B(\mathbf{r},t) & -1/T_2 & 0 \\ 0 & 0 & -1/T_1 \end{pmatrix} \begin{pmatrix} M_x \\ M_y \\ M_z \end{pmatrix} + \begin{pmatrix} 0 \\ 0 \\ M_0/T_1 \end{pmatrix}. \tag{2.5}$$

Introducing complex notation allows for combining M_x and M_y into a common transversal component, $M_\perp$:

$$M_\perp = M_x + \mathrm{i}M_y. \tag{2.6}$$

The Bloch equations can then be written as

$$\frac{dM_\perp}{dt} = \frac{dM_x}{dt} + \mathrm{i}\frac{dM_y}{dt} = -\left[\frac{1}{T_2} + \mathrm{i}[\omega_0 + \omega_G(\mathbf{r},t)]\right] M_\perp \tag{2.7}$$

$$\frac{dM_z}{dt} = -\frac{M_z - M_0}{T_1}. \tag{2.8}$$

General solutions for the transversal and longitudinal component are

$$M_\perp(\mathbf{r},t) = M_\perp(t=0)\exp(-t/T_2)\exp(-\mathrm{i}\omega_0 t)\exp\left(-\mathrm{i}\gamma\int_0^t \mathbf{G}(\tau)\cdot\mathbf{r}\,d\tau\right), \tag{2.9}$$

$$M_z(t) = M_0 + (M_z(t=0) - M_0)\exp\left(-t/T_1\right). \tag{2.10}$$

Applying a burst of an RF oscillating electromagnetic field, $\mathbf{B}_1(t)$, on resonance with the Larmor frequency rotates a magnetization from longitudinal orientation towards transversal orientations. This is referred to as excitation, and the effective time of excitation is referred to as $t = 0$ or the isodelay point[20].

2.2 Signal Equation and Selective Excitation

Ignoring the spatially dependent relaxation and coupling to the scanner's receive coils, the signal received during MRI reflects the total transversal magnetization over the imaged volume:

$$s_r(t) \propto \int_x\int_y\int_z M_\perp(\mathbf{r},t)\,dx\,dy\,dz. \tag{2.11}$$

Applying $\mathbf{B}_1(t)$ simultaneously with gradients allows for spatially selective excitation, where $\mathbf{B}_1(t)$ is on resonance with the local Larmor frequency. Applying a gradient in the $\hat{\mathbf{z}}$-direction, thus leads to the excitation of a slice in the xy-plane, where the slice thickness depends on the gradient strength and the RF bandwidth. In a slice with thickness Δz located at $z = z_0$, the transversal magnetization density for a given position (x, y) becomes

$$m(x,y) = \int_{z_0-\Delta z/2}^{z_0+\Delta z/2} M_\perp(\mathbf{r}, t=0)\,dz \tag{2.12}$$

and the signal received from the entire sample

$$s_r(t) \propto \int_x\int_y m(x,y)\exp(-\mathrm{i}\omega_0 t)\exp\left(-\mathrm{i}\gamma\int_0^t \mathbf{G}(\tau)\cdot\mathbf{r}\,d\tau\right)dx\,dy. \tag{2.13}$$

Performing a demodulation, i.e., multiplying by $\exp(\mathrm{i}\omega_0 t)$, effectively transforms the coordinate system from the laboratory reference frame to a rotating reference frame, which for most applications simplifies theory. After excitation, the slice selecting gradient is typically not applied, thus $G_z(t) = 0$. Introducing the spatial frequencies $k_x(t)$ and $k_y(t)$ as

$$k_x(t) = \frac{\gamma}{2\pi}\int_0^t G_x(\tau)\,d\tau,$$

$$k_y(t) = \frac{\gamma}{2\pi}\int_0^t G_y(\tau)\,d\tau, \tag{2.14}$$

therefore leads to the demodulated signal becoming

$$s(k_x, k_y) \propto \int_x \int_y m(x, y) \exp\left(-\mathrm{i}2\pi[k_x(t)x + k_y(t)y]\right)\, dx\, dy, \tag{2.15}$$

This equation is referred to as the signal equation. From this it follows, that the received signal is dependent on the spatial frequency component of $m(x, y)$ at spatial frequencies $k_x(t)$ and $k_y(t)$. As discussed in the following, an image is obtainable from the signal by sampling $s(k_x, k_y)$ at sufficiently different values of k_x and k_y. This leads to the introduction of the spatial frequency space, or more commonly the k-space, which is typically illustrated as a Cartesian coordinate system with positive and negative k_x's and k_y's on the axes. During image acquisition, gradients are alternated while the signal is sampled over time in order to "fill out" a central region of k-space.

2.3 k-Space Sampling Schemes and Image Reconstruction

Through reconstruction, an image of $m(x, y)$ is obtained from sampled data, $s(k_x, k_y)$. From Eq. 2.15 it follows, that $s(k_x, k_y)$ is proportional to the 2D Fourier transform of $m(x, y)$, thus reconstruction revolves around 2D inverse Fourier transformation, which is facilitated by multiple algorithms. Due to a much faster computational time compared to other alternatives, Fast Fourier Transformation (FFT) is almost exclusively used. This is despite it only being directly applicable for Cartesian sampled k-space, where the MR signal is sampled on a Cartesian grid. An example is echo-planar imaging (EPI), shown in Fig. 2.1 (top). Here, $k_x(t)$ and $k_y(t)$ are exchanged for $k_m(t)$ and $k_p(t)$, which denotes spatial frequencies in the readout and phase-encoding direction, respectively.

Unfiltered reconstruction of a Cartesian sampled k-space leads to a *sinc*-shaped point spread function (PSF), which seldom is ideal, as sidebands continue towards infinity. While the PSF can be filtered to a desired shape, it can also be improved by performing non-Cartesian sampling. Examples of this are spiral imaging, where k-space is sampled in spiral shaped trajectories (Fig. 2.1 bottom), and radial imaging, where k-space is sampled in multiple straight lines forming spoke-like trajectories. Both can lead to a more dense sampling of the center of k-space than Cartesian sampling, and yield modified PSFs with limited sidebands[21].

For reconstruction of non-Cartesian data, FFT is typically still used after interpolation, or regridding of sampled data. Convolving the non-Cartesian sampled data with an interpolation kernel approximates $m(x, y)$ over the entire sampled k-space, that can be resampled on a Cartesian grid, facilitating the use of FFT. Ideally an infinite *sinc* function is used as kernel, but as this is not computationally feasible, a common choice is instead a Kaiser-Bessel function[4]. Other kernels have been suggested in literature, typically leading to another weighting of precision versus computational time. Besides the interpolation onto a Cartesian grid, the inhomogeneous sampling density of the non-Cartesian sampling must also be addressed. This is done with a so-called density compensation function, that for some trajectories can be determined analytically, but is typically determined numerically[22].

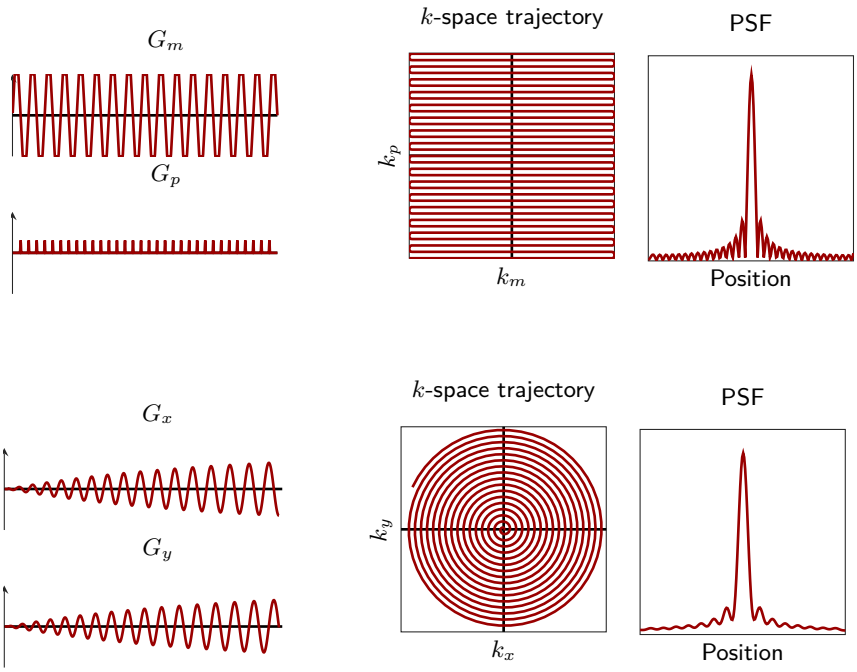

Fig. 2.1. Time evolution of gradient waveforms (left), the resulting k-space trajectories (center) and cross-section of point spread functions (right) of an EPI (top) and spiral (bottom) trajectory.

2.4 MR Scanner Hardware

An MR scanner relies on multiple subsystems that process electromagnetic fields oscillating at different frequencies. The fields are generated and received by largely concentric coils, so that an imaged object is exposed to the field of all coils simultaneously. A simplified schematic of an MR scanner is given in Fig. 2.2. References to this schematic in the following are given in parenthesis.

User-inputs given to a host computer are sent to a Central Control Device (CCD), that communicates instructions to the individual subsystems using a common master clock, securing the necessary sub-µs synchronization between subsystems.

The main magnet is typically superconducting and responsible for creating $\mathbf{B}_0$ (typically 1.5 T or 3 T), which is designed to be highly homogeneous. Putative inhomogeneities are addressed by adding spatially varying shim fields. First order shimming is typically done by the gradient coils, while dedicated shim coils are used for higher order shimming (not depicted in Fig. 2.2). Besides shimming, which often is performed in prescans, the main magnetic field is not changed during imaging.

The gradient field, $\mathbf{B}_G$, generated by the gradient system (green), typically consists of three spatial components with linear dependency in orthogonal directions. For imaging sequences, $\mathbf{B}_G$ facilitates the spatial and temporal alteration of the scanner's magnetic field ($\mathbf{B}_0 + \mathbf{B}_G$)

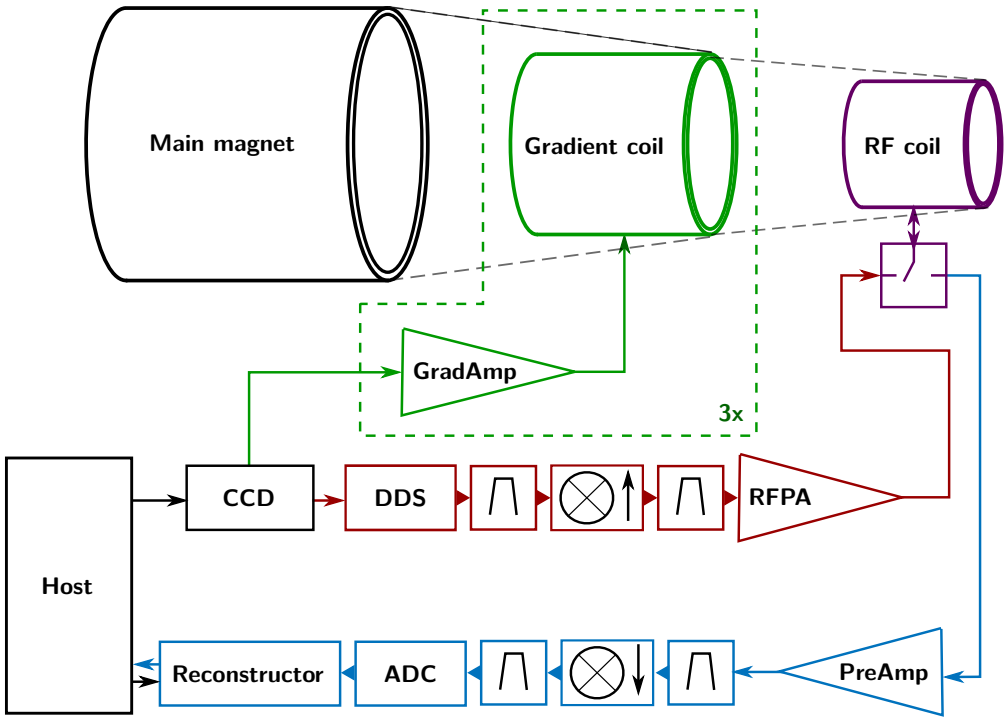

Fig. 2.2. Schematic of scanner components relevant for MRI. Adopted from [23] and [24].

necessary to traverse k-space, and is applied in a large fraction of the scanning time. For demanding sequences, such as EPI and diffusion weighted sequences, the field oscillates at, e.g., 2 kHz with gradient strength of 20 mT/m over a spherical volume of 300 mm diameter. The spatial dependency is typically in reference to a Cartesian coordinate system with origin in the isocenter of the coils, yielding both negative and positive main field changes that scale with distance to the isocenter. As $\mathbf{B}_G$ is generated by resistive coils, water cooling is applied to counteract heating of the gradient system due to ohmic losses. Despite of this, the gradient system will typically heat up for gradient intensive sequences, leading to thermal expansion and temporally changing characteristics of both amplifiers (GradAmp) and coils. The implications of gradient system imperfections are discussed further in Chapter 4.

The RF system is composed of the transmit chain (red), the receive chain (blue), and a common transmit-receive (T/R) switch and RF coil (purple). The T/R switch protects the receive chain from high-power signals generated by the transmit chain. In the transmit chain, a Direct Digital Synthesizer (DDS) synthesises low-power arbitrary waveforms in a frequency range similar to that of Larmor frequency variation caused by $\mathbf{B}_G$. The waveforms are bandpass-filtered ($\sqcap$) before being modulated ($\otimes \uparrow$) to ω_L (typically in the 10–130 MHz range) using frequency mixing. The waveforms are again bandpass filtered before being amplified by the RF power amplifier (RFPA) to 1–50 kW RF pulses, that are wirelessly applied to the imaged object by the RF coil in short bursts lasting a few milliseconds.

After experiencing an RF pulse, the imaged object will induce an MR signal in the RF coil. The

signal is amplified (PreAmp) before reaching a receive channel of the scanner. Here the signal is bandpass-filtered around ω_L, and demodulated by frequency mixing ($\otimes \downarrow$) and bandpass filtering. The demodulated analog MR signal is then digitized by analog-to-digital converters (ADC) and passed on to the reconstructor. The reconstructor additionally receives information of the nominal k-space trajectory from the host computer to facilitate correct positioning of the received MR data in k-space. The reconstructor transforms the received MR signal to images, that are presented to the user by the host computer. The receive chain typically features multiple parallel channels, that allow for receiving the MR signal from an RF coil constituted by multiple separate receive coils.

3 | MR Scanner Acquisition of non-MR Signals

Acquisition of non-MR signals of interest (SOIs) in the MR environment is challenged by the electromagnetic fields of the MR scanner, which restrict the use of typical measuring equipment in its vicinity, and may induce artefacts in acquired SOIs. Concurrent acquisition of the SOIs and MR signals will typically reduce these artefacts significantly, as the inducing electromagnetic fields are often kept constant or are not present during MR acquisition. Doing so, however, requires high degree of synchronization with the MR scanner[14], which is not trivial to obtain. These challenges can be circumvented by using the scanner for concurrent acquisition of both the SOI and MR signal.

Scanner-acquired SOIs with frequencies far from ω_L are heavily attenuated by the bandpass filters in the receive chain of the scanner (see Fig. 2.2). A solution to this is modulation of a carrier signal by the SOI, which facilitates transmission through the filters without attenuation, provided that the frequency of the carrier signal is within the passband of the filter. The demodulation, also done in the receive chain, will partially undo the modulation, and the SOI can be extracted from data acquired by the scanner's ADCs at sequence-specific intervals. The technique was initially suggested in a study by Hanson & Hanson[25], where custom hardware designed by Christian Hanson facilitated scanner-sampling of biomedical SOIs. The hardware was also used for the abstract in Appendix C.

This hardware does not facilitate scanner-sampling of all SOIs, with one example being k-space trajectories. Following Eq. 2.14, the position in k-space is dependent on the integral of applied gradients since the isodelay of the latest excitation pulse, and determining k-space trajectories therefore relies on a continuous measure of both gradients and RF pulses. While continuous sampling by the scanner is not feasible due to temporal gaps between acquisition periods, a possible solution is instead to generate a k-space trajectory signal from pre-processing of continuous sampled gradient and RF pulses, and sample this in synchrony with the MR signal.

Performing pre-processing allows in general for scanner-sampling of SOIs where, e.g., the available bandwidth or complicated dependencies prevent direct sampling. The necessary signal processing is, however, highly dependent on the individual SOI, and a common implementation is therefore not feasible. To facilitate sampling of such SOIs, a new circuitry was developed by Christian Hanson. This circuitry features a field programmable gate array (FPGA), and is capable of recording RF amplitude correlates and up to three input signals with frequencies up to 20 kHz. The FPGA facilitates flexible signal processing with minimal computation time, and the RF correlate allows determining timing and envelopes of RF pulses transmitted by a scanner. Christian Hanson implemented communication between sub-circuitries and interfacing

to circuitry inputs and outputs, while experimental specific features and signal processing were implemented by the PhD candidate. A summary of the circuitries applied in this thesis is given in Tab. 3.1.

Experiments investigating the fidelity of the FPGA-based circuitry are presented in a manuscript (Appendix A), where its ability to accurately sample test signals and encode these into carrier signals receivable by an MR scanner is documented. To demonstrate an application not supported by the previously developed hardware, the MR signal from a ^{1}H point-source during an EPI sequence was emulated, and compared to the signal and reconstructed images obtained from a physical point-like phantom. The magnetic field at the target position of the point-source was inductively measured, and used for frequency modulation of a carrier signal with frequency ω_0, that was transmitted wirelessly to the scanner. Transversal relaxation was emulated by the signal amplitude exponentially decaying with the experimentally determined T_2 of the physical point-like source. Ideal excitation was emulated by the signal being reset to full amplitude at each RF pulse detection. An overview of the experimental setup is shown in Fig. 3.1 and a supplementary discussion of detection and identification of RF pulses is given in Sec. 3.1.

Test signals extracted from scanner-acquired data after digitization and modulation by the circuitry, showed minimal distortions compared to the test signals concurrently sampled by an oscilloscope, indicating, that high-fidelity sampling of SOIs using the circuitry is feasible. The inductive measure of the scanner's magnetic field was affected by significant noise that limited the obtainable precision. Still, the emulated point-source was positioned accurately at the target position in the readout-direction, and within 96% accuracy in the phase-encoding direction. Putative applications of emulated point-source signals include motion sensing, sequence optimization, quality assurance, and signal quantification. These applications may be less demanding, with regards to the circuitry performance making the obtained precision applicable.

	Analogue hardware	FPGA-based circuitry
Input	8 analogue inputs, 1 sample-hold trigger	3 0–20 kHz inputs and 1 RF amplitude correlate, sampling rate: 200 kHz
Signal Processing	Flexible bandpass filtering, customizable signal-hold	Fully customizable, introduces signal delay
Output	8 mixed amplitude modulated carrier signals (10–130 MHz), variable amplification of the individual carrier signals	1 amplitude and/or frequency modulated carrier signal (10–130 MHz)
Other Connections	Optic cabling to computer for visualization of input signals and hardware control	Fully customizable bi-directional USB connection, e.g., custom user-inputs and offline visualization of sampled signals
Additional remarks	Analogue and does not rely on an internal clock, limited signal processing	Fully customizable, LCD display, input signals can be combined through signal processing, digital and rely on 40 MHz clock

Tab. 3.1. Summary of the hardware presented by Hanson & Hanson[25], and the circuitry presented in Appendix A. Both were fabricated by Christian Hanson, and optimized for scanner-sampling of different SOIs.

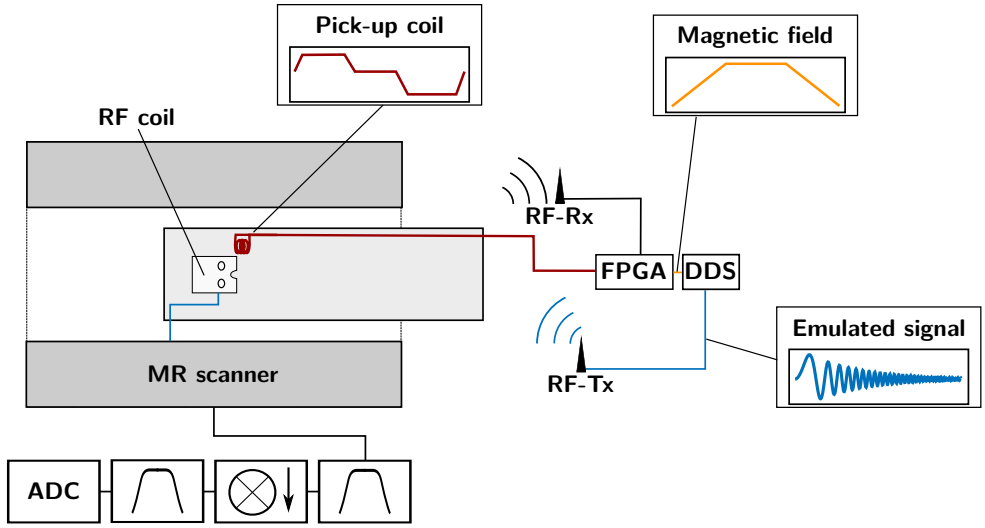

Fig. 3.1. Setup used for experiments presented in Appendix A. The inductively generated signal from a pick-up coil (red) placed in the gradient field of an MR scanner is transmitted to custom circuitry featuring an FPGA. The FPGA determines the magnetic field (yellow) at a target position, based on the inductive measure. A DDS sub-circuitry generates a carrier signal with exponentially decaying amplitude and frequency ω_0, that is frequency modulated by the magnetic field measure, and transmitted wirelessly to the RF coil of the MR scanner (blue) by a dipole antenna (RF-Tx). From here the signal is passed through the receive chain, yielding a point-source in the reconstructed images. The amplitude of the carrier frequency is reset to full strength at each detection of an RF pulse transmitted by the scanner, facilitated by an additional dipole antenna connected to the circuitry (RF-Rx). The signal modulated due to a trapezoidal gradient is depicted for the individual steps.

3.1 Detection of RF pulses

In the studies presented in Appendix A and Appendix B, a dipole antenna placed in the vicinity of the scanner was connected to the circuitry presented in Appendix A, to determine timing and amplitudes of RF pulses applied by the MR scanner. In these studies, only excitation pulses were applied, and distinguishing different types of RF pulses, e.g., excitation, refocusing, and inversion pulses, was therefore not of concern. For cases where this is necessary, RF pulses can potentially be distinguished by, e.g., maximum amplitude, shape, or timing compared to applied gradients, and classified by comparison with nominal values.

Another approach is to add characteristics to the different types of RF pulses. This would additionally allow for identifying specific timings inside an RF pulse, e.g., the isodelay point as shown in Fig. 3.2 for the RF pulse used in Appendix A (red). After a Dirac-Delta like function was added to the pulse shape in pulse programming, the RF pulse amplitude acquired by the circuitry (blue) showed a distinguishable feature. The effect of the added feature on the resulting slice profile was determined by Fourier transformation of the sampled pulse shape and was found to be insignificant. The effect might, however, be underestimated due to the temporal resolution offered by the circuitry, and should in all cases be validated for individual applications.

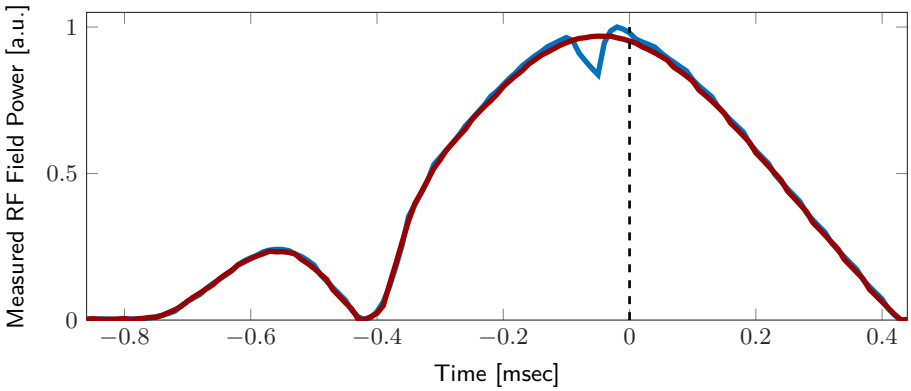

Fig. 3.2. The RF pulse shape used in the study presented in Appendix A as sampled by the circuitry. The used pulse shape (red) was modified to have a distinguishable feature right before its isodelay point (blue). The feature is clearly detectable by the circuitry (blue).

4 | Determination of k-Space Trajectory Errors

Play-out of gradient waveforms is used to traverse k-space, facilitating MR signal sampling at varying spatial frequencies as needed for image reconstruction. Deviations from nominal k-space trajectories (k-space trajectory errors) are commonly occurring in MRI and lead to image quality degradation and variation between images acquired by different scanners[26]. The effect of k-space trajectory errors on reconstructed images is highly dependent on the sampling scheme, and different approaches are used in dealing with these. The k-space trajectory errors can be formulated as an additional phase factor, $b(\mathbf{r}, t)$, in the signal equation:

$$s(k_x, k_y, b) \propto \int_x \int_y m(x, y) \exp(-\mathrm{i}\left[2\pi k_x(t)x + 2\pi k_y(t)y + b(\mathbf{r}, t)\right]) \, dx \, dy. \tag{4.1}$$

The presence of the k-space trajectory errors is often acknowledged by using trajectories, where their effect is limited. One example is Cartesian trajectories. As only a single constant gradient is typically active during signal readout, gradient trajectory errors can be approximated to only cause a translation of the k-space trajectory. While this leads to an error in reconstructed phase images, the amplitude images are unaffected[27],[28]. An exception to this is EPI, where the readout direction is alternated between each readout, and the direction of the translation is thereby shifting between even and odd readouts. This leads to limited blurring and distortions, but more importantly the N/2-ghosting artefact[29], which is typically accounted for by post-processing of the acquired data, rather than correcting the assumed k-space trajectory. The use of Cartesian trajectories has drawbacks, as also commented on in Sec. 2.3, and the widespread use of these can be ascribed to the effect of k-space trajectory errors being correctable, rather than being optimal regarding sampling of k-space.

For non-Cartesian trajectories, e.g., spiral imaging, k-space trajectory errors are a significant challenge, as they are not as easily accounted for in post-processing[30]. A more widely applicable approach is therefore to determine the errors and account for them in either reconstruction or when playing out gradient waveforms. In the following sections, typical causes of k-space trajectory errors will initially be described. Measurements of k-space trajectories can be applied to obtain better images in multiple ways, and examples of this will be presented in the second section. Depending on the nature of the k-space trajectory errors, different approaches for determining these have been proposed in literature. Some of these will be presented in the third section, which in addition introduces the study presented in Appendix B.

4.1 Causes of k-space trajectory errors

Gradient Amplifier Infidelity

Non-perfect gradient amplifiers cause distortions of the waveforms delivered to the gradient coils. While the amplifiers are typically tuned at installation to yield high-fidelity waveforms[31], temporal dependency due to, e.g., temperature drift, changing load of the amplifier, and unstable cooling and power supply, can result in degradation of the amplifier performance. The temporal instabilities are to some extent attenuated by internal feed-back control of the amplifier, but deviations from the nominal gradient waveforms often persist to some degree[32]. A typical result of the imperfections is an effective anisotropic delay between the actual and nominal gradient waveforms[33].

Eddy Currents

As described by Faraday's law, eddy currents are induced in conducting structures of a scanner, e.g., gradient coils and shim coils, by the temporally alternating gradient field. These currents leads to additional magnetic fields, $\mathbf{G}^E(t)$, in the order of $0.05\times$ the nominal gradient field, $\mathbf{G}(t)$[29]. Eddy currents are typically accounted for by pre-emphasis or avoiding them through shielding[34]. In determining a pre-emphasis, modelling the conducting structures of the scanner as RL[35] or RLC[36] circuits allows for approximation of the eddy currents as relatively long lived exponentially decaying currents. Based on such models, the nominal trajectory used in reconstruction can be updated to include eddy current effects, or the gradient driving current can be modified to cancel out the effects of eddy currents. This is to large extent done by scanner vendors, and both shielding and pre-emphasis are standard in modern commercial scanners, typically reducing eddy currents to the order of $0.005 \times \mathbf{G}(t)$[29]. Remaining eddy currents are primarily short lived and/or do not show linear time-invariant (LTI) behaviour, and are therefore difficult to model.

Mechanical Oscillations

The generation of $\mathbf{G}(t)$ causes Lorentz forces to act on the gradient coils[37], which results in vibrations of the coils. Besides causing the characteristic loud acoustic noises associated with MRI, the vibrations also lead to a similarly vibrating gradient field, and thereby imprecise k-space encoding. The vibrations are particularly challenging when gradient switching resonates with eigen-modes of the gradient system[38], and for fast-switching sequences, e.g., EPI[38] and diffusion imaging[37],[39],[40], where the Lorentz forces are largest. Compensating for the effect of the vibrations is difficult as it is dependent on the temperature and the age of the system, due to alterations of the physical properties of the gradient coils[41].

Heating

Besides indirect temperature dependencies of other listed factors, heating causes changes to the properties of the gradient coils and amplifiers, and thereby perturbations to the nominal gradient waveforms. Ohmic losses, and friction generated by mechanical vibration of the gradient coils generate thermal energy that increase the temperature of the gradient system, despite extensive

water cooling typically being applied[42]. Heating has been identified as a main contributor to dynamically changing behaviour of the gradients by, e.g., Foerster *et al.*[39], who included mechanical vibration and heating as reasons for phase drifts of MR signals during long scanning sessions, and Kasper *et al.*[43] who attributed the main reason for a linear dependency of the k-space trajectory root-mean-square (RMS) error to heating of the gradient system.

Concomitant Fields

Typically, the total magnetic field of a scanner is approximated as only consisting of a $\hat{\mathbf{z}}$-component, as also done in Eq. 2.1 and forward. In doing so, the relatively small field components in $\hat{\mathbf{x}}$- and $\hat{\mathbf{y}}$-directions created by the gradient coils, denoted the concomitant or Maxwell fields, are disregarded. This leads to an underestimation of the total magnetic field size, introducing an always positive phase error that increases with $B_G(\mathbf{r}, t)$, and therefore distance from isocenter[44]. The approximation is made despite the concomitant fields being fully described by Maxwell's equations, as it leads to a significant simplification of theory. The effects of the concomitant fields are particularly contributing when the gradient field is considerable relative to the total magnetic field, i.e., for low $\mathbf{B}_0$ fields strengths, and sequences with high gradient field strengths. While the size of the concomitant fields is relatively small, they can affect image quality, especially for EPI, where the small frequency difference between voxels in phase-encoding direction causes the concomitant fields to yield considerable spatial distortions[45].

4.2 Applications of k-Space Trajectory Measurements

Knowing k-space trajectories from high-fidelity measurements has several potential applications. Takahashi & Peters[46] showed that knowing the actual k-space trajectory can be used to optimize slice selecting RF pulses. Papadakis *et al.*[47] showed that the actual k-space trajectory can be used directly in reconstruction using discrete Fourier transformation. Doing so is, however, computationally demanding compared to FFT, which commonly is used for Cartesian k-space trajectories. As discussed in Sec. 2.3, the typical approach is therefore to resample non-Cartesian sampled data to a Cartesian grid.

Assuming the gradients are an LTI system, allows for determining the gradient impulse response function (GIRF), which maps the gradient's response to all relevant frequencies. In principle, hardware impulse responses can be determined, as the name suggests, by measuring the output from parsing an impulse. Due to hardware limitations, this is, however, not possible for a gradient system. Instead chirp-like[48] or triangular gradient waveforms[49] have been used. Knowing the GIRF, the scanner's time domain response to an arbitrary nominal gradient can be predicted by convolution and used to prospectively update the k-space trajectory[6], or pre-emphasizing the current to the gradient coils to account for errors[50]. Knowing the GIRF also allows for modifying the off-resonance reconstruction frequency during scanning, facilitating de-blurring of particular regions of interest[49].

Measuring the gradient field at multiple spatially distributed points enables compensation of spatial variations through fitting of spherical harmonics. This was initially suggested by Janke *et al.*[51] and experimentally shown by Barmet *et al.*[52] for zeroth and first order spherical harmonics and later up to 3rd order spherical harmonics[53].

4.3 Approaches for Determining k-Space Trajectories

Several approaches exist for determining k-space trajectory errors, as presented in the following subsections. The approaches typically vary with respect to underlying assumptions of the gradient field, which simplifies the experiments required for approximating the k-space trajectory errors. These approximations effectively limit the fidelity of the obtained trajectories, but as the experimental procedures typically are simplified significantly, evaluating the applicability of a certain method involves a weighting of precision versus complexity.

Delay Determination

Several studies have suggested to approximate the combined k-space trajectory errors as effectively reflecting a delay of the encoding gradient waveform. Characterization of k-space trajectory errors is thereby reduced to determination of a single time constant. Different approaches, typically specific for each traverse patterns, are used to determine this delay.

For EPI, a delay of the readout gradient is of particular concern, as it leads to ghosting artefacts in the phase-encoding direction[33]. The delay is commonly determined by acquiring multiple echoes without the phase encoding gradient, i.e., measuring the same k-space line multiple times with an alternating readout direction. After a 1D Fourier transform, a delay of the gradient waveform causes a phase discrepancy between data from opposite readout directions, from which it can be determined. Knowing the delay allows for compensation in post-processing, or preferably in the play-out of the gradient waveforms[33]. This approach is challenged by the phase of the acquired signal also being affected by $\mathbf{B}_0$ inhomogeneities and chemical shift. To overcome this, Reeder *et al.*[27] proposed repeating the entire scheme with inverse gradient polarity, allowing for isolating the delay.

For spiral imaging, a gradient delay causes blurring and/or distortions[54]. To determine the delay, Robison *et al.*[55] proposed to play out each gradient waveform with opposite polarity in repeated acquisitions. In doing so, they exploited, that a delay of the gradient waveforms leads to a time-shift of the MR signal amplitude peaks obtained at k-space zero crossings. Since the shift direction is opposite for the two polarities, the delay was determined from the difference in the time point of maximum signal amplitude. The method was expanded by Bhavsar *et al.*[54], allowing for playing out gradients in multiple encoding directions simultaneously.

Calibration-Based Trajectory Determination

If the gradient system acts as an LTI system, the actual k-space trajectory is identical for repetitions of a scan and k-space trajectory errors are spatially independent[56]. Multiple approaches rely on this assumption, as it allows for performing prescans from which the actual k-space trajectory, or the k-space trajectory error can be determined.

The peak-fitting method first proposed by Onodera *et al.*[57], and later modified by Takahashi & Peters[46] and Papadakis *et al.*[47] initially excites a thin slice of a large phantom, followed by play-out of a socalled self-encoding gradient and subsequent play-out of the gradient waveform of interest (test gradient). When the phase induced by the the self-encoding gradient is undone by the test gradient an echo is created, leading to a peak in the MR signal amplitude. By repeating the sequence for multiple sizes of the self-encoding gradient, a complete image of k-

space trajectory caused by the test gradient can be obtained. A function, e.g., a polynomial, can be fitted to the obtained waveform to obtain higher temporal precision than the dwell-time of the signal sampling rate. Using a similar experimental approach and performing a Fourier transformation of the MR data in the direction of the gradient waveform enables extraction of the phase, which facilitates a more robust fit as shown by Alley *et al.*[58].

Another approach relies on spatial limitation of the signal source. Duyn *et al.*[59] showed that by exciting a thin slice orthogonal to the test gradient, the transversal magnetization density can be approximated by a Dirac-Delta function. For a test gradient in the $\hat{\mathbf{x}}$-direction, for example, a slice in the yz-plane with position x_0 is excited. By turning off G_y (causing $k_y(t) = 0$), the signal as given by Eq. 4.1 becomes

$$s(k_x, b) \propto \int_x \int_y \delta(x - x_0) \exp(-\mathrm{i}\left[2\pi k_x(t)x_0 + b(t)\right]) \, dx \, dy \tag{4.2}$$

$$= C \cdot \exp\left[-\mathrm{i}2\pi(k_x(t)x_0 + b(t))\right], \tag{4.3}$$

where the $\mathbf{r}$-dependency of $b(t)$ is lost due to the LTI assumption. Defining $b(t) = b_G(t) + b_0(t)$, the phase of the signal becomes

$$\phi(t) = 2\pi k_x(t)x_0 + b_G(t) + b_0(t), \tag{4.4}$$

where $b_G(t)$ is caused by imperfections of the test gradient (e.g., eddy currents and hardware imperfections), and $b_0(t)$ is caused by remaining effects (e.g., $\mathbf{B}_0$ inhomogeneities, slice profile deviation from a Dirac-Delta function, and eddy currents from slice encoding gradients). The contribution from $b_0(t)$ can be determined by repeating the experiment without the test gradient, effectively setting $k_x(t) = 0$, thus resulting in

$$\phi(t) = b_0(t). \tag{4.5}$$

The method relies on the signal source being approximately a Dirac-Delta function, but it has in reality a thickness, Δx. For the approximation to hold, Δx must be smaller than $1/k_{FOV}$, where k_{FOV} is the range of spatial frequencies investigated. As the signal-to-noise ratio (SNR) is proportional to the volume of the source, this effectively limits the possible maximum spatial frequency determinable. Mason *et al.*[60] showed that point-like phantoms can be used to obtain similar measurements without the need for excitation of a slice. Despite this, Duyn's method is typically used in literature as it only requires a homogeneous phantom, and obtains accurate measurements in reasonable time.

An expansion to the approach of Mason *et al.*[60] is field probes, where each point-like source is equipped with its own receive coil, ensuring a high SNR for the individual point-like phantoms. The method yields a precise determination of actual k-space trajectories[61], but relies on expensive and complex equipment, and positioning of the field probes in a homogeneous $\mathbf{B}_0$ field. Field probes are further discussed in a following subsection.

The assumption of LTI behaviour of the gradient system have been investigated in multiple studies. Brodsky *et al.*[56] showed through improved image quality, that some k-space trajectory errors could be accounted for by assuming LTI behaviour, and remaining errors were on the order of 0.1 pixel in reconstructed images. However, they also found a temperature dependency of the gradient system performance, arguing for a per-scan calibration scheme. Research by Vannesjo *et al.*[62] suggest, that only a single calibration measurement is needed, as they found only slight image improvement when comparing the use of current and 3 years old calibrations. This was somewhat countered by Kasper *et al.*[43], who used Principal Component Analyses

(PCA) to investigate the evolution of the k-space trajectory errors on multiple time scales. They concluded that a day-to-day LTI based calibration would greatly reduce k-space trajectory errors, but leave heating induced errors of significant size. They found that this error could be reduced by an order of magnitude by using either a per-scan calibration prior to scanning, or by concurrently determining the k-space trajectory with MRI. The latter will be discussed in the following subsection.

Besides the described approaches, the k-space can with an LTI assumption also be determined using methodology developed for other purposes, such as through the PSF or through field mapping, as shown for EPI by Zeng & Constable[63]. While these methods are fully viable, they do not yield the k-space trajectory directly, and will not be commented on further.

Concurrent Trajectory Determination

For correction of k-space trajectory errors that follow from non-LTI behaviour of the gradient system, e.g., non-repeatable shot-to-shot variations and heating effects, it is necessary to determine k-space trajectories concurrently with MR acquisition. This can be accomplished with the use of field probes. These can either be excited by the same $\mathbf{B}_1$ as the imaged sample, or be excited by an external transmit chain[64]. The latter allows for RF shielding of the field probe, minimizing their interference with the main MR signal, but introduces additional eddy currents on these RF shields. An alternative approach is to use another nucleus in the field probes than in the imaged sample. This was done by Wilm *et al.*[53], who used ^{19}F-based field probes simultaneous with ^{1}H imaging, but in doing so, they relied on a separate additional receive chain for simultaneous sampling in the frequency range of both nuclei. Compared to, e.g., inductive measurements (discussed below), field probes benefit from not requiring integration to obtain a measure of a magnetic field, yielding a typical sensitivity of $<100\,\mathrm{fT/Hz^{3/2}}$[64].

Following Faraday's law, positioning a pick-up coil in a scanner's varying gradient field causes a voltage proportional to the time derivative of the field to be induced. A measure of the gradient field can therefore be determined by integrating the induced signal. Similar to field probes, this approach allow for concurrent imaging and monitoring of the gradient field, but does not yield a measure of the DC-component of the field. The integration of the induced signal can either be done in analog circuitry, yielding an analog field measurement, or be performed digitally after digitization of the coil-induced signal.

Multiple circuit designs facilitates analog integration, and two examples with flat transfer functions are shown in Fig. 4.1. These are referred to as feedback-flux and transimpedance integrators[65],[66]. In work by Senaj *et al.*[67] analog integration was performed by a transimpedance integrator, that in addition featured a reed relay to null the integrator at every TR. By combining two pick-up coils to create a gradiometer, they obtained a measure of the gradient, rather than the magnetic field strength. Imperfect components of the integrator introduced noise to the generated field measure, which limited the obtainable sensitivity to 10^{-4} times the applied gradient. Simulations of feedback-flux and transimpedance integrators, suggest a similar sensitivity of $<10\,\mathrm{nT/Hz^{0.5}}$ is theoretically obtainable for frequencies between 1 Hz and 20 kHz, with the performance being limited by the input voltage noise of the operational amplifier[65].

The manuscript in Appendix B documents the feasibility of concurrently acquiring MR data and inductively measuring k-space trajectories, using the circuitry presented in Appendix A to perform digital integration. The gradient measure was used to frequency modulate a carrier signal with frequency ω_0 transmitted to the MR scanner. This lead to a measure of the k-space

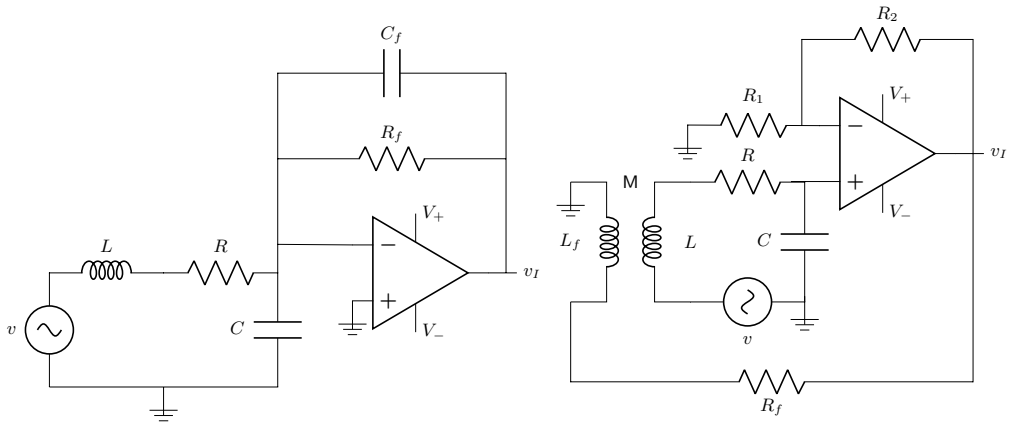

Fig. 4.1. Equivalent circuit of a transimpedance integrator (left), and a feedback-flux integrator (right), which both output an integrated signal (v_I) by applying an operational amplifier with positive and negative supply voltage, (V_+, V_-). A pick-up coil with resistance R, capacitance C and inductance L induces a voltage v when positioned in an oscillating gradient field. For the transimpedance integrator the induced voltage is fed to a transimpedance amplifier, stabilized by a capacitor (C_f). Similar performance is obtainable for a feedback-flux integrator by adding a feedback circuit (R_f and L_2, with L_2 and L_1 having mutual inductance M), and correct choice of amplification ($G = 1 + R_2/R_1$)[65].

trajectory being encoded into the cumulative phase of the signal acquired by the scanner. By performing digital integration an analog integrator and the noise induced by this was avoided, and signal processing, such as nulling of the integrator, became straight-forward. The dynamic range of the non-integrated signal was, however, larger than that of an integrated signal, and quantization errors became a primary noise-source.

In our early experiments, presented in an abstract at *The ISMRM 25th Annual Meeting & Exhibition, 2017*[68], an inductively determined k-space trajectory measure was encoded by amplitude modulation. The acquired measure was challenged by cumulative quantization noise, caused by an effective double integration performed in pre-processing as necessary for determining k-space trajectories from the inductive signal. This suggested, that the 16 bit sampling featured by the applied circuitry was insufficient to avoid significant quantization errors, which is also in accordance with the estimation of Senaj *et al.*[67], who estimated 20 bit sampling being necessary for obtaining a precision similar to that obtained using their analog integrator. While such sampling is facilitated by modern high-end ADC's, these are expensive and power consuming, making them ill-suited for battery-driven implementations.

In experiments presented in Appendix B a gradient measure was generated in pre-processing, and encoded by frequency modulation, facilitating extraction of a k-space trajectory measure from the cumulative phase of a scanner-acquired signal. For this approach, only a single integration was therefore done in pre-processing, which reduced the rate of noise accumulation significantly. The inductive measure was in addition regularized by measurements of the current running to the gradient coils, which further improved the k-space trajectory measure. An acquired EPI k-space trajectory was used for reconstruction of MR images, and showed better quality than images reconstructed using the scanner's assumed trajectory even after correcting these for a delay in the play-out of the causing gradient waveforms. For a spiral trajectory, where gradient field infidelities are not as easily corrected for, the regularized inductive measure yielded vastly

better images than those obtained from the delay-corrected, scanner-assumed trajectory. The applied experimental setup is summarized in Fig. 4.2.

While the fidelity of the regularized inductive measure is lower than that of field probes, it offers similar applications, namely fitting of spherical harmonics to multiple local gradient field measurements and concurrent acquisition with MR data. Contrary to field probes, the inductive measure is insensitive to $\mathbf{B}_0$, and the position of pick-up coils can be chosen with high flexibility. The necessary hardware is in addition simple compared to that necessary for high-fidelity field probe studies[69], potentially making it easy-to-use and an inexpensive approach to obtain concurrent k-space trajectory and MR signal acquisition.

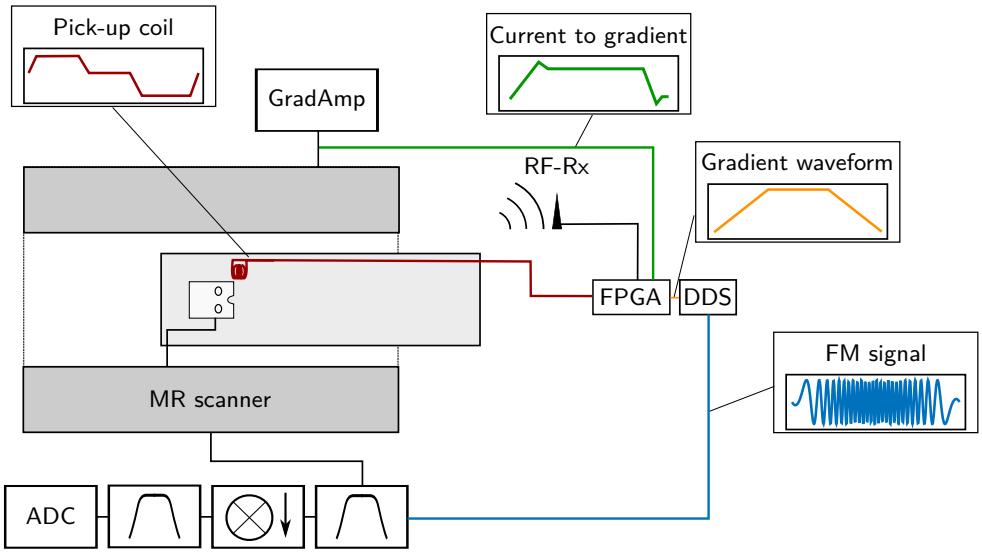

Fig. 4.2. Setup used for experiments presented in Appendix B. The inductively generated signal from a pick-up coil (red) placed in the gradient field of an MR scanner is transmitted to custom circuitry featuring an FPGA together with a measure of the current delivered to the gradient coil (green). The two signals are combined to a single measure of the applied gradient waveform by an FPGA (yellow). A DDS sub-circuitry generates a carrier signal with frequency ω_0, which is frequency modulated by the determined gradient waveform, and transmitted directly to a receive channel of the scanner. Determination of the gradient waveform is initialised by detection of an RF pulse by a dipole antenna position in vicinity of the scanner (RF-Rx). After demodulation performed by the scanner, the k-space trajectory is directly extractable from the cumulative phase of the received signal. The signal modulated due to a trapezoidal gradient is depicted for the individual steps.

5 | MR Scanner Acquisition of Speech During Imaging

Speech recording during MRI is beneficial for ensuring subject safety and for studying, e.g., gesticulation[70] and volumetric tracking[71] in the vocal tract. The strong magnetic field of an MR scanner makes use of ferromagnetic equipment to facilitate this, a safety risk. In addition, the changing gradient field and RF pulses necessary for imaging induce voltages in cabling and transducers placed in vicinity of scanners, potentially causing artefacts and signal clipping. Despite having been used in open-scanner studies[13],[72], general audio equipment is therefore typically not applied in the MR environment during scanning, and audio signals are instead typically encoded into non-affected signal carriers to transducers away from the scanner. Examples include an optic-based microphone[8],[12] and a non-metallic contraption fastened to the head of the subject that facilitates guided channelling of sound waves[73].

Recording of speech during imaging is also challenged by loud acoustic noise generated by the MR scanner. Lorentz forces acting on the gradient coils generate vibration in the auditory frequency range (0–20 kHz), generating noise that dominate speech. Methods to dampen the scanner-induced noise are typically dependent on restrictions to sequence design[74], and gradient noise is instead typically removed from mixed recordings of both speech and scanner-noise. One possibility is subtraction of noise recordings obtained from either initial scan repetitions without speech[12], or noise recordings acquired concurrently from a second microphone[8],[72],[73]. These approaches are challenged by the noise potentially not being identical for mixed and noise-only recordings, and speech being received by the intended noise-only microphone.

Noise and speech in mixed recordings can also be disentangled by computational signal processing. One approach relies on separation of noise and speech after inverse cepstral transformation[72]. Another approach is to determine parameters of a transfer function that fully describes the noise, effectively defining a filter that removes noise from mixed recordings. The coefficients of the filter can be determined from, e.g., noise-only recordings, or from harmonics of the repetition frequencies of applied gradient waveforms.[8],[73]. The latter approach relies on a high degree of synchronization between the gradient system and audio acquisition, which has been obtained from Transistor-transistor logic (TTL) pulses delivered by the scanner[73], or by accessing its master clock[8].

During individual sampling periods of most MR sequences, gradients are typically kept mostly constant. In these periods, noise generation and induction of artefacts in cabling and transducers are therefore limited. Speech recorded in synchrony with the MR signal is still contaminated by noise reflection and gradient waveforms stretching into the acquisition periods, but since the gradient waveforms are phase-locked to the scanner sampling, the recorded noise can be removed

through relatively simple signal processing. The necessary synchronization is directly obtained if the audio signal is recorded by the MR scanner.

This chapter documents the feasibility of concurrently acquiring audio and MR signals by an MR scanner. Sampling of an inductively transduced audio signal is facilitated by amplitude modulation, that allows for the signal to pass the filters in the scanner's receive chain unattenuated. The amplitude modulation is undone by the scanner before sampling, and the un-modulated audio signal can therefore be extracted from the raw data of the scan. By only sampling the audio signal in the MR readout periods, clipping of the sampled signal is to a large extent avoided, despite the use of a moving-coil microphone. Acquiring both the MR and acoustic signals by an MR scanner yields a high degree of synchronization between gradient shifting and audio sampling, which enables removal of gradient-induced noise by simple post-processing. Experimental procedures, signal processing and results from speech recordings performed during a Fast Low Angle Shot (FLASH) sequence are presented. This is followed by an overall discussion of recording MR and audio signals concurrently by an MR scanner. The performed experiments are also presented in the conference abstract in Appendix C, where the experimental setup is also depicted.

5.1 Materials and Methods

The membrane and attached loop coil of a dismantled 2" speaker was used as a moving-coil microphone by placing it in the MR scanner bore. A signal was thereby induced from audio-generated vibration of the membrane causing movement of the coil in the scanner's magnetic field. An additional identical coil was placed parallel and close to the one attached to the membrane. The coils were connected in series with opposite polarization, such that voltages generated in the coils by the alternating gradient field mostly cancel.

The microphone was connected to hardware developed by Christian Hanson and previously presented by Hanson & Hanson[25]. The hardware performed lowpass filtering of the audio signal (cutoff frequency: 25 kHz), before using this for amplitude modulation of a carrier signal with frequency equal to the scanner's reference frequency adjusted to ^{1}H (ω_0). The amplitude modulation assured unattenuated passage of the scanner's receive chain filters, and was undone by the following demodulation performed by the scanner (see Fig. 2.2). The hardware-generated signal was by wire transmitted continuously to the scanner during a FLASH sequence, but only sampled, when the MR signal was sampled (290×122 acquisition matrix, 5 slices, dwell-time: 9.9 µs, intervals between acquisitions: 9.87 ms, TE/TR: 4.6 ms/49.35 ms). The scan was performed twice, and in the second acquisition, gradient waveforms were turned off, such that no noise was generated. During both scans, a subject outside the scanner-bore uttered "Mary had a little lamb" continuously.

Initial experiments were performed on a 7 T Siemens Magnetom system ($\omega_0 = 297$ MHz). As the amplitude modulator was limited to outputting a maximum frequency of 130 MHz, the modulated signal was sent through a mixer, which performed a 200 MHz frequency shift of the amplitude modulated signal. This mixer was not thoroughly tested beforehand, and could potentially damage the MR system. The signal was therefore inductively transmitted between two closely positioned Ø3 cm loop coils, before reaching the receive channel, yielding galvanic isolation. Due to limited access to the 7 T system, later experiments and acquisition of presented data was done on a 3 T Philips Achieva system ($\omega_0 = 127$ MHz). Here, the additional mixer state and galvanic isolation were omitted.

After sorting data to chronological order, the first 20 samples of each acquisition, and the first 180 full acquisitions were discarded, as the signal here showed signs of being clipped. The contributions from the readout and phase-encoding gradients to noise in the audio recording were addressed separately. The readout gradient and its timing compared to the audio sampling was unchanged throughout the sequence, thus an identical contribution to each repeated readout was assumed. The induced noise was therefore approximated as the average across repeated readouts, and simply subtracted from the total recording. The noise generated by the phase-encoding gradient was assumed to scale with its amplitude, and thus linearly follow the phase-encoding table. The noise induced by the phase-encoding gradient was therefore approximated from a linear fit across readouts, and subtracted from the recording.

The audio signal was only sampled during MR signal acquisition, and not during, e.g., slice excitation, and phase-encoding, which lead to un-sampled periods in the obtained audio recording. Their relatively short duration allowed for assuming limited change in the characteristics of the uttered speech during these. For both acquired audio recordings, the gaps were therefore filled by autoregressive (AR) modelling (`fillgaps`[75], fitted over maximum 4000 samples, 100th order model). Residual noise was addressed by `Noise Reduction` algorithm in the open source sound editing software Audacity® 2.1.2[76].

5.2 Results

The acquired data before gradient noise removal (top), after removal of readout gradient noise (mid) and after additional removal of phase-encoding gradient noise (bottom) is depicted in Fig. 5.1 together with the noise removed in each step. The effect of readout gradient noise removal (subtraction of the average across horizontal lines in Fig. 5.1) is particularly visible for periods without speech (underlined in Fig. 5.1, top). Visible shadows scaling with horizontal distance from the central readout were addressed by removal of the phase-encoding gradient induced noise (subtraction of a linear fit across horizontal lines).

Fig. 5.2 depicts the speech recording before (red) and after (blue) autoregressive modeling to fill temporal gaps in the recording. For recorded periods, the blue curve is completely overlapping with the red curve. The top graph depicts the speech recording for two full utterances of "Mary had a little Lamb", and the lower graph depicts a single utterance of "Mary". Fig. 5.3 depicts the same recording after noise removal in Audacity. A clear relative reduction in signal amplitude is seen for periods without speech, e.g., in the period from 1850–2250 ms. Generated audio recordings are also available at `http://www.drcmr.dk/janop/Mary_had_a_Little_Lamb/`.

5.3 Discussion

MR scanner sampling of an audio signal was facilitated by amplitude modulation done by previously developed hardware. Experiments were performed simultaneously with ^{1}H imaging at both 3 T ($\omega_0 = 127$ MHz) and 7 T ($\omega_0 = 297$ MHz). For experiments at 7 T, an additional frequency shift was done to compensate for the maximum carrier frequency transmittable by the applied hardware being 130 MHz. Besides causing a decrease in signal amplitude, the frequency shift did not cause signal degradation. As only preliminary studies were performed using the frequency mixer, additional testing is necessary to further validate this claim. However, based

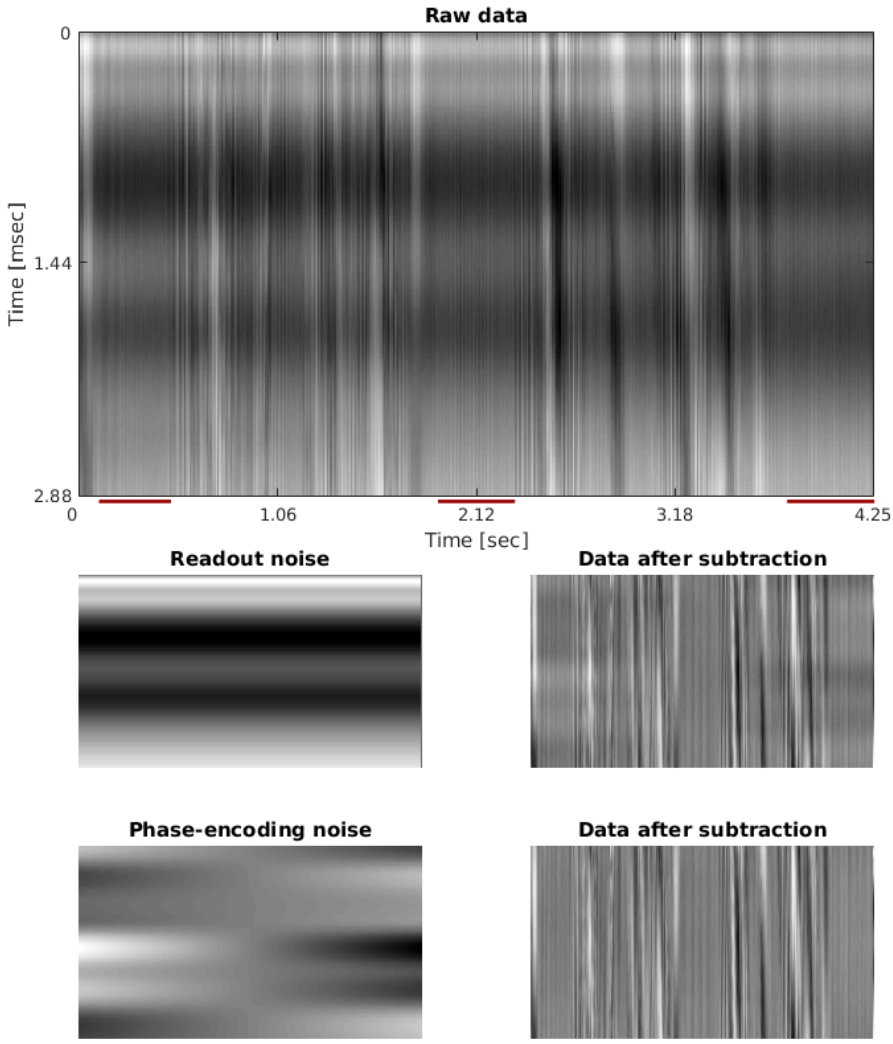

Fig. 5.1. The acquired, chronological audio signal after removal of clipped data acquisition (top), after removal of readout gradient noise (mid) and after removal of both readout and phase-encoding gradient noise (bottom). The signal contribution, that was subtracted in each step, is shown to the left, and the signal after removal is shown to the right. The red lines below the top spectrum depict periods without speech. Individual acquisitions are shown in the up-down direction, and the total readout time of the sequence is depicted in the left-right direction.

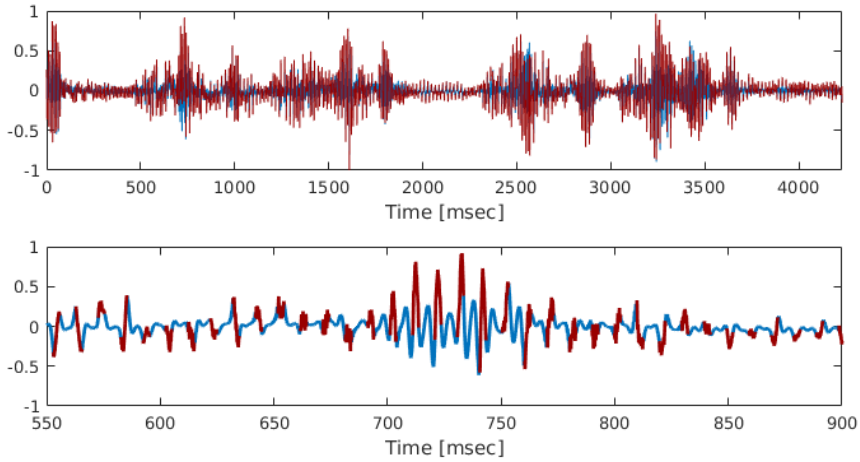

Fig. 5.2. Acquired speech recording after removal of gradient noise. Two utterances of "Mary had a little lamb" is depicted in the top graph, and a single utterance of "Mary" is depicted in the lower graph. The signal after AR-modelling (blue) is completely overlapping with the signal acquired by the scanner (red) during readout periods.

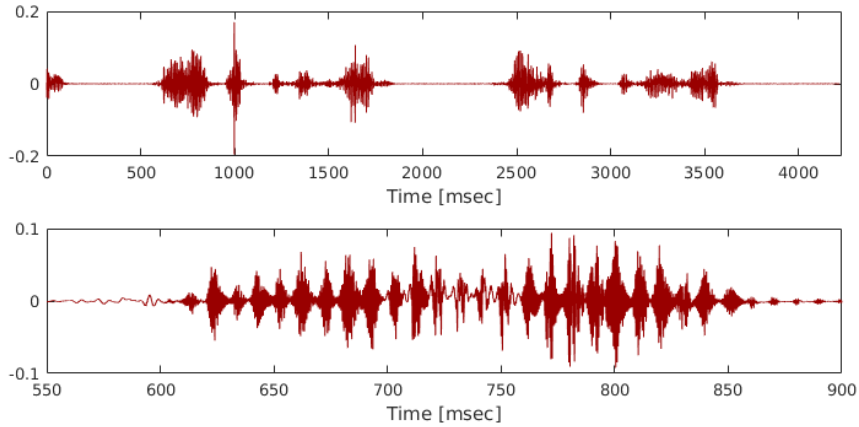

Fig. 5.3. The acquired signal after noise removal in Audacity. Two utterances of "Mary had a little lamb" is depicted in the top graph, and a single utterance of "Mary" is depicted in the lower graph.

on current experiences the method is expected to be generally viable, and thus also for sampling of non-audio signals at frequencies outside the range offered by modulating hardware.

The experiments performed with and without concurrent gradient waveforms yielded similar fidelity of speech recordings. The relatively simple noise-removal algorithm applied was therefore found sufficient for removing scanner noise from the acquired mixed recordings. The signal processing relied on a high degree of phase-locking between the noise source and the signal sampling, and on the noise scaling linearly with gradient amplitude. The performance in the initial steps of the noise removal algorithm confirms this being a valid assumption for acquired data. The performance of the noise-removal algorithm additionally suggest that gradient noise can be approximated from data acquired over a limited time window, and non-stationarities emerging for longer acquisitions may potentially be addressable by a sliding-window approach.

The applied FLASH sequence had an acquisition duty cycle of 30%, and gaps in the acquired speech recording were filled by AR-modelling done after removal of scanner noise. The non-equidistant sampling of the raw data prevents the direct use of filters developed under assumption of equidistant sampling, and makes the use of most signal processing algorithms infeasible. While the initial noise-removal and subsequent AR-modelling yielded recognizable speech recordings, performing AR-modelling before noise removal impairs the speech recording fidelity significantly. Obtaining equidistant sampling through AR-modelling to facilitate the use of other noise removal algorithms is therefore unlikely to be favourable.

Using sequences with a larger sampling duty cycle than the FLASH sequence used in the performed experiments, will lead to less signal being determined from AR-modelling, and likely increased audio quality. A candidate that additionally offers fast imaging is EPI, despite requiring larger gradient field strengths, and thus possibly causing extended signal clipping. This might be addressed by using another transducer than the microphone fabricated for these proof-of-concept experiments. Closer positioning of the two loop coils in the microphone is likely sufficient to avoid signal clipping, and using a better suited basis for the microphone than the applied speaker components is likely beneficial for the obtainable audio fidelity. Alternatively, other microphone types, such as optic-based or piezo-element based microphones, can alleviate the need for gradient field compensation. While the larger sampling duty cycle of EPI will reduce the acquisition dead time, the use of, e.g., Sweep Imaging With Fourier Transformation (SWIFT)[77], or Simultaneous RF Transmission and Reception (STAR)[78], can further reduce or completely remove gaps in the acquired signal by facilitating scanner-sampling concurrent with excitation. These methods are, however, still in early development, and not supported by typical MR scanners. The obtained contrast weighting of the acquired images may in addition be limiting their use.

In other studies, synchronization between gradient waveforms and audio sampling was obtained by accessing the scanner's master clock[8], and by using TTL pulses[73]. In previous experiments using the applied 3 T system, insufficient fidelity of generated TTL pulses limited the obtainable synchronization. In addition, pulse programming was necessary to enable these, limiting the general applicability across different scanners and vendors. Accessing the scanner's master clock enables similar synchronization as obtained in this study while also facilitating continuous sampling, and gaps in the audio recording are avoidable. However, a challenge arises from down-sampling of the master clock being necessary for triggering of typical audio-recording equipment[8]. The down-sampling ratio and access to the master clock is highly dependent on the individual scanner and applied audio sampling equipment, and considerable work is therefore associated with implementation on different scanners or changing audio sampling equipment. While yielding lower fidelity speech recordings, the implementation proposed here is only reliant on the scanner's receive chain filters, and can be implemented with knowledge solely of the

scanner's assumed Larmor frequency and characteristics of the applied sequence. It is speculated, that with further development, an increased audio fidelity is obtainable by scanner-sampling, despite challenges arising from discontinuous temporal sampling.

In summary, an inductively generated audio signal was amplitude modulated and sampled by an MR scanner concurrently with MRI. Gradient-induced noise and voltages were limited, as audio sampling was done only in MR readout periods. Residual noise was phase-locked to the signal sampling, and was therefore removable by simple post-processing. Gaps in the acquired audio recording were addressed by autoregressive modelling. Audible speech recordings were obtained, thus showing the feasibility of obtaining speech recordings by scanner sampling concurrently with MRI.

6 | Discussion

Throughout this thesis the feasibility of acquiring non-MR signals by an MR scanner has been explored. Considerations regarding experimental procedures were made in an effort to optimize these for individual SOIs. In the following, the differences and implications of different procedures are discussed from a general point of view.

Wired versus Wireless Transmission

The layout of an MR scanner's hardware prevents access to individual components, and direct transmission of an SOI to the scanner's ADC is therefore typically not possible without major alterations to the scanner. SOIs can instead be injected upstream of the receive channel with relative ease, and two approaches for doing so were investigated in this thesis. One approach is wireless transmission to the scanner's RF coil. The other approach is wired transmission directly to a receive channel, i.e., injection between the pre-amplifier and the first bandpass filter of the receive chain.

If an SOI-modulated carrier signal is wirelessly transmitted concurrently with MRI, a mixed MR and non-MR signal is received by the scanner. The signals can be disentangled in post-processing, provided that the two signals are not spectrally overlapping. Typically, an MR scanner acquires samples at a faster rate than necessary for imaging, and performs bandwidth reduction as part of reconstruction. The oversampling effectively yields a bigger FOV than requested by the user, while the following bandwidth reduction crops the FOV to the requested size. In the work of Hanson *et al.*[15], this was exploited by using carrier frequencies within the sampled bandwidth but outside the reduced frequency range. The SOIs were thereby cropped from images presented to the user, but accessible in raw data of the scan, and spectral overlap between the MR signal and the SOI was avoided.

An emulated point-source signal was similarly transmitted wirelessly in experiments presented in Appendix A. The limited spatial extent of a point-source typically allows for choosing a target position outside the imaged object, but within the requested FOV. For concurrent MR and emulated signal acquisition, these can thus be disentangled despite the frequencies of the emulated signal being within the scanner's reduced bandwidth. The available bandwidth is typically smaller than that offered by encoding in the oversampled frequency range, but the possibility of encoding an SOI into the images presented to the user is potentially beneficial. Examples include encoding of scalar measurements in the intensity of the point-source, such as temperature measurements, and reference signals for quantitative MRI. Solving the Bloch equations in real-time, using nominal or measured k-space trajectories, facilitates emulation of more advanced geometries than a point-source[79],[80], potentially increasing the available

bandwidth.

In the studies presented in Appendix B and Appendix C, SOIs were transmitted to a single receive channel of a scanner by wire. Mixing of the SOI and MR signal was thereby avoided as the receive channel was not available for MR signal acquisition, and the full bandwidth of the receive channel was available for acquisition of SOIs. To verify coil connections before scanning, an MR scanner sends a low-voltage signal through the receive chain to the RF coil. As the circuits used in Appendix B and Appendix C were not matched to correct resistance, this verification failed, and signal from the applied circuitry was not acquired. To avoid this, a matched resistor was therefore added in parallel with the circuitry, and the coil verification was passed. While this solution was applicable across scanners and vendors, it can be avoided by correct matching of the circuitry. This would in addition lower the reflected power, and thus allow for reducing the power usage of the circuitry without loss of SNR in the acquired signal. Depending on the applied MR receive coil and the number of available receive channels, wired transmission potentially lowers the SNR of the acquired MR signal, but for newer MR systems, featuring 32 or more channels, this loss is limited. While a wired transmission yields higher bandwidth and SNR than wireless transmission, it is also more invasive to the scanner setup, making experimental procedures more cumbersome.

Overall, the three presented approaches are viable for all typical MRI sequences. However, particularly for wireless transmission of emulated MR signals, an incorrect coupling of the transmitting antenna to the scanner's RF coil, compared to that of a physical signal source, presents a potential challenge, since it may implicate reconstruction algorithms used for, e.g., parallel imaging. This may lead to a need for adapting experimental procedures, such as moving the antenna, or avoiding signal transmission during determination of the RF coil's sensitivity maps. In general, non-MR signal transmission should should be avoided during prescans, unless being specifically necessary, as it may cause incorrect scanner adaptation to the prescans, which may cause artefacts in reconstructed images.

Amplitude Modulation versus Frequency Modulation

Carrier signals were modulated by SOIs to facilitate MR scanner-sampling of the SOIs. Amplitude modulation, as done for encoding of speech recordings in Appendix C, allows for directly extracting SOIs from the amplitude of the scanner's acquired data. Amplitude modulation was employed by the previously developed hardware, that in addition performed simple filtering of the SOI before modulation. Compared to frequency modulation, a lower SNR is obtained with amplitude modulation, as this is directly proportional to the signal amplitude. However, for acquisitions that require Fourier transformation for disentangling an SOI from an MR signal, amplitude modulation allows for the modulated carrier frequency to have an integer number of oscillations over each readout period, and ringing effects can thereby be avoided[15].

The study presented in Appendix B utilized frequency modulation to encode k-space trajectory measures in scanner-acquired data, facilitated by the circuitry presented in Appendix A. Frequency modulation was chosen for encoding of this SOI, as it allows for a constant high carrier signal amplitude, yielding a consistently high SNR. Extraction of a frequency modulated signal is typically more cumbersome than extraction of amplitude modulated signals, but this was here exploited, as it allowed for extracting k-space trajectories directly from the cumulative phase of a signal modulated by gradient measures. By doing so, only a single integration was necessary in pre-processing, which lead to a significant increase in SNR compared to initial studies, where a double integration was done to facilitate encoding by amplitude modulation[68].

For emulation of an MR signal, both frequency and amplitude modulation is necessary to correctly depict gradient-dependent precession frequency and relaxation-dependent amplitude. In Appendix A, where a point-source was emulated, the frequency modulation was dependent on simultaneously obtained gradient field measures, and the amplitude modulation was as an exponential function with a user-defined exponent. As evident from the experiments presented in this thesis, the optimal choice of modulation to facilitate scanner acquisition is highly dependent on the individual SOI, and whether it is mixed with the MR signal. Together with varying necessary pre-processing, this complicates the development of a common implementation applicable for multiple SOIs.

Signal Processing

Performing various degrees of signal processing before and after transmission to the scanner typically leads to an increased fidelity of SOIs. For the audio recording done in Appendix C, lowpass filtering was performed prior to transmission to the MR scanner to reduce noise in the scanner-acquired signal and could as-well be done in post-processing. The primary signal processing was done after scanner-acquisition, which facilitated the use of non-causal filters for removal of gradient-induced noise. The limited necessary pre-processing allowed for using the hardware of Hanson & Hanson[25].

While the circuitry presented in Appendix A potentially can perform similar pre-processing, the necessary programming of the FPGA to facilitate this is not trivial. This circuitry is instead better suited for sampling of SOIs not facilitated by the hardware of Hanson & Hanson[25], typically SOIs that benefit from pre-processing beyond simple filtering. One example is the k-space trajectory measure determined in Appendix B. Separate measures of the gradient field were pre-processed and combined through a cumulative sum, initiated by an RF-correlate measure surpassing a threshold. The generated k-space trajectory signal can be sampled concurrently with an MR signal, and can potentially facilitate a general reconstruction without the need for passing the sequence diagram from the host computer to the reconstructor. Other SOIs may benefit from occupying less of the scanner's bandwidth, if pre-processing is done, potentially facilitating the use of wireless transmission instead of wired transmission. As the signal processing introduces a limited signal delay ($\approx$ 15 µs), real-time implementations, such as encoding emulated MR signals in the images presented to the user as done in Appendix A, are still facilitated even when extensive pre-processing is performed.

The flexibility of the circuitry presented in Appendix A argues for the use of FPGA-based solutions for facilitating scanner-acquisition of non-MR signals, as this allows for reusing features such as offline visualization on a computer, carrier signal generation, and user-input interface across implementations. Enabling scanner-sampling of SOIs is thereby reduced to implementation of the necessary pre-processing, potentially from multiple input signals. For scanner-induced SOIs, the delay through the circuitry is a potential limitation, as it can correspond to several dwell-times of the scanner's sampling. A large contributor to the delay is digitization performed by the ADCs of the circuitry, and can thus be reduced by implementing faster digitizing ADCs at the cost of, e.g., less linearity, fewer sampled bits, increased power consumption and/or increased expense. Another possible approach is implementing a higher clock frequency of the FPGA than the current 40 MHz. A higher quality crystal to drive this clock will also yield more stable generation of carrier frequencies, which in Appendix B was limiting the circuitry's performance. Further development of the circuitry, e.g., parallel transmission between sub-circuitries, can possibly bring the delay below a single dwell-time of the scanner. This would, however, require extensive modification to the circuitry presented in Appendix A,

but is worth consideration for future generations of circuitry facilitating sampling of SOIs by MR scanners.

Critical sampling of the scanner's RF pulses is not facilitated by the presented circuitry, and only sampling of RF amplitude correlates is performed. The typical bandwidths of MR signals and RF pulses, potentially allow for sampling of these by a 20 kHz-input after performing a demodulation. This is, however, likely challenged by clock drift between the scanner's master clock and the clock driving the demodulation, which may introduce unacceptable artefacts depending on the intended use-cases. A putative solution is to undo the demodulation by a modulation driven by the same clock, effectively undoing any effect of clock drifts, and artefacts are avoided. Similar signal processing to what is done by current circuitry can potentially be performed between the modulation and demodulation. This may for example facilitate including the effects of non-excitatory RF pulses in emulated MR signal sources.

7 | Conlusion

Concurrent MRI and non-MR signal sampling by MR scanners was explored through several studies presented in this thesis. Different examples of non-MR signals of interest (SOIs) were acquired, with experimental procedures adapted to optimize bandwidth, signal-to-noise ratio, signal processing, and accessibility of the acquired data. The SOIs had vastly different characteristics, but all benefited significantly from being sampled in synchrony with the MR signal.

Speech recording concurrent with MRI is challenged by the electromagnetic fields of the scanner inducing artefacts if transducers or cabling are placed in vicinity of the scanner, and by acoustic noise generated by the gradient coils. For the study presented in Appendix C, a custom inductive microphone was fabricated, and by using the MR scanner for sampling of a carrier signal that was amplitude modulated by the audio signal, gradient-induced noise could be filtered out using simple post-processing. Audible speech recordings were thereby obtained concurrently with imaging using a Fast Low Angle Shot (FLASH) sequence, despite gradient-induced noise dominating speech in the non-processed audio signal. The obtainable audio fidelity is challenged by gaps between MR acquisition periods, e.g., during excitation, which was addressed by autoregressive modelling. These gaps are minimal for sequences with high sampling duty cycle, such as EPI.

In a second study presented in Appendix A, an MR signal from a point-source was emulated from measured gradient waveforms and RF pulse amplitudes. The emulated point-source served as an example application of custom circuitry developed to facilitate MR scanner sampling of SOIs benefiting from extensive processing before transmission to the scanner. Gradient field induced alterations to the precession frequency were emulated by frequency modulation, and T_2 relaxation was emulated by amplitude modulation. The emulated signal yielded a point-like structure in scanner-reconstructed images.

Emulation of MR signals has multiple potential uses. Similar to Electronic Reference To access In vivo Concentrations (ERETIC), which facilitates quantification by comparison of MR signal peak intensities to a known emulated signal, point-source emulation allows for quantitative MRI by generating a known signal intensity in reconstructed images. An emulated reference signal facilitates great flexibility in positioning, signal strength and relaxation rate compared to a physical phantom. Other signals can also be encoded into the intensity of the reconstructed signal, e.g., temperature measurements or paradigm variables in functional MRI. Multiple point-like sources emulated from field measures generated by transducers fastened to a moving object, e.g., a subject's head, are usable for motion referencing, particularly applicable for low-signal imaging such as diffusion weighted imaging and low gamma-imaging, e.g., imaging of ^{13}C and ^{23}Na. Spectral overlap between an actual and emulated MR signal is also feasible, e.g.,

for augmented MRI. With extensive knowledge of both the gradient and RF fields, signals of particular coherence pathways can be emulated, which is applicable for scanner diagnostic purposes and sequence development.

In a third study presented in Appendix B, k-space trajectories were acquired using the MR scanner during sequences where reconstruction based on the scanner's nominal k-space trajectory lead to artefacts in reconstructed images. A carrier signal was frequency modulated by the generated k-space trajectory measure and sampled by the MR scanner, yielding synchronized sampling of the MR signal and k-space position. Extensive pre-processing of multiple inputs yielded an accurate regularized inductive k-space trajectory measure, which enabled reconstructions with limited artefacts compared to images reconstructed using the scanner's nominal trajectories. Field probes have in other studies also been used for concurrent MRI and k-space trajectory acquisition, and compared to these, the generated measure offers better robustness against field inhomogeneities, and independence of temperature and coherence times, as it does not rely on the acquisition of a free induction decay (FID). A change in the imaged nucleus is easily handled, as it simply requires updating the circuitry-assumed gyromagnetic ratio. The presented method requires little extra hardware, and provides an experimentally simple and inexpensive approach to obtaining concurrent MR and k-space trajectory acquisition.

In studies using the circuitry presented in Appendix A, RF measurements were limited to determining the envelope of RF pulses transmitted by the scanner. This allowed for distinguishing RF pulse timings and determination of the acquired SOIs by assuming nominal responses to applied RF pulses. Other SOIs, particularly of relevance for scanner-monitoring, may be highly dependent on RF pulses, and assuming nominal responses may therefore be limiting to the obtainable SOI fidelity. High-fidelity RF measurements would, for example, permit expanding experiments performed in Appendix B to account for the effect of refocusing and inversion RF pulses, yielding a general applicable method for measuring k-space trajectories. For emulation of MR signals, as done in Appendix A, determination of the induced effect of applied RF pulses would facilitate emulation of only specific echo pathways, which is not directly feasible with physical phantoms.

Determining the RF response is possible from critical sampling of RF pulses, but requires faster sampling rate than currently facilitated by any of the applied circuitries. It is speculated, that the limited bandwidth of typical RF pulses would allow for full characterization of these if the circuitry-acquired RF signal is demodulated before sampling. If the same reference oscillator is used for a following modulation during transmission, phase drifting compared to the scanner may be avoided. Such expansions would be valuable for the general applicability of the circuitry, and a putative candidate for further development of circuitry facilitating scanner-recording of non-MR signals.

Bibliography

1. Smith-Bindman, R., Miglioretti, D. L. & Larson, E. B. Rising use of diagnostic medical imaging in a large integrated health system. *Health Affairs* **27,** 1491–1502 (2008).
2. Rosen, B. R. & Savoy, R. L. FMRI at 20: Has it changed the world? *NeuroImage* **62,** 1316–1324 (2012).
3. Le Bihan, D., Poupon, C., Amadon, A. & Lethimonnier, F. Artifacts and pitfalls in diffusion MRI. *Journal of Magnetic Resonance Imaging* **24,** 478–488 (2006).
4. Delattre, B. M. A., Heidemann, R. M., Crowe, L. A., Vallée, J. P. & Hyacinthe, J. N. Spiral demystified. *Magnetic Resonance Imaging* **28,** 862–881 (2010).
5. Zhang, Y., Hetherington, H. P., Stokely, E. M., Mason, G. F. & Twieg, D. B. A novel k-space trajectory measurement technique. *Magnetic Resonance in Medicine* **39,** 999–1004 (1998).
6. Addy, N. O., Wu, H. H. & Nishimura, D. G. Simple method for MR gradient system characterization and k-space trajectory estimation. *Magnetic Resonance in Medicine* **68,** 120–129 (2012).
7. Gotman, J., Kobayashi, E., Bagshaw, A. P., Bénar, C. G. & Dubeau, F. Combining EEG and fMRI: A multimodal tool for epilepsy research. *Journal of Magnetic Resonance Imaging* **23,** 906–920 (2006).
8. Bresch, E., Nielsen, J., Nayak, K. & Narayanan, S. Synchronized and noise-robust audio recordings during realtime magnetic resonance imaging scans. *The Journal of the Acoustical Society of America* **120,** 1791–1794 (2006).
9. Lewis, C. E., Prato, F. S., Drost, D. J. & Nicholson, R. L. Comparison of respiratory triggering and gating techniques for the removal of respiratory artifacts in MR imaging. *Radiology* **160,** 803–810 (1986).
10. Van Audekerkea, J., Peeters, R., Verhoye, M., Sijbers, J. & Van der Linden, A. Special designed RF-antenna with integrated non-invasive carbon electrodes for simultaneous magnetic resonance imaging and electroencephalography acquisition at 7T. *Magnetic Resonance Imaging* **18,** 887–891 (2000).
11. Mattei, E. *et al.* An optically coupled sensor for the measurement of currents induced by MRI gradient fields into endocardial leads. *Magnetic Resonance Materials in Physics, Biology and Medicine* **28,** 291–303 (2015).
12. NessAiver, M. S., Stone, M., Parthasarathy, V., Kahana, Y. & Paritsky, A. Recording high quality speech during tagged cine-MRI studies using a fiber optic microphone. *Journal of Magnetic Resonance Imaging* **23,** 92–97 (2006).
13. Pribil, J., Pribilová, A. & Frollo, I. Analysis of spectral properties of acoustic noise produced during magnetic resonance imaging. *Applied Acoustics* **73,** 687–697 (2012).

14. Anami, K. *et al.* Stepping stone sampling for retrieving artifact-free electroencephalogram during functional magnetic resonance imaging. *NeuroImage* **19,** 281–295 (2003).

15. Hanson, L. G., Lund, T. E. & Hanson, C. G. Encoding of electrophysiology and other signals in MR images. *Journal of Magnetic Resonance Imaging* **25,** 1059–1066 (2007).

16. Gruetter, R. *Automatic, localized in Vivo adjustment of all first- and second-order shim coils* 1993.

17. Banks, W. P. & Company, H. Nutation Angle Measurement During Mri Prescan. *Search,* 3–6 (1980).

18. Feiweier, T., Heubes, P. & Speckner, T. Method and magnetic resonance system for adjustment of the field strength of RF pulses. *United States Patent* (2009).

19. Nishimura, D. G. *Principles of Magnetic Resonance Imaging* 1.1 (Lulu, 2010).

20. Bernstein, M. A., King, K. F. & Zhou, X. J. *Handbook of MRI Pulse Sequences* (2004).

21. Mareci, T. H. & Brooker, H. R. Essential considerations for spectral localization using indirect gradient encoding of spatial information. *Journal of Magnetic Resonance (1969)* **92,** 229–246 (1991).

22. Pipe, J. G. & Menon, P. Sampling density compensation in MRI: Rationale and an iterative numerical solution. *Magnetic Resonance in Medicine* **41,** 179–186 (1999).

23. Scott, G. C. *MRI Transmit/Receive Chains* in *Proceedings 23rd Scientific Meeting, International Society for Magnetic Resonance in Medicine* (2015).

24. Jezzard, P., Matthews, P. M. & Smith, S. M. *Functional MRI: An Introduction to Methods* (Oxford Medical Publications, 2003).

25. Hanson, L. & Hanson, C. *A multi-frequency amplitude modulator for encoding electrical signals in MR images* in *Proceedings 14th Scientific Meeting, International Society for Magnetic Resonance in Medicine* (2006), 2388.

26. Jovicich, J. *et al.* Reliability in multi-site structural MRI studies: Effects of gradient non-linearity correction on phantom and human data. *NeuroImage* **30,** 436–443 (2006).

27. Reeder, S. B., Atalar, E., Faranesh, A. Z. & McVeigh, E. R. Referenceless interleaved echo-planar imaging. *Magnetic Resonance in Medicine* **41,** 87–94 (1999).

28. Jung, Y., Jashnani, Y., Kijowski, R. & Block, W. F. Consistent non-cartesian off-axis MRI quality: Calibrating and removing multiple sources of demodulation phase errors. *Magnetic Resonance in Medicine* **57,** 206–212 (2007).

29. Jezzard, P., Barnett, A. S. & Pierpaoli, C. Characterization of and correction for eddy current artifacts in echo planar diffusion imaging. *Magnetic Resonance in Medicine* **39,** 801–812 (1998).

30. King, K. F., Ganin, A., Zhou, X. J. & Bernstein, M. A. Concomitant gradient field effects in spiral scans. *Magnetic Resonance in Medicine* **41,** 103–112 (1999).

31. Connell, I. *Gradient Drivers: Amplifier Considerations, Power, Tuning, & Cooling* in *Proceedings 25th Scientific Meeting, International Society for Magnetic Resonance in Medicine* (2017).

32. Lai, R., Sabate, J., Chi, S. & Skeffington, W. High performance gradient driver for magnetic resonance imaging system. *IEEE Energy Conversion Congress and Exposition: Energy Conversion Innovation for a Clean Energy Future, ECCE 2011, Proceedings,* 3511–3515 (2011).

33. Davies, N. P. & Jezzard, P. Calibration of gradient propagation delays for accurate two-dimensional radiofrequency pulses. *Magnetic Resonance in Medicine* **53,** 231–236 (2005).

34. Mansfield, P. & Chapman, B. Active magnetic screening of coils for static and time-dependent magnetic field generation in NMR imaging. *Journal of Physics E: Scientific Instruments* **19,** 540–545 (1986).

35. Boesch, C., Gruetter, R. & Martin, E. Temporal and spatial analysis of fields generated by eddy currents in superconducting magnets: optimization of corrections and quantitative characterization of magnet/gradient systems. *Magnetic Resonance in Medicine* **20,** 268–284 (1991).

36. Zur, Y. & Stokar, S. An algorithm for eddy currents symmetrization and compensation. *Magnetic Resonance in Medicine* **35,** 252–260 (1996).

37. Gallichan, D. *et al.* Addressing a systematic vibration artifact in diffusion-weighted MRI. *Human Brain Mapping* **31,** 193–202 (2010).

38. Tomasi, D. G. & Ernst, T. Echo planar imaging at 4 Tesla with minimum acoustic noise. *Journal of Magnetic Resonance Imaging* **18,** 128–130 (2003).

39. Foerster, B. U., Tomasi, D. & Caparelli, E. C. Magnetic field shift due to mechanical vibration in functional magnetic resonance imaging. *Magnetic Resonance in Medicine* **54,** 1261–1267 (2005).

40. Hiltunen, J. *et al.* Quantification of mechanical vibration during diffusion tensor imaging at 3 T. *NeuroImage* **32,** 93–103 (2006).

41. Vannesjo, S. J. *et al.* Gradient system characterization by impulse response measurements with a dynamic field camera. *Magnetic Resonance in Medicine* **69,** 583–593 (2013).

42. Chronik, B. A. *Gradient Train: Power Amplification Through Chiller Requirements* in *Proceedings 23rd Scientific Meeting, International Society for Magnetic Resonance in Medicine* (2015).

43. Kasper, L. *et al.* Monitoring, analysis, and correction of magnetic field fluctuations in echo planar imaging time series. *Magnetic Resonance in Medicine* **74,** 396–409 (2015).

44. Bernstein, M. A. *et al.* Concomitant gradient terms in phase contrast MR: Analysis and correction. *Magnetic Resonance in Medicine* **39,** 300–308 (1998).

45. Weisskoff, R. M., Cohen, M. S. & Rzedzian, R. R. Nonaxial whole–body instant imaging. *Magnetic Resonance in Medicine* **29,** 796–803 (1993).

46. Takahashi, A. & Peters, T. Compensation of multi-dimensional selective excitation pulses using measured k-space trajectories. *Magnetic Resonance in Medicine* **34,** 446–456 (1995).

47. Papadakis, N. G., Wilkinson, A. A., Carpenter, T. A. & Hall, L. D. A general method for measurement of the time integral of variant magnetic field gradients: Application to 2D spiral imaging. *Magnetic Resonance Imaging* **15,** 567–578 (1997).

48. Vannesjo, S. J. *et al.* Field camera measurements of gradient and shim impulse responses using frequency sweeps. *Magnetic Resonance in Medicine* **72,** 570–583 (2014).

49. Campbell-Washburn, A. E., Xue, H., Lederman, R. J., Faranesh, A. Z. & Hansen, M. S. Real-time distortion correction of spiral and echo planar images using the gradient system impulse response function. *Magnetic Resonance in Medicine* **75,** 2278–2285 (2016).

50. Goora, F. G., Colpitts, B. G. & Balcom, B. J. Arbitrary magnetic field gradient waveform correction using an impulse response based pre-equalization technique. *Journal of Magnetic Resonance* **238,** 70–76 (2014).

51. Janke, A., Zhao, H., Cowin, G. J., Galloway, G. J. & Doddrell, D. M. Use of spherical harmonic deconvolution methods to compensate for nonlinear gradient effects on MRI images. *Magnetic Resonance in Medicine* **52,** 115–122 (2004).

52. Barmet, C., Zanche, N. D. & Pruessmann, K. P. Spatiotemporal magnetic field monitoring for MR. *Magnetic Resonance in Medicine* **60,** 187–197 (2008).

53. Wilm, B. J., Barmet, C., Pavan, M. & Pruessmann, K. P. Higher order reconstruction for MRI in the presence of spatiotemporal field perturbations. *Magnetic Resonance in Medicine* **65,** 1690–1701 (2011).

54. Bhavsar, P. S., Zwart, N. R. & Pipe, J. G. Fast, variable system delay correction for spiral MRI. *Magnetic Resonance in Medicine* **71,** 773–782 (2014).

55. Robison, R. K., Devaraj, A. & Pipe, J. G. Fast, simple gradient delay estimation for spiral MRI. *Magnetic Resonance in Medicine* **63,** 1683–1690 (2010).

56. Brodsky, E. K., Samsonov, A. A. & Block, W. F. Characterizing and correcting gradient errors in non-Cartesian imaging: Are gradient errors Linear Time-Invariant (LTI)? *Magnetic Resonance in Medicine* **62,** 1466–1476 (2009).

57. Onodera, T., Matsui, S., Sekihara, K. & Kohno, H. A method of measuring field-gradient modulation shapes. Application to high-speed NMR spectroscopic imaging. *Journal of Physics E: Scientific Instruments* **20,** 416–419 (1987).

58. Alley, M. T., Glover, G. H. & Pelc, N. J. Gradient characterization using a fourier-transform technique. *Magnetic Resonance in Medicine* **39,** 581–587 (1998).

59. Duyn, J. H., Yang, Y., Frank, J. A. & van der Veen, J. W. Simple Correction Method for k-Space Trajectory Deviations in MRI. *Journal of Magnetic Resonance* **132,** 150–153 (1998).

60. Mason, G. F. *et al.* A method to measure arbitrary k-space trajectories for rapid MR imaging. *Magnetic Resonance in Medicine* **38,** 492–496 (1997).

61. De Zanche, N., Barmet, C., Nordmeyer-Massner, J. a. & Pruessmann, K. P. NMR Probes for measuring magnetic fields and field dynamics in MR systems. *Magnetic Resonance in Medicine* **60,** 176–186 (2008).

62. Vannesjo, S. J. *et al.* Image reconstruction using a gradient impulse response model for trajectory prediction. *Magnetic Resonance in Medicine* **76,** 45–58 (2016).

63. Zeng, H. & Constable, R. T. Image distortion correction in EPI: Comparison of field mapping with point spread function mapping. *Magnetic Resonance in Medicine* **48,** 137–146 (2002).

64. Barmet, C., De Zanche, N., Wilm, B. J. & Pruessmann, K. P. A transmit/receive system for magnetic field monitoring of in vivo MRI. *Magnetic Resonance in Medicine* **62,** 269–276 (2009).

65. Coillot, C. & Leroy, P. Induction Magnetometers Principle, Modeling and Ways of Improvement. *Magnetic Sensors - Principles and applications,* 45–64 (2012).

66. Tumanski, S. Induction coil sensors – a review. *Measurement Science and Technology* **18,** R31–R46 (2007).

67. Senaj, V., Guillot, G. & Darrasse, L. Inductive measurement of magnetic field gradients for magnetic resonance imaging. *Review of Scientific Instruments* **69,** 2400–2405 (1998).

68. Pedersen, J. O., Xue, R., Hanson, C. G. & Hanson, L. G. *Encoding of Inductively Measured k-Space Trajectories in MR Raw Data* in *Proceedings 25th Scientific Meeting, International Society for Magnetic Resonance in Medicine* (2017), 3906.

69. Dietrich, B. E. *et al.* A field camera for MR sequence monitoring and system analysis. *Magnetic Resonance in Medicine* **75,** 1831–1840 (2016).

70. Byrd, D., Tobin, S., Bresch, E. & Narayanan, S. Timing effects of syllable structure and stress on nasals: A real-time MRI examination. *Journal of Phonetics* **37,** 97–110 (2009).

71. Skordilis, Z. I., Toutios, A., Toger, J. & Narayanan, S. Estimation of vocal tract area function from volumetric Magnetic Resonance Imaging. *ICASSP, IEEE International Conference on Acoustics, Speech and Signal Processing - Proceedings,* 924–928 (2017).

72. Pribil, J., Horracek, J. & Horak, P. Two Methods of Mechanical Noise Reduction of Recorded Speech During Phonation in an MRI device. *Measurement Science Review* **11,** 92–98 (2011).

73. Aalto, D. *et al.* Large scale data acquisition of simultaneous MRI and speech. *Applied Acoustics* **83,** 64–75 (2014).

74. Shou, X. *et al.* The suppression of selected acoustic frequencies in MRI. *Applied Acoustics* **71,** 191–200 (2010).

75. MathWorks. *MATLAB* (Signal Processing Toolbox, 2016).

76. Audacity(R). *Audacity(R) software is copyright 1999-2018 Audacity Team. The name Audacity(R) is a registered trademark of Dominic Mazzoni* (2018).

77. Idiyatullin, D., Suddarth, S., Corum, C. A., Adriany, G. & Garwood, M. Continuous SWIFT. *Journal of Magnetic Resonance* **220,** 26–31 (2012).

78. Sohn, S. M., Vaughan, J. T., Lagore, R. L., Garwood, M. & Idiyatullin, D. In vivo MR imaging with simultaneous RF transmission and reception. *Magnetic Resonance in Medicine* **76,** 1932–1938 (2016).

79. Saint-Jalmes, H., Eliat, P.-A., Bezy-Wendling, J., Bordelois, A. & Gambarota, G. ViP MRI: virtual phantom magnetic resonance imaging. *Magnetic Resonance Materials in Physics, Biology and Medicine* **27,** 419–424 (2014).

80. Rondeau-Mouro, C., Kovrlija, R., Gambarota, G. & Saint-Jalmes, H. μ-ViP: Customized virtual phantom for quantitative magnetic resonance micro-imaging at high magnetic field. *Journal of Magnetic Resonance* **275,** 73–79 (2017).

Appendices

A | General Purpose Electronics for Real-Time Processing and Encoding of non-MR Data in MR Acquisitions

The following manuscript has been submitted for publication in *Concepts of Magnetic Resonance: Part B.*

General Purpose Electronics for Real-Time Processing and Encoding of non-MR Data in MR Acquisitions

Jan Ole Pedersen[1,2,3], Christian G. Hanson , Rong Xue[4], and Lars G. Hanson[1,2]

[1] *Center for Magnetic Resonance, Electrical Engineering, Technical University of Denmark, Kgs. Lyngby, Denmark*
[2] *Danish Research Centre for Magnetic Resonance, Centre for Functional and Diagnostic Imaging and Research, Copenhagen University Hospital, Hvidovre, Denmark*
[3] *Sino-Danish Center for Education and Research, Aarhus, Denmark*
[4] *State Key Laboratory of Brain and Cognitive Sciences, Institute of Biophysics, Chinese Academy of Sciences, Beijing, China*

A.1 ABSTRACT

Recording of data other than MR signals are often of interest during MRI. We present unique, versatile circuitry developed for sampling and real-time processing of such non-MR signals to facilitate recording of these by an MR scanner. The circuitry is capable of acquiring multiple signals at 200 kHz sampling rate, measure RF power correlates, perform fast and flexible signal processing, and transmitting both amplitude and frequency modulated RF signals receivable by MR scanners. As an example of use, an electronic point-source signal is generated by the circuitry, and transmitted wirelessly to the receive coil of an MR scanner during an echo-planer imaging sequence.

A.2 INTRODUCTION

Other signals than the magnetic resonance (MR) signal are often of interest during magnetic resonance imaging (MRI). These signals of interest (SOIs) can, e.g., contain biomedical information such as electroencephalography (EEG)[1],[2] or be used for scanner monitoring and characterization. An example of the latter is gradient field measurements, which facilitates determining the exact position of each MR sample in k-space[3],[4],[5]. When acquiring such SOIs, care must be taken to avoid interference with MR measurements, and avoid artefacts caused by scanner subsystems, typically dominated by radio frequency (RF) transmission and gradient switching. Depending on the SOI in question, different strategies have been used. For audio recordings, subtracting a noise-only signal acquired separately have been shown to be a viable strategy[6]. For EEG recording, a typical approach is to minimize artefacts, by, e.g., twisting bipolar electrodes, and filter out remaining artefacts in post-processing[7],[2]. A third approach is to only sample the SOIs in periods where the interfering sources are not active, such as during gradient plateaus, coinciding with MR signal acquisition[8]. While this makes filtering of the SOI to remove artefacts a trivial, or even unnecessary task, it requires high temporal precision and synchronization with the MR scanner, which is non-trivial to obtain.

A relatively simple strategy to obtain the necessary synchronization is acquisition of the SOIs by the MR scanner, which we previously presented hardware developed to facilitate[9],[10]. The SOIs were amplitude modulated at carrier frequencies close to the demodulation frequency of the scanner, and wirelessly transmitted to the MR receive coil. The amplitude modulation, which entailed unattenuated transfer through the scanner's receiver filters, was partially undone by the demodulation performed in the scanner's receive chain, enabling extraction of the SOIs from the raw data of the scan. Non-interfering concurrent SOI and MRI acquisition was possible by exploiting that readout oversampling followed by bandwidth reduction is normally done in MR image reconstruction, allowing for encoding the amplitude modulated SOIs in the discarded frequency range. For traditional Cartesian MRI sampling, the amplitude modulated SOIs thus appeared as stripes orthogonal to the frequency encoding direction outside the requested FOV, if reconstruction was performed without bandwidth reduction. For echo planar imaging (EPI), where the MR signal and modulated SOIs were most easily separated by individual Fourier transformation of each sampled k-space line, the sampling rate of the SOIs effectively became the reciprocal of the echo-spacing, thus typically in the kHz range. This was shown sufficient for concurrent acquisition of biomedical signals, including electrooculography, electrocardiography, and EEG[10]. Since readout oversampling is default for MRI, the method is generally applicable, including for non-Cartesian k-space sampling and parallel imaging.

A subset of SOIs can not be directly sampled as described above. These include SOIs with higher frequency content than the available sampling bandwidth, SOIs having complex dependencies (example below), and/or SOIs, where sampling gaps between scanner readouts are not acceptable. This subset of SOIs can typically still be sampled using an MR scanner, if appropriate signal processing is done before transmission to the scanner. The required pre-processing is dependent on the signal in question, and a catch-all solution is therefore not feasible. One example is electronic phantoms, where the signal from a chosen transversal magnetization density is determined by integrating the Bloch equations and emulated electronically[11]. As the accumulated phase of an MR signal at a given time point is dependent on the magnetic field history, particularly since the most recent excitation pulse, knowledge of both the scanner-generated RF field ($B_1(t)$) and the gradient field must be incorporated into a single SOI to perform such emulation.

To facilitate MR scanner sampling of a broader category of SOIs, we present tailored circuitry capable of sampling up to three signals simultaneously with acquiring a correlate of the RF power transmitted by MR scanners. Real-time flexible processing of the incoming signals is performed by a Field Programmable Gate Array (FPGA), which also controls the phase, frequency and amplitude of a circuitry-generated signal that is receivable by MR scanners.

An overview of the circuitry is shown in Fig. A.1, and a further description and characterization is given in Sec. A.4. While FPGA-based electronics previously have been developed for processing of MR signals, also outside of scanners[12], this is to our knowledge the first hardware developed for transmitting scanner-receivable signals, which offers several advantages. The presented circuitry is 1st generation, and limited optimization has been carried out. Yet it shows considerable potential.

As a putative use case of the circuitry, an MR point-source is emulated electronically from measured $B_1(t)$ and gradient field activity during an MRI sequence. Emulation of such a signal is highly demanding in terms of bandwidth, signal-to-noise ratio and timing, and thus demonstrates the perspectives and limitations of the circuitry well. Even when limited to a point-source, electronic phantoms have multiple potential uses. Examples include motion sensing, sequence optimization, quality assurance, and signal quantification. The electronically generated signal

recorded by the MR scanner is compared to simulations, and the signal obtained from imaging of a physical point-like source.

A.3 THEORY

The frequency $f(\mathbf{r}, t)$ of an MR signal from a point-source positioned at $\mathbf{r}$ is given by

$$f(\mathbf{r}, t) = f_0 + f_G(\mathbf{r}, t) = \gamma B_0 + \gamma B_G(\mathbf{r}, t), \tag{A.1}$$

where γ is the gyromagnetic ratio of the source, B_0 is the size of the scanner's main magnetic field (assumed constant), and $B_G(\mathbf{r}, t)$ is the size of the temporally and spatially varying gradient field. The signal will decay over time due to T_2 relaxation attenuating the size of the transverse magnetization, $M_\perp$:

$$\frac{dM_\perp}{dt} = -\frac{M_\perp}{T_2}. \tag{A.2}$$

An electronic point-phantom may be emulated by transmitting a signal with the same frequency and amplitude variation as the MR signal from a point-source at the target position[13].

A.4 MATERIALS

For fast and flexible signal processing, the presented circuitry features an FPGA (Max 10, Altera. Clock frequency: 40 MHz), which receives data from three 16-bit ADCs for low frequency signal sampling (denoted LF-Rx, sampling rate: 200 kHz, maximum signal peak-peak amplitude (U_{pp}) = 2 V). Before reaching the ADCs, an incoming signal is passed through a programmable-gain amplifier (PGA) with possible amplification between 1× and 200×, and a lowpass antialiasing filter (22 kHz cutoff frequency). The FPGA receives a non-linear power correlate from a fourth ADC, that detect 50–1000 MHz signals in a −25–14 dBm range (RF-Rx).

In our previous work[10], transmission of a SOI to the MR scanner was wireless, which for concurrent MR acquisition was viable, provided the modulated SOIs were detectable and had no spectral overlap with the MRI signal. This restricted the bandwidth available for SOI sampling. By using a wired connection to a single receive channel of a scanner allocated to the purpose, the full channel bandwidth is available for sampling of a SOI with no risk of signal contamination. Depending on the MR scanner and receive coil in question, this may be at the cost of reduced signal-to-noise ratio (SNR) of the MR signal, as the allocated receive channel is not available for MR reception. For the receive coils, where this method has been tested, shunting the output of the preamplifer of the unconnected coil element with the impedance of the receive channel ensured unchanged behavior of the coil element. A wired connection may pose a potential safety risk, as current flow to the scanner or ground is possible. To avoid this, signals from LF-Rx to the FPGA are passed through an optocoupler, providing galvanic isolation.

For transmission of a SOI to the scanner, the FPGA controls the output of a direct digital synthesizer (DDS) subcircuitry, yielding phase, amplitude, and frequency control of an output signal (RF-Tx) of up to 130 MHz frequency and amplitude up to U_{pp} = 100 mV. Two-way communication for hardware control and signal visualization on a computer is possible through a Universal Serial Bus (USB) connection and an 8-bit serial port. The use of the available

bandwidth is fully customizable, as it is controlled by the FPGA. For the work presented here, the USB connection was used for transmission of data packages, containing address, time stamp, and six 16-bit samples at 300 kHz for monitoring measured and FPGA-internal signals. A Joint Test Action Group (JTAG) interface makes flashing of the FPGA possible, and a 2×16 digit LCD display controlled by the FPGA is featured for simple FPGA feedback. The board can either be powered through USB or by a 5 V DC supply, e.g., a non-magnetic rechargeable battery.

A.5 METHODS

To determine the noise properties of the output of the circuitry, a sinusoidal signal ($U_{pp} = 1\,\mathrm{V}$, frequency $f = 1000\,\mathrm{Hz}$) was sampled (LF-Rx, PGA gain: $1\times$) and modulated by example carrier frequencies 63.87 MHz (Larmor frequency of ^{1}H at 1.5 T), 127.74 MHz (^{1}H at 3 T), 32.13 MHz (^{13}C at 3 T) and 74.97 MHz (^{13}C at 7 T).

The feasibility of extracting signals that are amplitude modulated by the circuitry and received by an MR scanner, was also tested. Input waveforms (1 s burst, triangular amplitude, $U_{pp} = 1\,\mathrm{V}, f = 1\,\mathrm{Hz}, 10\,\mathrm{Hz}, 100\,\mathrm{Hz}$ and $1000\,\mathrm{Hz}$) were generated by a waveform generator (Keysight 33500B) and amplitude modulated with the ^{1}H demodulation frequency of a 3 T Philips Achieva MR scanner ($\approx 127\,\mathrm{MHz}$) before being wirelessly transmitted during a pulse-acquire sequence (bandwidth: 8000 Hz, readout time: 2.04 s). The waveforms were transmitted 0.5 s after the start of the scanner readout. The waveforms were extracted from the acquired MR data and compared to the input waveform, simultaneously acquired by an oscilloscope (Agilent Technologies DSOX3024A, voltage resolution: 5 mV).

A rudimentary electronic phantom was generated by measuring the temporal variation of $B_G(\mathbf{r}, t)$ during an EPI sequence, and modulating the frequency of an emulated T_2-decaying signal,

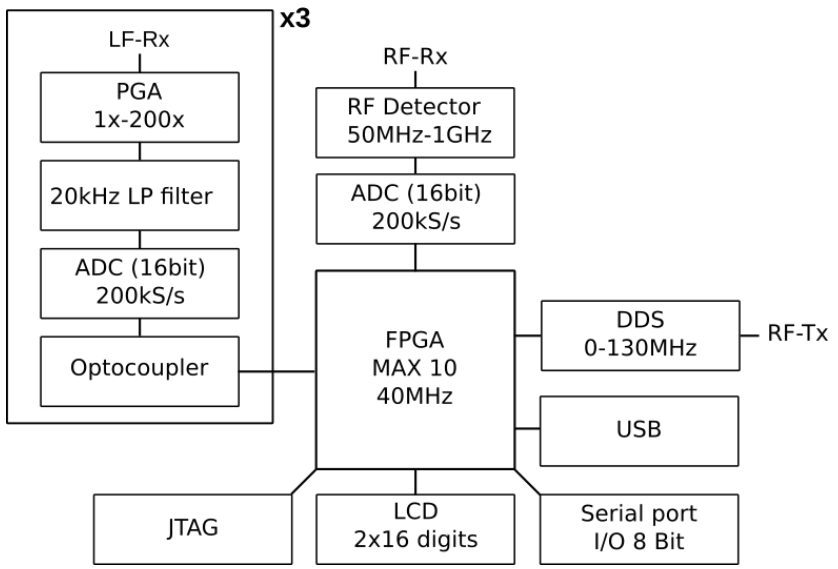

Fig. A.1. Schematics of circuitry developed for acquisition of non-MR data using an MR scanner.

$S_e(t)$, transmitted to an MR scanner correspondingly. For comparison, a point-source signal was also obtained from simulations, $S_s(t)$, and imaging of a point-like physical phantom, $S_p(t)$. The signals $S_s(t)$ and $S_e(t)$ were generated to match the T_2 of the physical phantom, perfect excitation, and steady-state incoherent conditions[14].

The physical phantom (6 cm water filled Ø1.5 mm PVC tubing) was placed at target position $\mathbf{r}$ with its axis perpendicular to the image plane and oriented along $\mathbf{B}_0 = \hat{\mathbf{z}} \cdot B_0$, where $\hat{\mathbf{z}}$ is a unit vector along the z-axis chosen along the scanner bore. A single-slice, single-shot EPI sequence was used (TE/TR: 28 ms/4000 ms, dwell-time: 1.42 µs, echo-spacing: 394 µs, 90° tip angle, voxel size: 4 mm × 4 mm, slice thickness: 4 mm, FOV: 500 mm × 500 mm, 128 averages, Readout direction oversampling factor: 2). The large FOV was chosen to provide large voxels, thus making the physical phantom a good point-source approximation. An EPI sequence was used, as the reconstructed images effectively feature two frequency encoding axes, (readout direction and blip-direction), as reflected in the bandwidth per pixel (bpp), that differs accordingly between the two axis ($\text{bpp}_{\text{RO}} = 3039$ Hz, $\text{bpp}_{\text{blip}} = 20.35$ Hz). For the acquisition of the emulated signal, $S_e^m(t)$, no averaging was performed (50 repeats, individually identified by superscript m). The scanner's data acquisition was delayed to account for a known signal delay through the circuitry (15 µs). As time for T_1 relaxation was not needed for the emulation, TR was here reduced to 100 ms. To determine $B_G(\mathbf{r}, t)$ a gradient pick-up coil (Ø3 cm, 20 windings) was centered at position $\mathbf{r}$, with the normal vector of its circular cross section oriented perpendicular to $\mathbf{B}_0$. This yielded an electromotive force,

$$\epsilon_{\mathbf{r}}(t) = -\frac{d\,\Phi_G}{dt} = \frac{1}{b} \cdot \frac{d\,f_G(\mathbf{r}, t)}{dt}, \tag{A.3}$$

where Φ_G denotes the magnetic flux through the pick-up coil, and b denotes a geometry factor of the pick-up coil. The gradient induced frequency offset was then determined as

$$f_G(\mathbf{r}, t) = \int_0^t b \cdot \epsilon_{\mathbf{r}}(t')\, dt' + c, \tag{A.4}$$

where $t = 0$ denotes the isodelay point[15] of the latest excitation pulse, and c accounts for possible gradients applied at the isodelay point, e.g., a slice selection gradient. The expression holds as long as the gradient field is linearly varying over the cross section of the pick-up coil, which was assumed a valid approximation as the pick-up coil was relatively small and positioned inside the normal imaging volume of the MR scanner. Due to the long TR for imaging of the physical phantom compared to T_1 of water, only the primary FID following excitation was assumed to contribute to the signal. Echo pathways were thus ignored.

The solution to the integral in Eq. A.4 was approximated as a running sum of $b \cdot \epsilon_{\mathbf{r}}(t)$ measured by LF-Rx. To challenge the circuitry, the position $\mathbf{r}$ (approximately 7.5 cm/15 cm offcenter in readout/blip-directions) was chosen so that during the dwell-time of LF-Rx, $\Delta t = 5$ µs, the maximum nominal change of $f_G(\mathbf{R}, t)$ (2.54 kHz) was comparable to the frequency resolution in the readout direction of the EPI sequence. The circuitry was thus expected to correctly position the point-source in the readout-direction, but with limited precision in the higher resolved blip-direction.

The T_2 of the physical phantom was determined using multiple pulse-acquire sequences with varying echo time, and was used in the emulation ($T_2 = 1.4$ s). Since this was considerably longer than the time between signal amplitude updates (for simplicity chosen equal to Δt), the exponential decay of the amplitude of $S_e(t)$ was well approximated by solving Eq. A.2 using the Euler method. To emulate 90° excitation, at $t = 0$, $M_\perp$ was set to a preset value, corresponding to the size of the longitudinal magnetization in equilibrium, thus emulating perfect unsaturated

excitation. The calculated signal was frequency modulated to the demodulation frequency of the MR scanner by the DDS subcircuitry to emulate precession around $\mathbf{B}_0$. The generated MR-like signal was transmitted wirelessly to the receive coil of the scanner through a quarter wavelength antenna connected to RF-Tx. An identical antenna was connected to RF-Rx for monitoring B_1. As all RF pulses in the sequence were excitation pulses with maximum amplitude at the isodelay, $t = 0$ was simply determined by the RF-Rx signal exceeding a threshold. The pick-up coil was observed to also be partially sensitive to B_1, causing gradient waveforms concurrent with B_1 to be noisily determined. This caused incomplete cancellation of the slice selection gradient and the following refocusing gradient, and therefore an offset in the frequency of $S_e(t)$. To avoid this, both gradient waveforms were turned off, thus emulating a perfect slice selection, and resulting in $c = 0$. The PGA was set to $2\times$ amplification, and the constant b was chosen so that the emulated point-source was positioned at $\mathbf{r}$ in a prior calibration scan. The value 1 was subtracted from $\epsilon_{\mathbf{R}}(t)$ in a fraction of the time steps to account for a sub-bit bias of LF-Rx. The frequency of this subtraction was chosen so that measured positive and negative gradients were balanced for the EPI sequence. For both aquisition of $S_e(t)$ and $S_p(t)$, only data acquired from a single receive element of a 32 channel head coil was used in the following analysis.

The signal $S_s(t)$ was obtained by solving the Bloch equations. This simulation was based on gradient waveforms predicted by the MR scanner, which are obtained by convolving the nominal gradient waveforms with a kernel determined by the vendor during calibration of the MR scanner. The kernel accounts for most of the gradient hardware imperfections, such as slew rate limitations, but does not include, e.g., spatial and temperature dependencies[16].

The ability of the circuitry to correctly emulate the temporal phase evolution of a point-source signal was investigated by comparing the phase evolution from individual repetitions of $S_e(t)$ to $S_p(t)$ and $S_s(t)$. Following this, the ability of the circuitry to yield a point-source in a reconstructed image was investigated. The ramp-sampled $S_e(t)$ and $S_p(t)$ were reconstructed by non-uniform Fourier Transformation[17] using a k-space trajectory based on the scanner-predicted gradient waveforms. An effective delayed play-out of the gradient waveforms result in a Nyquist ghost, that was not corrected for, and a stronger ghost than typically observed in EPI images is therefore expected. The reconstructed images were normalised to have equal maximum amplitude. Based on the reconstructed images of $S_e(t)$, the position of the emulated point-source was determined as the highest intensity voxel, and compared to the position of the physical phantom, determined from reconstruction of $S_p(t)$.

A.6 RESULTS

The spectra of the amplitude modulated sinusoids generated by the circuitry are depicted in Fig. A.2 in a -50–50 kHz range around the carrier frequencies. The individual signals were present at three frequencies, consistent with the expected spectrum of an amplitude modulated single frequency signal. A similar noise floor -80 dB below the signal were observed for all four frequency ranges. For 74.97 MHz, additional noise was observed around -25 kHz. The cause of this noise was not investigated further, and the signal power was still significantly higher (30 dB).

The triangular waveforms acquired by an oscilloscope and the MR scanner after amplitude modulation, was found to be almost identical, as seen in Fig. A.3 (top) where both are depicted for one example of the tested waveforms ($f = 10$ Hz). Their difference, Fig. A.3 (mid), was anticorrelated with the test signals, indicating a slight attenuation of the test signals sampled

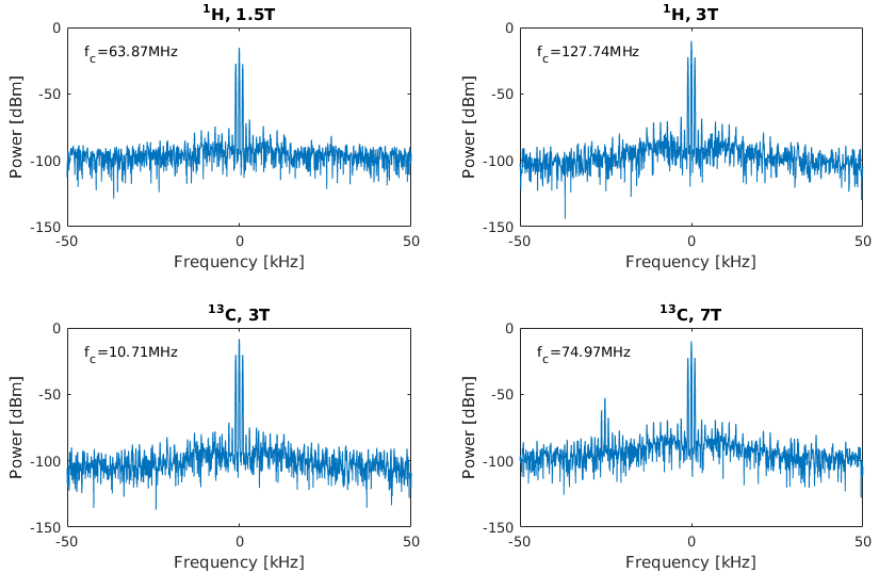

Fig. A.2. Measured output power of amplitude modulated sinusoidal signals ($U_{pp} = 1\,\mathrm{V}, f = 1000\,\mathrm{Hz}$) shown as a function of frequency offset from four example carrier frequencies $f_c = 63.87\,\mathrm{MHz}, 127.74\,\mathrm{MHz}, 10.71\,\mathrm{MHz}$, and $74.97\,\mathrm{MHz}$. Similar power levels were seen at the carrier (-15–$-8\,\mathrm{dBm}$) and sideband frequencies (-20–$-27\,\mathrm{dBm}$). Besides additional noise around $-25\,\mathrm{kHz}$ from $74.97\,\mathrm{MHz}$, a common noise floor ($-95\,\mathrm{dBm}$) is seen for all four frequency intervals.

by the MR scanner. Rescaling the scanner-acquired waveform by a factor 1.012 reduced the difference to a level comparable to the variation seen before transmission of the burst signal (depicted in Fig. A.3 (bottom)). After rescaling, the signal difference had a standard deviation of 3.2 mV, corresponding to 0.64% of the peak amplitude of the waveform generator output. For comparison, an average standard deviation of 2.7 mV, or 0.54% of the peak amplitude, was found across 50 repetitions of the scanner acquisitions. Due to the limited resolution of the oscilloscope, it was not determined, whether the deviation between repetitions was caused by the circuitry or the waveform generator.

The phase evolution during three repeated acquisitions of $S_e(t)$ is depicted in Fig. A.4 (left). The difference in phase, $\Delta\phi$, between $S_e(t)$ and $S_s(t)$ is depicted in Fig. A.4 (top right) for the full duration of the repetitions, and Fig. A.4 (bottom right) for the first 10 readout periods of the same repetitions. Of the 50 repetitions of $S_e(t)$, the three depicted showed the largest negative $\Delta\phi$ ($S_e^{27}(t)$, red), largest positive $\Delta\phi$ (S_e^{29}, green), and smallest final $\Delta\phi$ ($S_e^{17}(t)$, blue) respectively. The repetitions $S_e^{27}(t)$ and $S_e^{29}(t)$ showed similar magnitude of $\Delta\phi$, corresponding to $\epsilon(t)$ being determined with a constant offset of $95\,\mu\mathrm{V}$ and $-95\,\mu\mathrm{V}$ (before PGA amplification), or ± 6.1 times the smallest voltage increment (Δv) of LF-Rx after $2\times$ PGA amplification. For comparison, in periods without gradient waveforms, but with the gradient amplifier turned on and idle, $\epsilon(t)$ was white noise with a standard deviation of $519\,\mu\mathrm{V}$ ($34 \cdot \Delta v$). On the shorter time scale of a single readout period, all three repetitions show almost identical phase evolution. Similar was observed for non-depicted repetitions. The final phase deviation showed a normal

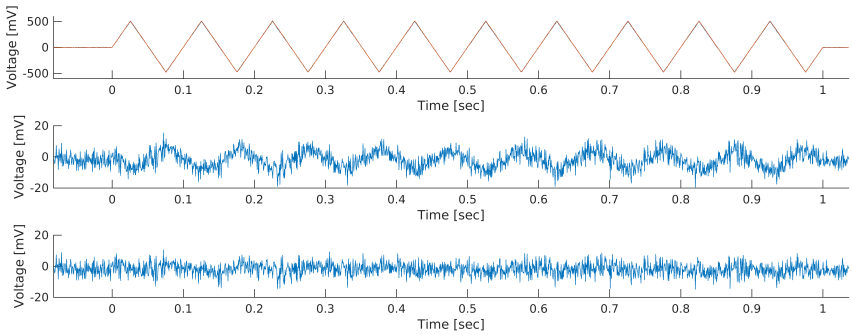

Fig. A.3. Top: A 10 Hz test waveform extracted from measurements performed with a pulse-acquire MR sequence (red curve) and an oscilloscope (blue curve, mostly hidden under red curve), where time $t = 0$ corresponds to start of the test signal play-out. Mid: Difference between the test signals acquired by the scanner and the oscilloscope. The mean absolute difference corresponds to 0.83% of the maximum signal amplitude. Bottom: Difference between rescaled scanner-acquired and oscilloscope-acquired test signal. The mean absolute difference corresponds to 0.57% of the maximum signal amplitude.

distribution corresponding to a standard deviation of 208 rad s^{-1}, or a standard deviation in the measured magnetic field of 781 nT.

The phase evolutions of $S_e^{17}(t)$ and the physical phantom signal, $S_p(t)$, are compared in Fig. A.5, where the phase of $S_s(t)/S_e^{17}(t)$ (blue) and $S_s(t)/S_p(t)$ (black) are depicted. The phase of $S_p(t)$ appeared to have considerable high-frequency content that increased in amplitude over time, and decreased with inclusion of more averages (not shown), which is consistent with this being thermal noise. Similar was not seen in the phase of any repetition of $S_e(t)$, supporting the thermal

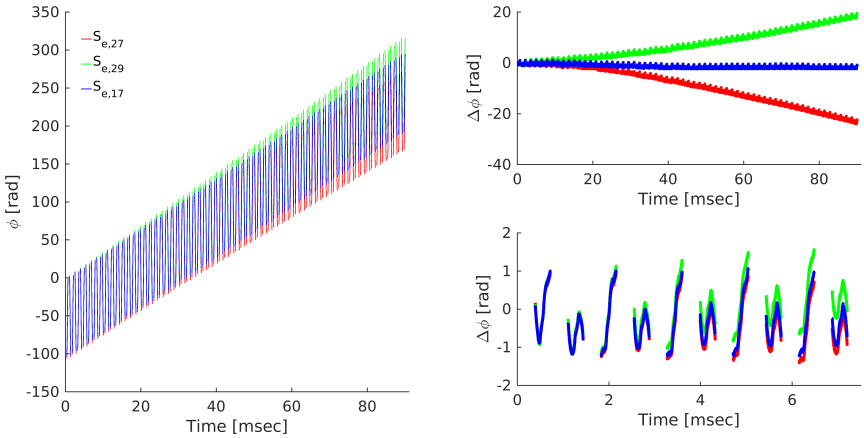

Fig. A.4. Left: Phase evolution of three repetitions of $S_e(t)$. Right: Difference between the phase evolution of the three repetitions of $S_e(t)$ and $S_s(t)$ for the entire repetition (top) and for the first 10 readout periods (bottom).

noise hypothesis. Additionally the signal deviated from that expected from a true point-source, as the phase of $S_p(t)$ showed an unexpected slow oscillation, and the signal strength decayed with a relaxation rate, T_2^*, faster than its determined T_2.

Overall, $S_p(t)$ and $S_e^{17}(t)$ showed a similar phase deviation from $S_s(t)$, indicating a significant difference between the actual and nominal gradients. After correction for possible differences in the initial phase of the signals, the root-mean-square (RMS) error between $S_p(t)$ and $S_s(t)$ was 0.55 rad, whereas between $S_s(t)$ and $S_e^{17}(t)$ this was found to be 0.48 rad. For the worst emulated case, $S_e^{27}(t)$, the RMS error was found to be 46 rad. To estimate the error if $S_e(t)$ is generated from only integrating $\epsilon(t)$ over each readout period instead of over all repetitions, the RMS error was also determined after mean-subtraction of the phase for each individual readout-period of $S_e(t)$ and $S_p(t)$. The RMS error for all $S_e(t)$ was then found to be between 0.16–0.18 rad.

The reconstructed images of $S_p(t)$ (left) and of two repetitions of $S_e(t)$ are depicted in Fig. A.6 with linear and logarithmic amplitude scaling ($S_e^{17}(t)$, center and $S_e^{27}(t)$, right). The position of the point-source was correctly emulated in the readout direction (left-rigt) for all 50 repetitions of $S_e(t)$. In the blip-direction, the deviation in the phase evolution lead to variation of the phantom position between +5 and −3 pixels around the target position (−102–61 Hz). The cumulative nature of the error corresponds to an effective temporal non-linear blip-gradient variation, causing the point-source signal to be smeared over multiple pixels in the blip-direction, particularly visible for $S_e^{27}(t)$.

The reconstructed magnitude images of all repetitions of $S_e(t)$ showed non-Gaussian noise, though only visible on logarithmically scaled images. The relative noise level was lower than what was observed in the reconstructed image of $S_p(t)$. This was evident when Gaussian noise was added to the individual repetitions of $S_e(t)$ to yield the same SNR as the physical point source image, and the Gaussian noise drowned out the structured noise (not shown). A half FOV ghost was also observed for all reconstruction of $S_e(t)$ and $S_p(t)$ with similar relative amplitude (11-13%). This ghost was attributed to the reconstruction being based on the k-space trajectory expected by the scanner, which from Fig. A.5 was concluded to deviate from the actual k-space trajectory. Besides the half FOV ghost, the reconstructed image of $S_p(t)$ showed additional aliases around −80 Hz and 250 Hz, as a result of the slow oscillations visible in the phase evolution of $S_p(t)$ observed in Fig. A.5.

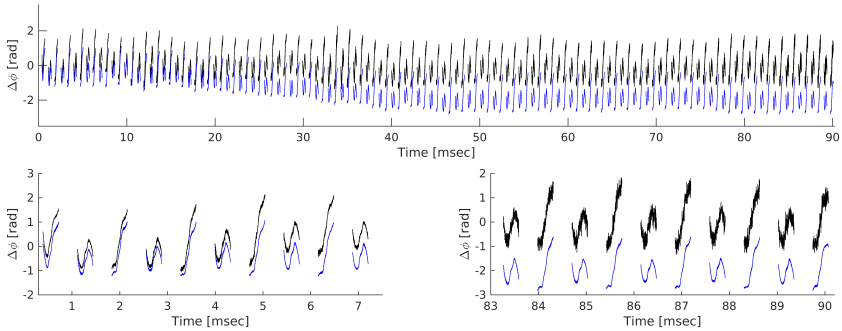

Fig. A.5. Temporal phase evolution of $S_e^{17}(t)$ (blue) and $S_p(t)$ (black) for the entire k-space traversal (top), the first 10 readout periods (bottom left) and the last 10 readout periods (bottom right).

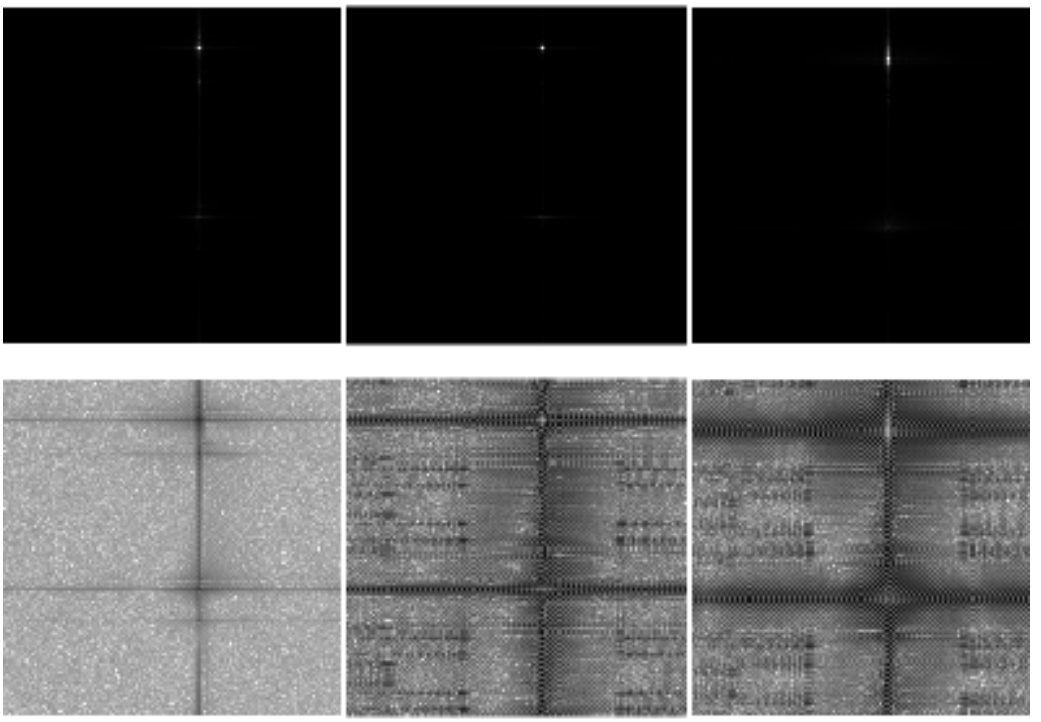

Fig. A.6. Reconstructed images of $S_p(t)$ (left), $S_e^{17}(t)$ (center), and $S_e^{27}(t)$, with linear (top) and logarithmic (bottom) scaling. The frequency encoding direction is left-right.

A.7 DISCUSSION

In this paper we presented unique circuitry developed to facilitate sampling of non-MR signals by an MR scanner. Signals transmitted by the circuitry showed high SNR, and acquisition by an MR scanner introduced only minimal distortions, that were easily accounted for. By combining an inductive gradient field measure and $B_1(t)$ power measurements, the circuitry was shown capable of emulating a point-source.

While the noise characteristics of the circuitry was not determined across all frequencies, a high SNR was found in the tested frequency domains (30 dB or better). The noise may depend on factors that were not controlled, e.g., circuitry position relative to the MR scanner, and the performance may vary. Noise radiated by the circuitry was not a focus, as the SNR was found adequate for all current use cases.

For imaging of the emulated point-source, the slice selection and refocusing gradient waveforms were turned off, as the pick-up coil was found partially sensitive to $B_1(t)$. In cases where concurrent $B_1(t)$ and $B_G(t)$ is essential, the pick-up coil can be enclosed in Faraday shielding that only allow low frequency $B_G(t)$ fields to pass. The large difference in frequency between $B_G(t)$ and $B_1(t)$, makes the design of shielding relatively uncomplicated.

While $S_e(t)$ and $S_s(t)$ were chosen to only have T_2 relaxation appropriate for a true point-source, $S_p(t)$ showed a faster T_2^* signal decay, indicating that the physical phantom deviates from a true point-source, which also is supported by the slow oscillations seen in its phase evolution of $S_p(t)$. A Likely cause of this deviation is field inhomogeneities caused by the sample and its holder.

For fast imaging sequences, the latency introduced by passing a signal through the circuitry (15 µs) amounts to multiple dwell-times. For SOIs where this latency is not negligible, it can be counteracted by delaying the scanner's signal acquisition accordingly, as it was done here for imaging of the emulated point-source. This can pose a challenge for concurrent MR and non-MR acquisition, as the delay should be accounted for in the reconstruction of the MR signal. As the delay is well defined, this is relatively straight forward, either by using the Fourier shift theorem or updating the k-space grid used in the reconstruction.

Inductively determining $B_G(t)$ during a single-shot EPI sequence is challenged by its relatively long readout-time, due to the intrinsic integration that causes noise effects to accumulate over time. A higher precision is expected for sequences with shorter readout-times, as evident from the highly decreased RMS error observed when effectively integrating over shorter time periods. Other methods for determining $B_G(t)$ may also improve the precision. Examples of such are field probes[3],[12],[18] and Hall effect sensors[19] which previously have been used in MRI, and yield a direct measure of the magnetic field, so integration is avoided. For showcasing the use of the presented circuitry, the precision obtained from inductive measures was, however, found adequate, and compared to other methods, inductive coils has the clear advantages of being easy to manufacture and use.

Electronic point-phantoms are potentially applicable for quantitative MRI, where an electronic phantom can serve as reference signals for determining absolute concentrations[11]. Another possible application is for motion tracking, by attaching one or multiple pick-up coils to a subject, and emulating individual point-sources[20]. This could facilitate robust image registration, particularly relevant for low SNR images, e.g., diffusion weighted imaging, and low gamma MRI, e.g., ^{13}C and ^{23}Na, where this is a well-known challenge.

Besides emulating electronic phantoms, the presented circuitry also enables sampling of other SOIs. Since the position in k-space is proportional to the temporal integral of $f_G(t)$, the k-space trajectory can be determined with limited changes to the current experimental setup. While similar measures likely can be achieved with higher sensitivity using, e.g., field probes, inductive measures are independent of signal relaxation, which simplifies their use significantly, and can be used independently of field inhomogeneity and of the nuclei targeted by the sequence. The applied gradient can be measured locally using, e.g., a gradiometer or be globally estimated from the measured signal under a spatial linearity assumption and exploiting that the field is constant in the iso-center.

The RF power correlate measured by the circuitry (RF-Rx) does not yield phase information when measuring $B_1(t)$, which is a limitation, especially for multi-shot sequences. Demodulating the acquired $B_1(t)$ signal with the reference frequency of the MR scanner would allow sampling by LF-Rx, yielding both phase and amplitude measures. In order for the demodulated signal to have correct phase, clock synchronization between the MR scanner and the clock driving the deconvolution is necessary. It is possible that trigger pulses generated by the MR scanner can facilitate such clock synchronization, though the temporal precision might be confounding. Alternatively, the same crystal may be used for demodulation and modulation to ensure phase synchronization. With knowledge of the phase of $B_1(t)$ the signal from specific coherence pathways can be emulated for example, which is not directly feasible by imaging of a physical phantom.

In conclusion, the presented versatile circuitry and an MR scanner was used for sampling of non-MR signals, which provided a simple approach for acquiring signals of interest in synchrony with MR data acquisition. The circuitry was proven capable of performing real-time signal processing of multiple inputs to a generate and transmit a single signal receivable by an MR scanner. Based on $B_1(t)$ power correlate measures and inductive $B_G(t)$ measures, a point-source signal was generated electronically during an EPI sequence and sampled by the scanner. The circuitry offers great flexibility, and facilitates sampling of most signals of interest during MR acquisition, and is a useful and inexpensive tool for, e.g., scanner monitoring and methods development.

Bibliography

1. Huster, R. J., Debener, S., Eichele, T. & Herrmann, C. S. Methods for Simultaneous EEG-fMRI: An Introductory Review. *Journal of Neuroscience* **32,** 6053–6060 (2012).
2. Gotman, J., Kobayashi, E., Bagshaw, A. P., Bénar, C. G. & Dubeau, F. Combining EEG and fMRI: A multimodal tool for epilepsy research. *Journal of Magnetic Resonance Imaging* **23,** 906–920 (2006).
3. Kasper, L. *et al.* Monitoring, analysis, and correction of magnetic field fluctuations in echo planar imaging time series. *Magnetic Resonance in Medicine* **74,** 396–409 (2015).
4. Duyn, J. H., Yang, Y., Frank, J. A. & van der Veen, J. W. Simple Correction Method for k-Space Trajectory Deviations in MRI. *Journal of Magnetic Resonance* **132,** 150–153 (1998).
5. Mason, G. F. *et al.* A method to measure arbitrary k-space trajectories for rapid MR imaging. *Magnetic Resonance in Medicine* **38,** 492–496 (1997).
6. Bresch, E., Nielsen, J., Nayak, K. & Narayanan, S. Synchronized and noise-robust audio recordings during realtime magnetic resonance imaging scans. *The Journal of the Acoustical Society of America* **120,** 1791–1794 (2006).
7. Goldman, R. I., Stern, J. M., Engel, J. & Cohen, M. S. Acquiring simultaneous EEG and functional MRI. *Clinical Neurophysiology* **111,** 1974–1980 (2000).
8. Anami, K. *et al.* Stepping stone sampling for retrieving artifact-free electroencephalogram during functional magnetic resonance imaging. *NeuroImage* **19,** 281–295 (2003).
9. Hanson, L. & Hanson, C. *A multi-frequency amplitude modulator for encoding electrical signals in MR images* in *Proceedings 14th Scientific Meeting, International Society for Magnetic Resonance in Medicine* (2006), 2388.
10. Hanson, L. G., Lund, T. E. & Hanson, C. G. Encoding of electrophysiology and other signals in MR images. *Journal of Magnetic Resonance Imaging* **25,** 1059–1066 (2007).
11. Salvati, R., Hitti, E., Bellanger, J. J., Saint-Jalmes, H. & Gambarota, G. Fat ViP MRI: Virtual Phantom Magnetic Resonance Imaging of water-fat systems. *Magnetic Resonance Imaging* **34,** 617–623 (2016).
12. Dietrich, B. E. *et al.* A field camera for MR sequence monitoring and system analysis. *Magnetic Resonance in Medicine* **75,** 1831–1840 (2016).
13. Saint-Jalmes, H., Eliat, P.-A., Bezy-Wendling, J., Bordelois, A. & Gambarota, G. ViP MRI: virtual phantom magnetic resonance imaging. *Magnetic Resonance Materials in Physics, Biology and Medicine* **27,** 419–424 (2014).
14. Haacke, E. M., Brown, R. W., Thompson, M. R. & Venkatesan, R. *Magnetic Resonance Imaging: Physical Principles and Sequence Design* (Wiley, 1999).

15. Bernstein, M. A., King, K. F. & Zhou, X. J. *Handbook of MRI Pulse Sequences* (2004).

16. Zur, Y. & Stokar, S. An algorithm for eddy currents symmetrization and compensation. *Magnetic Resonance in Medicine* **35,** 252–260 (1996).

17. Greengard, L. & Lee, J.-Y. Accelerating the Nonuniform Fast Fourier Transform. *SIAM Review* **46,** 443–454 (2004).

18. Vannesjo, S. J. *et al.* Gradient system characterization by impulse response measurements with a dynamic field camera. *Magnetic Resonance in Medicine* **69,** 583–593 (2013).

19. Schell, J. *et al.* Towards a Hall effect magnetic tracking device for MRI. *35th Annual International Conference of the IEEE EMBS,* 2964–2967 (2013).

20. Ooi, M. B., Krueger, S., Thomas, W. J., Swaminathan, S. V. & Brown, T. R. Prospective real-time correction for arbitrary head motion using active markers. *Magnetic Resonance in Medicine* **62,** 943–954 (2009).

B | Encoding of regularized inductively measured k-space trajectories in MR raw data

The following manuscript is in preparation, and extends on experiments and results in an abstract presented at *The ISMRM 25th Annual Meeting & Exhibition, 2017*[68].

Noname manuscript No.
(will be inserted by the editor)

Encoding of inductively measured k-space trajectories in MR raw data

Jan Ole Pedersen[1,2,3] · Christian G. Hanson · Rong Xue[4] · Lars G. Hanson[1,2]

the date of receipt and acceptance should be inserted later

1 Abstract

Objectives Concurrently acquire an inductively generated k-space trajectory measure and magnetic resonance imaging data by an MR scanner.
Materials and methods An inductive gradient measure was regularized using measured gradient coil currents and recorded by the scanner concurrently with raw MR data. The gradient measure was frequency modulated into an RF signal receivable by the scanner, yielding a k-space trajectory measure from the cumulative phase of the acquired data. Generation of the gradient measure and frequency modulation was performed by previously developed custom circuitry.
Results For a normal echo planar imaging (EPI) sequence, the acquired k-space trajectory measure yielded slightly improved image quality compared to that obtained from using the scanner's estimated eddy current compensated k-space trajectory. For a spiral trajectory, the regularized inductive k-space trajectory measure lead to a a 76% decrease in the root-mean-square error of the reconstructed image.
Discussion While the the proof-of-concept experiments show potential for further improvement, the feasibility of inductively measuring k-space trajectories and increasing the precision through regularization was demonstrated. The approach offers an inexpensive approach to acquire k-space trajectories concurrently with scanning.

[1] Center for Magnetic Resonance, Electrical Engineering, Technical University of Denmark, Kgs. Lyngby, Denmark
[2] Danish Research Centre for Magnetic Resonance, Centre for Functional and Diagnostic Imaging and Research, Copenhagen University Hospital, Hvidovre, Denmark
[3] Sino-Danish Center for Education and Research, Aarhus, Denmark,
[4] State Key Laboratory of Brain and Cognitive Sciences, Institute of Biophysics, Chinese Academy of Sciences, Beijing, China,

2 Introduction

Real-time acquisition and processing of non-MR signals in the MR environment is of general interest. A particular example is monitoring of gradient-switching during MR image acquisition, and thereby of actual k-space trajectories, which may differ significantly from nominal trajectories [4; 14; 17]. The deviations are caused by gradient imperfections, that are normally addressed by the use of robust k-space trajectories where hardware limitations and instabilities cause limited, or easily accounted for, artefacts in the reconstructed images. One example is echo planar imaging (EPI), where Nyquist ghosting, caused by deviation from the nominal k-space trajectory in the readout-direction, typically is addressed by acquiring extra reference lines to determine and facilitate correction of an effective delay in the play-out of the gradient waveforms [8].

Other k-space trajectories are more challenging, e.g., spiral or rosette trajectories, as the effect of gradient imperfections are not as easily accounted for. For such sequences nominal k-space trajectories are typically not sufficient, and k-space trajectory errors must either be alleviated or corrected for in reconstruction using more elaborate techniques [13]. One approach is to assume time invariant behaviour of the gradient system, which allows for determining the k-space trajectory from calibration scans [15; 18; 20] or convolving nominal trajectories with predetermined impulse-response functions to improve the estimate of the actual gradient waveforms [3; 10; 25]. Particularly, the method of Duyn et al [15] is widely applied as it yields reliable k-space traject-

ory measures in reasonable time, while only requiring the use of a homogeneous phantom. The assumption of time invariance is challenged by temporal changes in the gradient system induced by, e.g., heating of the gradient coils due to ohmic losses during gradient-intensive sequences. Hardware temperatures and associated imperfections typically change over seconds to minutes, whereas other characteristics may change on a longer time scale, e.g., when the system is recalibrated or serviced. Additionally, unavoidable minor shot-to-shot variability happen on an even shorter time scale, due to hardware instabilities [17]. NMR-based field probes offer attractive ways to determine magnetic fields dynamically, and therefore also k-space trajectories concurrently with imaging [4; 9; 17; 26], avoiding the assumption of time invariance. While offering excellent sensitivity, they require extensive dedicated hardware specific to scanners and field strengh. They may interfere with imaging [5], even when based on other nuclei than the one being imaged, and as they are highly sensitive to magnetic field inhomogeneities they must be placed inside or close to the field of view (FOV), limiting the flexibility in their positioning.

The time varying property of the gradient field allows for alternative direct monitoring of the gradient performance. While field probes offer better sensitivity, inductive measurements do not rely on the acquisition of an FID, thus offering more robustness against field inhomogeneities and independence of spin history. The inductive signal is proportional to the time-derivative of the magnetic field, and obtaining a measure for the gradient field therefore requires temporal integration. In the work of Senaj et al [23], this integration was performed in analogue circuitry, which in addition featured a relay for discharging of the integrator at the start of each measurements. The integration can alternatively be performed digitally, potentially simplifying the necessary hardware and yield increased flexibility in signal processing capabilities [11; 19].

Determining k-space trajectories from gradient measures concurrently with scanning requires real-time signal processing and sub-µs synchronization with the MR signal acquisition. Particularly the synchronization is non-trivial to obtain, but can be achieved directly if the the scanner itself is used for acquisition of both signals, which we recently developed hardware to facilitate [1; 21]. The circuitry features a field-programmable gate array (FPGA) for fast and reprogrammable signal processing, and acquisition of up to 4 input signals with one input being designated for acquisition of RF correlates to determine the envelope of scanner-applied RF pulses. The FPGA controls the frequency and amplitude of a direct digital synthesis sub-circuitry (DDS), that can generate signals receivable by typical MR scanners.

In this paper, gradient-induced magnetic field changes of an MR scanner are measured inductively, and used for generating k-space trajectory measures through digital integration and real-time processing by the previously developed custom circuitry. Performing frequency modulation of a carrier signal with the gradient measure encodes a k-space trajectory measure into the cumulative phase of the signal. If the frequency of the carrier signal is in the range of Larmor frequencies of the imaged sample, it can be transmitted to the receive chain of the scanner without being attenuated by its filters. The demodulation performed in the receive chain undoes the frequency modulation, enabling extraction of a k-space trajectory measure from raw data acquired concurrently with MR data. The inherent integrations needed for determining k-space trajectories inductively cause noise to accumulate rapidly over time, which decreases the obtainable precision. We show that the noise accumulation can be counteracted by regularization using simple measurements of the current running to the gradient coils. The k-space trajectory caused by the readout gradient of an EPI sequence, and the k-space trajectory of a spiral sequence are measured, and used in reconstruction of MR data from a structured water phantom. The reproducibility, accuracy and ability to reconstruct artefact-free images are evaluated for the prototype implementation to assess the general applicability of the method for reliably determining k-space trajectories concurrently with MR acquisition.

3 Theory

The position, $k_r(t)$, in k-space at time t due to one of three orthogonal spatial components $r \in \{x, y, z\}$ of the time-dependent, spatially linear gradient field $G_r(t)$ is given as

$$k_r(t) = \frac{\gamma}{2\pi} \int_0^t G_r(\tau)\, d\tau, \tag{1}$$

where $t = 0$ is the isodelay point [6] of the excitation pulse, γ the gyromagnetic ratio ($2\pi \cdot 42\,\mathrm{MHz\,T^{-1}}$ for protons) and subscript r denotes the given spatial component. The k-space trajectory can then be determined from the accumulated phase, $\phi(t) = \int_0^t \omega(\tau)\, d\tau$, of a signal originating at position $\mathbf{r}$, with frequency $\omega(t) = D_r \gamma G_r(t)$ with D_r being the component of $\mathbf{r}$ along the gradient direction. According to Faraday's law, a voltage $v(t)$ is induced over a circular pick-up coil with its center positioned at $\mathbf{r}$ due to a temporally

varying magnetic flux, $\Phi(t)$, through the coil:

$$v_r(t) = -\frac{d\,\Phi(t)}{dt} = \frac{d\,G_r(t)}{dt}\frac{1}{b}. \quad (2)$$

The constant b is dependent on the geometry of the pick-up coil and its position in the gradient coil of the MR scanner generating a magnetic field, $\mathbf{B} = B \cdot \hat{\mathbf{z}}$, with $\hat{\mathbf{z}}$ chosen along the main field direction, typically parallel to the bore. Under the assumption that $G_r(t)$ is slowly varying compared to the dwell-time (Δt) between discrete samples of $v_r(t)$, it can be well approximated by numerical integration:

$$b\,v_r(t)\,\Delta t \approx G_r(t) - G_r(t - \Delta t), \quad (3)$$

$$G_r^v(t) = \sum_{i=1}^{N} [b\,v_r(t_1 + i\,\Delta t)\Delta t] + c = G_r(t) + \epsilon(t). \quad (4)$$

Here $N = \frac{t-t_1}{\Delta t}$, with t_1 being the starting time of integration. The constant c accounts for any gradient applied at t_1, and $\epsilon(t)$ accounts for any deviation between the gradient estimate, $G_r^v(t)$, and the actual gradient waveform, $G_r(t)$. Due to the integration (here summation) involved in determining $G_r^v(t)$, the error $\epsilon(t)$ is expected to increase in amplitude over time, limiting the obtainable sensitivity. This can be counteracted by regularization based on additional knowledge of $G_r(t)$. One possibility is to calculate a gradient estimate, $G_r^I(t)$, from its driving current, $I_r(t)$ [24]. This is an approximate gradient field measure insensitive to, e.g., eddy currents, and an inaccurate predictor on a short time scale. However, on a longer time scale it is highly reproducible and accurate, and therefore potentially well suited for regularization of the inductive magnetic field measure. A simple, regularized inductive measure, $G_r^M(t)$, can be calculated as

$$G_r^M(t) = \sum_{i=1}^{N} [b\,v_r(\tau_i)\Delta t - \lambda R(i)] + c, \quad (5)$$

where $\tau_i = t_1 + i\,\Delta t$ and $\lambda \in [0; 1]$ determines the influence of the regularization term

$$R(i) = \zeta \cdot \left[G_r^M(\tau_{i-1}) - G_r^I(\tau_{i-1})\right]^2 \quad (6)$$

If $G_r^M(\tau_{i-1}) < G_r^I(\tau_{i-1})$, then $\zeta = -1$ for the given sample of $R(i)$, else, $\zeta = 1$. The term $R(i)$ will drive the regularized induction gradient measure, $G_r^M(t)$, towards the current-based estimate, $G_r^I(t)$, at a rate dependent on λ. Assuming that the amplitude of $\epsilon(t)$ is slowly increasing compared to the rate of change of $G_r(t)$, for an appropriate chosen value of λ, $G_r^M(t)$ retain the accuracy from an inductive and direct measure of $G_r(t)$ on a short time scale, while having reproducibility similar to $G_r^I(t)$ on a longer time scale.

4 Materials and methods

Multiple k-space trajectory measures were determined and compared. These are introduced in the following section and summarized in Table 1.

To determine $v_r(t)$, a simple pick-up coil (20 windings, Ø3 cm) was placed in the gradient field of the MR scanner (7/15 cm in $\hat{\mathbf{x}}/\hat{\mathbf{y}}$-direction from isocenter, with the $\hat{\mathbf{y}}$-direction being anterior-posterior). A current clamp was used to determine $I_r(t)$ (Fluke i400s, current range: 5 A to 400 A). Both were connected to the above-mentioned previously developed circuitry facilitating sampling of non-MR signals by MR scanners. This was achieved through real-time FPGA signal processing and modulation by a carrier signal recordable by the scanner. The circuitry determined $G_r^v(t)$, $G_r^I(t)$, and $G_r^M(t)$ from discrete sampling of $v_r(t)$ and $I_r(t)$ (16-bit samples acquired at 200 kHz sampling rate, 22 kHz cutoff frequency anti-aliasing filter). A sub-bit bias of the ADCs of the circuitry introduced errors in the measures of $v_r(t)$ and $I_r(t)$, which were accounted for by nulling of the least significant bit in the discretized $v_r(t)$ and $I_r(t)$ in a fraction of the time steps. The frequency of nulling was chosen, so that the period between k-space zero crossings matched those of the nominal trajectory on average. A carrier signal with frequency chosen equal to the scanner's reference frequency, ω_0, was frequency modulated by the individual measures of $G_r(t)$ to yield $\omega'(t)$. This signal was transmitted by wire to a single receive channel of the scanner. The demodulation performed by the scanner partially undid the frequency modulation, and resulted in $\omega(t)$ being sampled. This allowed for extraction of the individual measures of $k_r(t)$ from unwrapping of the cumulative phase of the scanner-acquired signal. The average of samples acquired during the first 50 µs of each k-space trajectory acquisition was subtracted to account for a discrepancy in the initial phase between repetitions after unwrapping of the cumulative phase.

Using a 3 T Philips Achieva scanner, the k-space trajectory due to gradients in only the readout-direction, $k_m(t)$, of a vendor EPI sequence was determined (TE: 35 ms, TR: 4000 ms, single slice, 2 mm thickness, FOV: 230×230 mm, 96×95 acquisition matrix with $2\times$ oversampling in the readout-direction yielding an actual acquisition matrix of 192×95, dwell-time/echo-spacing: 4.6/493 µs, 50 repetitions, 90° excitation pulses). As summarized in Table 1, the trajectory was determined using $G_m^v(t)$ exclusively, yielding $k_m^v(t)$, using $G_m^I(t)$ exclusively ($k_m^I(t)$), using $G_m^M(t)$ ($k_m^M(t)$), and using Duyn's method ($k_m^D(t)$). The readout gradient was applied in the $\hat{\mathbf{x}}$-direction, corresponding to left-right in the scanner so $G_m(t) = G_x(t)$. A correlate of the amp-

Table 1 Summary of acquired and compared k-space trajectory measures. When appropriate, an additional subscript $\{s, m, x, y\}$ denotes the played out k-space trajectory component, where m denotes EPI readout, and x, y the two components of a spiral trajectory combined denoted s.

k-space trajectory	Obtained from...
$\tilde{k}(t)$	... scanner logfile.
$\tilde{k}^E(t)$	... $\tilde{k}(t)$ by correcting for an effective delay due to eddy currents.
$k^V(t)$	... inductively measuring the gradient field.
$k^I(t)$	... a measure of the current delivered to the gradient coil.
$k^M(t)$	... regularizing an inductive measure by a current measure.
$k^D(t)$	... Duyn's method, relying on 1D imaging after localized excitation.

litude of RF pulses applied by the scanner was measured wirelessly by the applied circuitry, and the approximate isodelay points of the excitation pulses were determined by this signal exceeding a threshold. A temporal gap between each excitation pulse and the start of $G_m(t)$ allowed for setting the current measure of $G_m(t) = 0$ following each detection of an excitation pulse. This lead to t_1 being a time point without gradient activity, so $c = 0$. The long TR of 4000 ms was chosen to ensure minimal signal loss from incomplete signal relaxation, and to avoid heating effects of the gradient coils to ensure minimal variance over time, as needed for acquiring trajectories using Duyn's method as reference. To assess the circuitry performance, a signal with frequency ω_0 was acquired in a separate scan ($k_0(t)$), corresponding to determining $k(t)$ for $G(t) = 0$.

The regularized inductively determined $k_m^M(t)$ was interpolated to delayed time points to account for a delay (15.1 µs) arising from passing signals through the circuitry, and from performing signal processing. The acquired $k_m^I(t)$ was re-sampled to account for an observed pre-emphasis compared to $k_m^D(t)$, and a delay originating from generating $G_r^I(t)$ (11.0 µs). A discrepancy between the modulation frequency of the circuitry and the demodulation frequency of the scanner was accounted for by subtracting a linear fit to the unwrapped phase of individual repetitions of the scans. The k-space trajectory estimated by the scanner, $\tilde{k}_m(t)$, was obtained from logging done by the scanner. This trajectory was re-sampled to delayed time points, yielding $\tilde{k}_m^E(t)$, to account for an observed effective delay compared to $k_m^D(t)$ (1.4 µs). This is similar to simple eddy current compensation.

EPI of a structured water phantom was performed with both readout and phase-encoding gradients. Imperfections in the blipped phase-encoding gradients were not limiting for the EPI performance, and were ignored in the present context. The acquired data were therefore reconstructed using the individual measures of $k_m(t)$ and nominal phase-encoding gradients ($G_p(t) = G_y(t)$), to yield 2D images.

In addition to the EPI sequence, the k-space trajectory of a single-shot spiral-out sequence was also determined (TE: 10 ms, TR: 4000 ms, single slice, 2 mm thickness, FOV: 230 × 230 mm, 9099 samples, dwelltime: 4.4 µs, 50 repetitions, 90° excitation pulses). The trajectory, $k_s(t)$ was obtained from separate acquisitions of $k_x(t)$ and $k_y(t)$ using the regularized integrative measure ($k_s^M(t)$), and Duyn's method ($k_s^D(t)$). Also the scanner's assumed trajectory ($\tilde{k}_s(t)$) was obtained, and re-sampled to delayed time points using the delay determined for the EPI sequence ($\tilde{k}_s^E(t)$). The four k-space trajectories were used for image reconstruction of MR data acquired from the same structured phantom used in the EPI experiments.

For all reconstructions, images from 31 individual elements of a head coil were reconstructed separately using non-uniform Fourier transformations [16], and sampling density compensation [22]. Images from individual coil elements were combined using Sum-of-Squares. In all EPI reconstructions, 7 of 192 samples in the end of each readout were discarded, as $k_m^M(t)$ was not determined for these due to the delay described above. For spiral sequences the last 4 of 9099 samples were discarded. In generating both $k_m^M(t)$ and $k_s^M(t)$ $\lambda = 0.25$, chosen based on observations made in initial experiments.

5 Results

The standard deviation across 50 repetitions of acquiring $k_m(t)$ using each of the described approaches and 50 repetitions of acquiring $k_0(t)$ are depicted in Figure 1. From the limited relative standard deviation of $k_m^D(t)$ (on average $9.94 \cdot 10^{-7}$), the time invariance assumption of the system was found valid for the chosen sequence parameters, speaking against this as being contributing significantly to the standard deviation observed for the

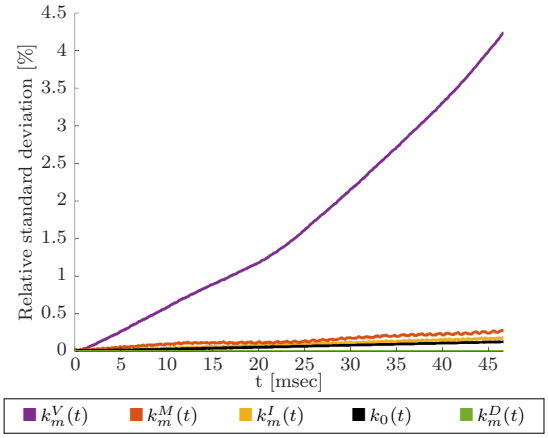

Figure 1 Standard deviation in the central k-space position across 50 repeated acquisitions of the individual measures of $k_m(t)$ and $k_0(t)$ relative to the full width of the acquired k-space trajectory.

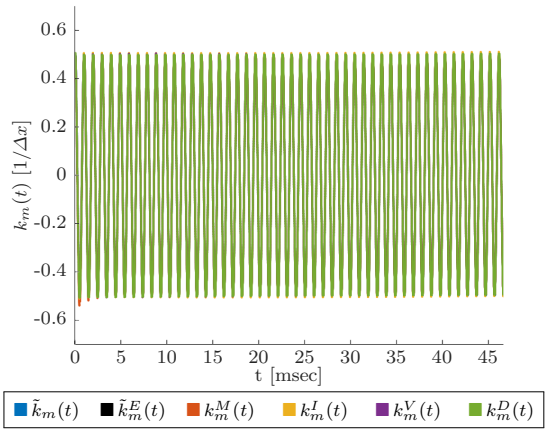

Figure 2 Averaged measures of $k_m(t)$ in units of $1/\Delta x$, where Δx is the voxel size in the reconstructed image in the $\hat{\mathbf{x}}$-direction. The individual measures are almost non-distinguishable from $k_m^D(t)$.

remaining measures of $k_m(t)$. Due to this $k_m^D(t)$ and $k_s^D(t)$ were assumed closest to the actual $k_m(t)$ and $k_s(t)$, and were therefore used as reference in the following comparisons. The relative standard deviation of the central measurement of $k_m(t)$ was used in comparison of the individual k-space trajectory measures, and are summarized in Table 2 together with the following findings.

As expected, the relative standard deviation of the non-regularized $k_m^v(t)$ was found to increase considerably faster than for the other measures of $k_m(t)$, and with a non-linear temporal dependency, likely due to the accumulated quantization errors amplified by the integrations inherent in determining $k_m^v(t)$. In comparison $k_m^I(t)$ and $k_m^M(t)$ were quantitatively more reproducible, and an approximately linear temporal dependency was observed for their relative standard deviations. Notably, the relative standard deviation of $k_0(t)$ was comparable to that of $k_m^M(t)$ and $k_m^I(t)$ (46% and 67%, respectively).

In Figure 2 and Figure 3, the time evolution of the average measures of $k_m(t)$ and their deviation from $k_m^D(t)$ (k-space trajectory error) are depicted. In Figure 3 the top graph depicts the k-space trajectory errors for the entire EPI readout, and the bottom graph depicts the 3 central readout periods. All compared k-space trajectory errors reached a steady state with oscillations showing periodicity similar to twice the echo-spacing, though with considerable smaller amplitude for $k_m^M(t)$ and $k_m^v(t)$. For acquisition of $k_m^D(t)$, the slice selection gradient was applied by the same gradient coil as the investigated gradient waveform. This caused long-lived eddy currents, that would not be present during imaging, as the slice selection gradient here is orthogonal to the imaging plane. For $k_m^D(t)$, these eddy currents are accounted for, but this was not possible for the other k-space measures, if acquired concurrently with $k_m^D(t)$. As this was the case for $k_m^v(t)$, it experienced approximately 30 Hz oscillations, that diminished over the first 25 ms. These oscillations were not observed for $k_m^M(t)$, that was acquired with the slice encoding gradient in the $\hat{\mathbf{z}}$-direction. Disregarding the 30 Hz oscillations, the averaged $k_m^v(t)$ showed similar performance to $k_m^M(t)$, but with higher variance between repetitions (not shown), as can also be deduced from Figure 1.

The k-space trajectory error of $\tilde{k}_m(t)$ was reduced by 40.2% from 0.378% to 0.226% on average by performing delay correction to yield $\tilde{k}_m^E(t)$. The average k-space trajectory error of $k_m^M(t)$ was 0.173%. As evident from Figure 3 (top), the first readout periods of $k_m^M(t)$ contributed significantly to this error, and disregarding the first six readouts reduced it to 0.076%, (in comparison, the error of $\tilde{k}_m^E(t)$ was 0.213% for the same period). The cause of this initial inaccuracy was ascribed to the error also visible for $k_m^I(t)$ in Figure 3, though for $k_m^I(t)$ the error was only observable for the first two readouts, indicating, that the regularization prolonged the time needed to reach steady state.

Using the averaged measures of $k_m(t)$, 2D images were reconstructed, and scaled so that the reconstruction using $\tilde{k}_m(t)$ had an average root-mean-square deviation from the image reconstructed using $k_m^D(t)$ (image RMS error) of 1. Trajectories performing better than

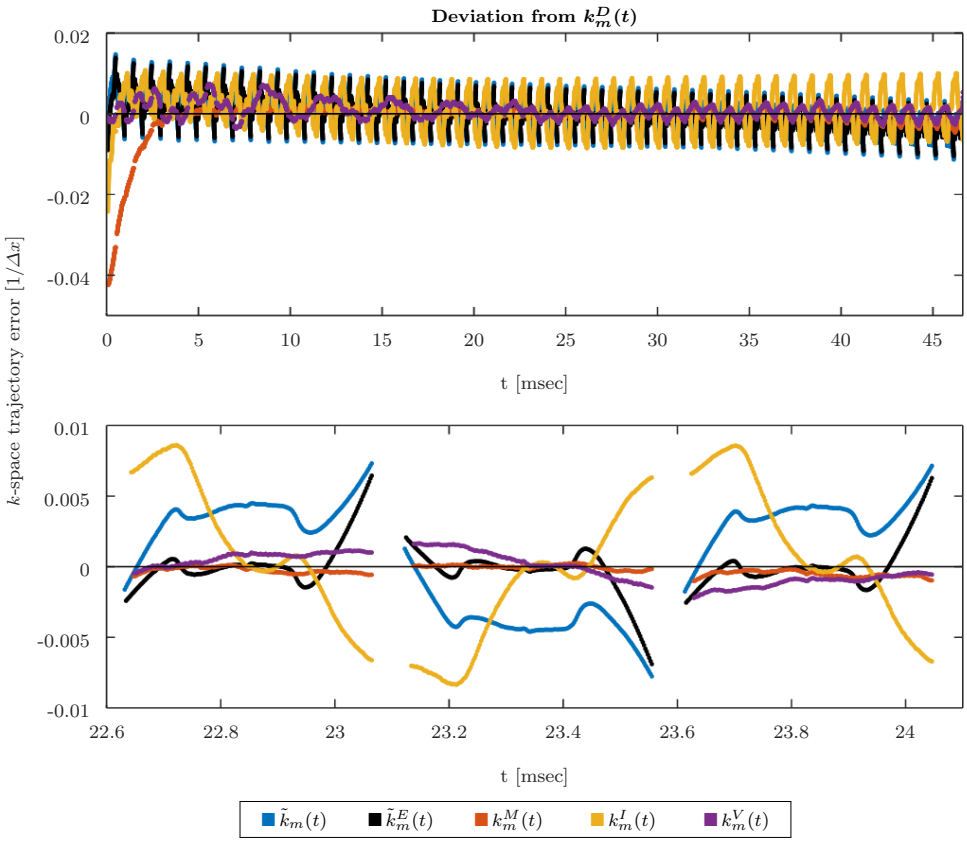

Figure 3 Difference of acquired measures of $k_m(t)$ relative to $k_m^D(t)$ (k-space trajectory error) for the entire EPI readout (top), and the centre three readouts (bottom).

the scanner's assumed trajectory (before eddy current compensation) will thereby have an RMS error below 1. The spatial distributions of the image RMS error are depicted in Figure 4 for $\tilde{k}_m(t)$, $\tilde{k}_m^E(t)$, $k_m^I(t)$, and $k_m^M(t)$. The image RMS error of $k_m^v(t)$ (not shown), had an image RMS error of 0.145. The image reconstructed using $\tilde{k}_m(t)$ showed strong ghosting for the entire phantom, that scaled with $\hat{\mathbf{x}}$-distance from the centre of the image. Performing delay correction improved the image significantly, and a similar level of image RMS error was seen for $\tilde{k}_m^E(t)$ and $k_m^M(t)$. The image RMS error of $\tilde{k}_m^E(t)$ was dominated by contributions from a Nyquist ghost of the edges of the imaged phantom, indicating trajectory errors primarily in outer k-space. Ghosting in the image RMS error of $k_m^M(t)$ was less localised and instead distributed over the phase-encoding direction. The image RMS errors of $k_m^I(t)$ were similar to those of $\tilde{k}_m^E(t)$ dominated by high-frequency errors, albeit with higher amplitude. These findings are in concordance with the observations from Figure 2 and Figure 3.

The individual components of the spiral k-space trajectory are depicted in Figure 5. The average k-space trajectory error of $\tilde{k}_s(t)$ was significantly higher than that of $k_s^M(t)$ (2.232% and 0.182%, respectively). The error of $\tilde{k}_s(t)$ was largely caused by a delay of the actual waveform, and $\tilde{k}_s^E(t)$ showed a k-space trajectory error of 0.364%. Reconstructed images from the spiral trajectories are shown in Figure 6. A rotation of the imaged phantom and inconsistent location of its edges was observed in the image reconstructed using $\tilde{k}_s(t)$. Similar was not observed for images reconstructed using $k_s^D(t)$ or $k_s^M(t)$. While the rotation of the phantom was also not observed in the image reconstructed using $\tilde{k}_s^E(t)$ (not shown), the artefacts at the border of the phantom persisted, arguing for delay correction not being sufficient for correction of $\tilde{k}_m(t)$. The spatial dis-

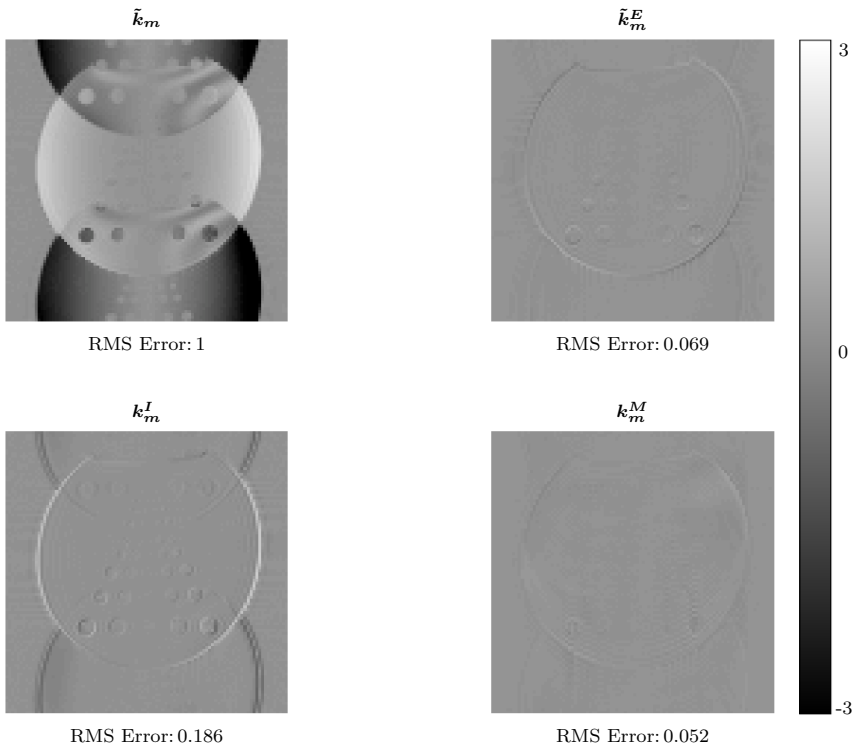

Figure 4 Deviation in reconstructed images compared to the image obtained from reconstruction using $k^D_m(t)$ (image RMS error). The nominal phase-encoding gradient was adopted for all reconstructions. The images were normalised to give $\tilde{k}_m(t)$ an image RMS error of 1. The phase-encoding direction, and thereby the direction of ghosting, is up-down.

tributions of the image RMS error are depicted in Figure 7. While the image RMS errors of all three reconstructions were dominated by contributions close to edges of the phantom, the image RMS error of $k^M_s(t)$ was 80% and 76% lower than of $\tilde{k}_s(t)$ and $\tilde{k}^E_s(t)$ respectively.

6 Discussion

Using custom circuitry, which facilitates sampling of non-MR signals by MR scanners, k-space trajectories were encoded into the raw data of imaging sequences. Determining k-space trajectories, $k(t)$, solely from digitally integrating an inductively generated signal ($v(t)$) showed limited reproducibility. This was addressed by simple regularization using estimates of the gradient from its driving current ($I(t)$). The resulting precision and reproducibility of the regularized inductive k-space trajectory measure ($k^M(t)$) was compared to that obtained from an exclusively inductive measure ($k^v(t)$), exclusively from the driving current ($k^I(t)$), the scanner's assumed k-space trajectory with and without delay correction ($\tilde{k}^E(t)$ and $\tilde{k}(t)$, respectively), and trajectories determined using Duyn's method ($k^D(t)$).

The standard deviation across 50 repetitions was used to evaluate the reproducibility of each of the measures of $k(t)$. Determining $k(t)$ from a digitized inductively generated signal required effectively a double integration, which caused noise to accumulate rapidly. This noise was a primary limitation to the obtainable precision, evident from the standard deviation between repeated acquisitions of $k^v(t)$. In comparison, $k^M(t)$ had significantly lower standard deviation than $k^v(t)$, though higher than $k^I(t)$. A considerable standard deviation was also observed for acquisitions of a single-frequency signal generated by the circuitry. This argues for a significant contribution to the observed stand-

Table 2 Summary of experimental results compared to $k^D(t)$. The first four columns relate to measures of EPI trajectories, $k_m(t)$, and the latter two to spiral trajectories, $k_s(t)$, for which $k^I(t)$ and $k^v(t)$ were not determined. The standard deviation is given for the centre position of k-space.

	EPI				Spiral	
Trajectory	Standard dev.	Traj. error	Traj. error (centre)	Image RMS error	Traj. error	Image RMS error
$\tilde{k}(t)$	-	0.378%	0.435%	1	2.23%	1
$\tilde{k}^E(t)$	-	0.226%	0.030%	0.068	0.364%	0.856
$k^M(t)$	$1.2 \cdot 10^{-3}$	0.173%	0.032%	0.049	0.182%	0.201
$k^I(t)$	$8.5 \cdot 10^{-4}$	0.394%	0.058%	0.186	-	-
$k^v(t)$	$1.4 \cdot 10^{-2}$	0.159%	0.079%	0.145	-	-

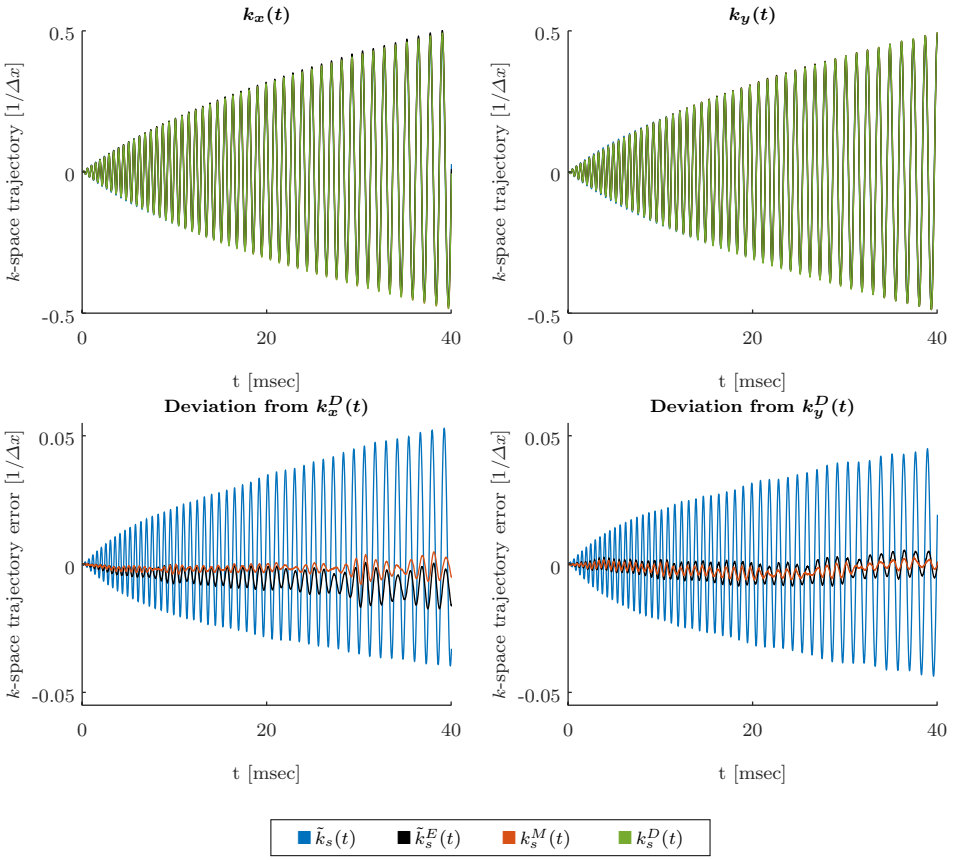

Figure 5 The individual measures of $k_x(t)$ and $k_y(t)$, that together yield $k_s(t)$ (top), and the difference to $k_s^D(t)$ (bottom). The trajectories in the 2 top graphs are not easily distinguishable but up to 5% difference from $k_s^D(t)$ is visible in the bottom graphs.

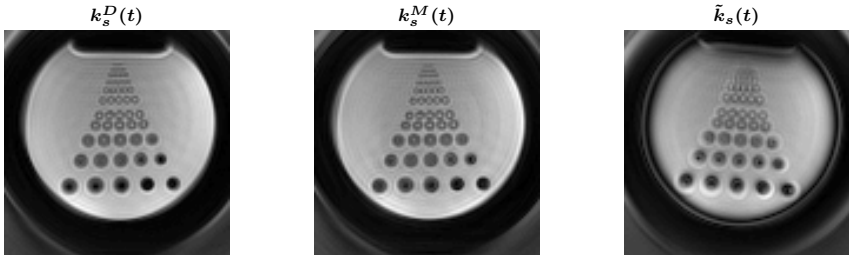

Figure 6 Reconstructed images using different k-space trajectory measures in reconstruction of MR data acquired during a spiral sequence.

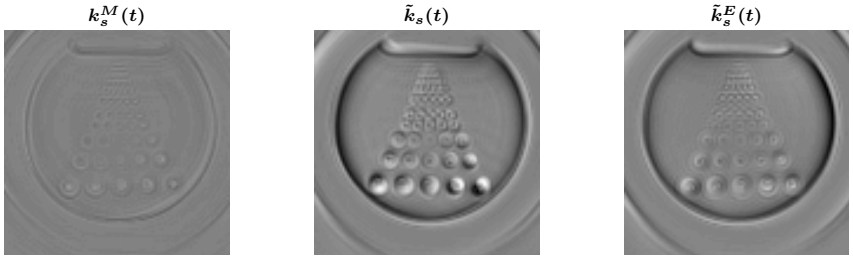

Figure 7 Spatial distribution of the image RMS error for different measures of the k-space trajectory of a spiral sequence.

ard deviation resulting from generation of the circuitry-transmitted signal.

The accuracy of each k-space trajectory measure was evaluated by the averaged trajectory's difference from $k^D(t)$ (k-space trajectory error) and the RMS difference in reconstructed images (image RMS error). As $k^I(t)$ is insensitive to, e.g., eddy currents and dependencies of the generated field to the gradient coils temperature, it is ill-suited to directly predict $k(t)$ on a short time scale, also evident from the observed k-space trajectory error and image RMS error of $k^I(t)$. A large contributor to the image RMS error of $\tilde{k}(t)$ was an effective delay of the gradient waveforms, which is typically accounted for in post-processing of EPI sequences. However, even compared to the corrected trajectory $\tilde{k}^E(t)$, $k^M(t)$ showed a smaller k-space trajectory error and image RMS error. This was particularly observable for spiral k-space trajectories, as $k_s^M(t)$ showed markedly smaller artefacts than $\tilde{k}_s^E(t)$.

In generation of $k^D(t)$, multiple repeated signal acquisitions with varying slice positions were necessary, which caused $k^D(t)$ to benefit from averaging effects reducing its observed standard deviation. This did however not account for the vastly better reproducibility found for $k^D(t)$ compared to the other measured k-space trajectories, and Duyn's method is therefore expected to yield higher sensitivity for sequences where time variance of the gradient system is limited. However, the underlying time-invariance assumption of $k^D(t)$ makes it unsuitable for robust investigation of the accuracy and reproducibility of $k^M(t)$ acquired concurrently with MR data from gradient intensive sequences. For such investigation, a putative solution is using field probes, as they also facilitate concurrent MR and k-space trajectory acquisition, and the obtainable sensitivity is similar or superior to Duyn's method [12].

All acquired trajectories have been obtained under assumption of spatially linear gradients, and any non-linearities potentially influence the individual k-space trajectory measures differently. An estimate of the linearity can be obtained by comparing differences in the phase evolution from different slice positions when obtaining $k^D(t)$. Here, the largest RMS difference (2.1% for 100 mm difference in slice position) was comparable to what has previously been reported and found to have minimal effect on reconstructed images [7]. The non-linearities are, however, temperature-dependent [17], arguing for the necessity of accounting for these for gradient intensive sequences. Assuming the non-linearities are spatially slowly varying, spherical harmonic functions can be fitted to spatially distributed point-measurements of the field [27], which is feasible with measurements from multiple pick-up coils. Alternatively, the assumption of global linearity can be relaxed to an as-

sumption of local linearity by using gradiometers [23]. It is possible that using a common basis for regularization of the individual measures, such as $I(t)$ or the nominal gradient trajectory, limits the obtainable sensitivity, but this remains to be investigated further. Similarly, more accurate regularization schemes may be envisioned by, e.g., introducing a temporal dependency to λ, to avoid the initial increase in k-space trajectory error introduced in $k_m^M(t)$, or including measurements from other sensors with other noise profiles, such as Hall sensors, magneto-diode magnetometers, or pick-up coils with different sensitivities.

In acquisition of all the acquired k-space trajectory measures, the individual spatial components were determined separately, as untangling of multiple contributions was infeasible for single-probe recordings. Putative contributions from concomitant fields generated by gradients played out in other directions are therefore not accounted for, and concurrent 2D image acquisition and $k^M(t)$ acquisition is currently not possible. If $v(t)$ is acquired from multiple pick-up coils, and potentially $I(t)$ from multiple gradient amplifiers, the individual gradient field components may be disentangled using, e.g., calibration scans. The disentangling can in principle be performed in real time using the FPGA featured by the applied circuitry, at the cost of a prolonged delay of the signal through the circuitry. The additional delay would likely be minimal, as the current delay is dominated by digitization, and updating of the frequency output of the circuitry. In addition, the circuitry is limited in the number of signals recorded and generated (three and one, respectively), and such experiments would potentially require an extension, or alternatively the use of multiple circuitries for retrospective untangling.

The method of Duyn et al [15] relies on encoding a k-space trajectory measure into the phase of an MR signal. This makes the obtainable sensitivity directly dependent on the SNR of the MR signal, and thereby challenged by sequences with long readouts or low gamma MRI such as ^{13}C and ^{23}Na. The signal may in addition experience dephasing across the excited slice, further limiting the obtainable SNR. The method also relies on correct unwrapping of the phase of the MR signal, effectively limiting the maximum k-space position change between sample points. While $k^M(t)$ likewise is challenged by long readouts due to the accumulation of noise, the obtainable sensitivity is independent of the imaged nucleus, as this simply leads to a change in the frequency of the carrier signal. Also the circuitry allows for free choice of scaling of the ratio between k-space trajectory measures and phase of the transmitted signals, making arbitrarily long dwell-times and strong gradients manageable.

Only excitatory RF pulses were applied in the performed experiments, and the long TR compared to T_1 of the imaged phantom ensured that signal contributions from non-primary echoes could be disregarded. The effect of refocusing RF pulses on k-space trajectories was therefore not addressed. Determining the tip angle of an RF pulse is not directly feasible from circuitry measurements, as only the envelope of RF pulses is acquired. One possible approach for handling non-excitatory RF pulses is to assume nominal tip angles, and utilize prior knowledge of distinguishable features, e.g., maximum amplitude, duration and timing compared to gradients to discriminate between pulses of different tip angles. Such prior knowledge can either be hard-coded into memory of the circuitry, or transmitted by the scanner to a receive channel of the circuitry.

There is considerable potential for further improvement by development of the prototype circuitry implementation here used to demonstrate proof-of-concept. Of the current 15.1 µs delay through the circuitry, 8 µs are due to digitization and communication from the ADCs to the FPGA, and 4.5 µs are due to communication from the FPGA to the DDS. The delay can be decreased at the cost of, e.g., reduced ADC linearity, fewer communicated bits, increased expense of the circuitry, or by using parallel communication, which can reduce the delay through the circuitry without affecting the number of bits transmitted. For example, transmission using 4 connections compared to the current single connection would roughly half the total delay through the circuitry. An increased dynamic range of the ADC would reduce the quantization error of digitizing $v(t)$ and thereby increase the reproducibility of $k^v(t)$. For example, LTC2387-18 (Analog Devices, Inc) facilitates a dynamic range of 120 dB at 25 kHz sampling rate (with oversampling), 25 dB more than currently implemented. The price of this ADC would however double the total material cost of the circuitry from it's current price of 125USD, and increase the power consumption of the ADCs 100-fold, making battery-driven usage less attractive. The limited reproducibility of single-frequency signals by the circuitry, indicates that a putative increased performance is achievable with a more precise signal-generation than currently available. The performance of the implemented DDS is limited by the frequency of the clock of the circuitry, and up to 30 dB decrease in DDS-induced noise is achievable by the use of a higher frequency oscillator[2]. This would in turn also decrease the delay through the circuitry, though notably also increase the cost of the circuitry. Implementation of these alternatives and further develop-

ment of the circuitry can potentially make the circuitry-induced delay insignificant compared to the dwell-time of typical MRI acquisitions.

In conclusion, regularized inductive k-space trajectory measures were encoded and extracted from signals acquired by an MR scanner. For reconstruction of EPI, the determined k-space trajectory performed slightly better than a delay-compensated k-space trajectory assumed by the scanner. For spiral trajectories, the regularized inductive measure outperformed the scanner's k-space trajectory, and produced images without severe artefacts. The method allows for concurrent acquisition with MR signals, and is an inexpensive and relatively simple approach for real-time determination of k-space trajectories for debugging and for correct reconstruction of gradient-demanding sequences.

References

1. (????) Encoding of non-MR signals in scanner recordings. `http://drcmr.dk/MagstripeEncoding`, [Online; accessed 14-August-2018]
2. (2016) Direct Digital Synthesize. "Analog Devices", rev. B
3. Addy NO, Wu HH, Nishimura DG (2012), Simple method for MR gradient system characterization and k-space trajectory estimation. Magnetic Resonance in Medicine 68(1):120–129
4. Barmet C, Zanche ND, Pruessmann KP (2008), Spatiotemporal magnetic field monitoring for MR. Magnetic Resonance in Medicine 60(1):187–197
5. Barmet C, De Zanche N, Wilm BJ, Pruessmann KP (2009), A transmit/receive system for magnetic field monitoring of in vivo MRI. Magnetic Resonance in Medicine 62(1):269–276
6. Bernstein MA, King KF, Zhou XJ (2004) Handbook of MRI Pulse Sequences. DOI 10.1016/B978-0-12-092861-3.X5000-6, `arXiv:1011.1669v3`
7. Brodsky EK, Samsonov AA, Block WF (2009), Characterizing and correcting gradient errors in non-Cartesian imaging: Are gradient errors Linear Time-Invariant (LTI)? Magnetic Resonance in Medicine 62(6):1466–1476
8. Bruder H, Fischer H, Reinfelder HE, Schmitt F (1992), Image reconstruction for echo planar imaging with nonequidistantk-space sampling. Magnetic Resonance in Medicine 23(2):311–323
9. Brunner DO, Dietrich BE, Cavusoglu M, Wilm BJ, Schmid T, Gross S, Barmet C, Pruessmann KP (2016), Concurrent recording of RF pulses and gradient fields - comprehensive field monitoring for MRI. NMR in Biomedicine 29(9):1162–1172
10. Campbell-Washburn AE, Xue H, Lederman RJ, Faranesh AZ, Hansen MS (2016), Real-time distortion correction of spiral and echo planar images using the gradient system impulse response function. Magnetic Resonance in Medicine 75(6):2278–2285
11. D'Antona G, Lazzaroni M, Ottoboni R, Svelto C (2003), AC current-to-voltage transducer for industrial application. Instrumentation and Measurement Technology Conference, 2003 IMTC '03 Proceedings of the 20th IEEE 2(May):1185–1190 vol.2
12. De Zanche N, Barmet C, Nordmeyer-Massner Ja, Pruessmann KP (2008), NMR Probes for measuring magnetic fields and field dynamics in MR systems. Magnetic Resonance in Medicine 60(1):176–186
13. Delattre BMA, Heidemann RM, Crowe LA, Vallée JP, Hyacinthe JN (2010), Spiral demystified. Magnetic Resonance Imaging 28(6):862–881
14. Dietrich BE, Brunner DO, Wilm BJ, Barmet C, Gross S, Kasper L, Haeberlin M, Schmid T, Vannesjo SJ, Pruessmann KP (2016), A field camera for MR sequence monitoring and system analysis. Magnetic Resonance in Medicine 75(4):1831–1840
15. Duyn JH, Yang Y, Frank JA, van der Veen JW (1998), Simple Correction Method for k-Space Trajectory Deviations in MRI. Journal of Magnetic Resonance 132(1):150–153
16. Greengard L, Lee JY (2004), Accelerating the Nonuniform Fast Fourier Transform. SIAM Review 46(3):443–454
17. Kasper L, Bollmann S, Vannesjo SJ, Gross S, Haeberlin M, Dietrich BE, Pruessmann KP (2015), Monitoring, analysis, and correction of magnetic field fluctuations in echo planar imaging time series. Magnetic Resonance in Medicine 74(2):396–409
18. Mason GF, Harshbarger T, Hetherington HP, Zhang Y, Pohost GM, Twieg DB (1997), A method to measure arbitrary k-space trajectories for rapid MR imaging. Magnetic Resonance in Medicine 38(3):492–496
19. Milano P, Elettrotecnica D (2002), AC current Measurements via digital processing of rogowski coils signal.pdf (May):21–23
20. Onodera T, Matsui S, Sekihara K, Kohno H (1987), A method of measuring field-gradient modulation shapes. Application to high-speed NMR spectroscopic imaging. Journal of Physics E: Scientific Instruments 20(4):416–419
21. Pedersen JO, Hanson CG, Xue R, Hanson LG (in press), General Purpose Electronics for Real-Time Processing and Encoding of non-MR Data in MR Acquisitions. Concepts of Magnetic Resonance B, doi:101002/CMRB21385
22. Pipe JG, Menon P (1999), Sampling density compensation in MRI: Rationale and an iterative numerical solution. Magnetic Resonance in Medicine 41(1):179–186
23. Senaj V, Guillot G, Darrasse L (1998), Inductive measurement of magnetic field gradients for magnetic resonance imaging. Review of Scientific Instruments 69(6):2400–2405
24. Spielman DM, Pauly JM (1995), Spiral imaging on a small-bore system at 4.7t. Magnetic Resonance in Medicine 34(4):580–585
25. Vannesjo SJ, Haeberlin M, Kasper L, Pavan M, Wilm BJ, Barmet C, Pruessmann KP (2013), Gradient system characterization by impulse response measurements with a dynamic field camera. Magnetic Resonance in Medicine 69(2):583–593
26. Vannesjo SJ, Dietrich BE, Pavan M, Brunner DO, Wilm BJ, Barmet C, Pruessmann KP (2014), Field camera measurements of gradient and shim impulse responses using frequency sweeps. Magnetic Resonance in Medicine 72(2):570–583
27. Wilm BJ, Barmet C, Pavan M, Pruessmann KP (2011), Higher order reconstruction for MRI in the presence of spatiotemporal field perturbations. Magnetic Resonance in Medicine 65(6):1690–1701

C | Mary had a little Lamb: Scanner-recorded speech during MRI without gradient-induced sound

The following abstract was submitted and presented at *The ISMRM 25th Annual Meeting & Exhibition, 2017.*

Mary had a little Lamb: Scanner-recorded speech during MRI without gradient-induced sound

Jan Ole Pedersen[1,2], Christian Hanson , Rong Xue[3], and Lars G. Hanson[1,2]

[1] *Danish Research Centre for Magnetic Resonance, Centre for Functional and Diagnostic Imaging and Research, Copenhagen University Hospital, Hvidovre, Denmark*
[2] *Center for Magnetic Resonance, Electrical Engineering, Technical University of Denmark, Kgs. Lyngby, Denmark*
[3] *State Key Laboratory of Brain and Cognitive Sciences, Institute of Biophysics, Chinese Academy of Sciences, Beijing, China*

C.1 Synopsis

During MRI, fast switching of imaging gradients generate loud noise of high intensity due to vibration of the gradient coils. The in-bore intercom used for patient communication is therefore typically turned off during scanning. This has implications for safety and image quality since patient speech and yells are not heard by the scanner operator. Using standard sequences, we demonstrate that sound can be recorded by MRI scanners and extracted from the scanners raw data, thereby enabling communication with patients for safety or experimental reasons.

C.2 Introduction

For most MRI sequences, acquisition is performed without ramp-sampling and therefore in silent periods. Using the scanner itself for acquisition of a sound signal alleviates timing challenges arising when using external equipment. This is however not directly feasible, as the filters of the scanner attenuates signal outside a narrow range around the Larmor frequency. However, by performing an amplitude modulation of the sound signal to a frequency close to the Larmor frequency allows the signal to pass the filters of the scanner, and the demodulation performed by the scanner restores the original sound signal except for a small frequency offset. The sound can then be extracted from the raw data of the scan. The constant timing between sampling and gradient waveforms allow for easy filtration of residual gradient induced noise in the sound signal. Using a dedicated receive channel of the scanner allow for sampling of the sound signal with high SNR and without interference from MR signals.

C.3 Method

Two 2" loudspeakers were sacrificed to make a simple MR-compatible microphone: A loudspeaker coil mounted on a membrane was placed in a tube inside the static field (B_0) of the scanner.

Membrane vibration thus generated a coil voltage, i.e. a sound signal. An identical coil with no membrane was mounted in series with similar orientation and close to the microphone coil to cancel out gradient-induced voltages. The coils were connected to a modulator circuitry developed previously[1] for amplitude modulation of non-MR signals for wireless recording by scanners. Due to a maximum carrier frequency of 130MHz producible by the modulator, the signal was send through a 200 MHz mixer to reach the frequency range of the scanner (hydrogen at 7 T, Siemens Magnetom). To remove any DC component, the modulated signal was sent via two inductively coupled coils, before reaching a receive channel of the scanner. A 50 Ω resistor in parallel with the transmission line of the modulator made the setup recognizable by the scanner as a coil element. The sound signal was send by the modulator continuously, but only sampled by the scanner during acquisition periods. During a GRE sequence (256×128 receive matrix, 5 volumes) a subject was asked to repeatedly say out loud "Mary Had a Little Lamb" (chosen for melodramatic effect, as the verse was famously used by Edison for the first sound recording ever). Non-linearities from the modulator were compensated before the DC component was removed. The phase-locked noise from the readout gradient and noise from the phase-encoding gradient were relatively easily estimated and subtracted. The non-equidistant sampling in time of the GRE sequence left periods without sound data. Autoregressive modelling across short subsets of the data, where the noise was assumed to be unchanged, was used to fill these gaps.

C.4 Results

A sound recording with easily recognizable repetition of "Mary Had a Little Lamb", acquired by an MRI scanner was obtained after removal of residual scanner noise. In contrast to direct audio recording, gradient noise is barely audible.

C.5 Discussion & Conclusion

Through the use of a homebuilt MR compatible microphone and amplitude modulation, we have shown it possible to record sound signals using a receive channel of an MRI scanner. The limited signal processing needed to obtain recognizable vocalization allow for fast signal processing, and thereby real-time oral communication with a patient during scanning. Here a separate channel of the scanner was used for receiving the sound signal. As previously shown[1], it is possible to transmit a signal wirelessly at a frequency in the oversampled range of the scan (sampled by the scanner, but not in FOV), and thereby receive the sound MRI signal on common receive channels.

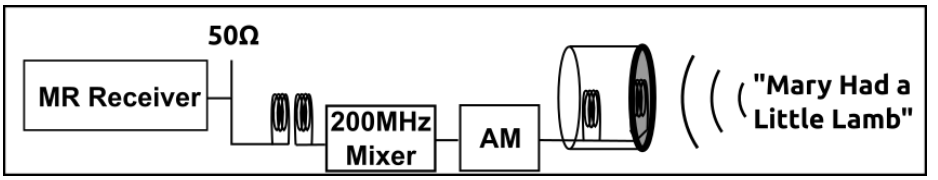

1. Hanson, L. G., Lund, T. E. & Hanson, C. G. Encoding of electrophysiology and other signals in MR images. *Journal of Magnetic Resonance Imaging* **25,** 1059–1066 (2007).